博士論文

Laboratory and analytical study of surge-induced impact pressure on a vertical wall

(Surge により直立壁に作用する衝撃圧に関する

水理実験及び解析的研究**)**

Wenang XIE

謝　文昂

Department of Civil Engineering

School of Engineering

The University of Tokyo

2022

博士論文

Laboratory and analytical study of surge-induced impact pressure on a vertical wall

(Surge により直立壁に作用する衝撃圧に関する

水理実験及び解析的研究**)**

Wenang XIE

謝　文昂

Thesis submitted

for the degree of

Doctor of Philosophy

Department of Civil Engineering

School of Engineering

The University of Tokyo

Tokyo, Japan

2022

Author's Declaration

I hereby declare that I am the sole author of this thesis.

I authorize the University of Tokyo to lend this thesis to other institutions or individuals for the purpose of scholarly research.

Signature

I further authorize the University of Tokyo to reproduce this thesis by photocopying or by other means, in total or in part, at the request of other institutions or individuals for the purpose of scholarly research.

Signature

Abstract

Devastating impact pressure could be generated when water surge impinges onto a solid surface (a typical example is a vertical wall). As of now, engineers are using empirical formulas obtained from laboratory experiments to evaluate the surge-induced impact pressure. In laboratory studies, although it is a very difficult task to measure the velocity field near the wall, the impact pressure has been recorded by highly sensitive pressure sensors on the wall. However, in many of those studies, it has been repeatedly reported that the surge-induced impact pressure is a highly stochastic variable. Therefore, the existing deterministic empirical engineering formulas for the impact pressure obtained by different authors fail to agree with each other, and there is no stochastic model has been proposed as of now. Also, due to the lack of a sound theoretical physical foundation, these formulas involve different physical parameters from each other.

Numerical calculations on this issue have recently become popular with various sophisticated computational tools. Although some numerical models successfully provided detailed information of the velocity and pressure fields during surge impact events for small-scale cases, it is simply too time-consuming and expensive to conduct accurate calculations for large-scale problems. Also, the abrupt changes in the velocity field and free water surface during the impingement are not handled well by most computational models as of now, which is calling for a physical insight of the fluid motions at the first contact between surge and structure.

The number of analytic theories describing the surge impingement onto a vertical wall is surprisingly limited. The main reason is the difficulty in handling the sudden changes in the velocity field of water motions during the impingement process. This transient process usually involves singularities in its mathematical description, and thus different physical assumptions have been introduced to simplify the problem. However, some major assumptions in the past analytic studies yielded peculiar results at times, and few verification has been made for them. This situation prevented people from having a further insightful view of physics and may result in misunderstanding of the governing physical parameters of the impact pressure.

The main objective of the present study is to advance and renew people's knowledge on the physics of surge-induced impact pressure, including the governing equation, boundary conditions, initial conditions and its stochastic nature. This study improves the shortcomings, as introduced, in the existing literature. The following two issues are supportive of this main objective.

① This study clearly reveals the governing and trivial physical parameters of surge-induced impact pressure, providing a sound theoretical basis for laboratory and numerical studies.

② This study presents a pioneer work on quantifying the stochastic nature of the surge-induced impact pressure, proposing a specific extreme value distribution for it.

In the theoretical derivations of the analytic solution, the velocity field near the bed is directly obtained from the simplified vorticity transport equation. A self-similarity system without any representative length is proposed for the horizontal velocity component with

clearly defined boundary conditions and initial conditions. Following the solution of the velocity field, the pressure field during the impingement is derived in an explicit form. Consequently, the impact pressure applied on the vertical wall could also be clearly calculated, and it converges to a specific finite value. Through this analytic investigation, the impactive process right after the first contact between surge and wall is reasonably interpreted, and the governing and trivial factors of the impact pressure are also revealed theoretically.

Carefully controlled laboratory experiments are conducted to reveal the stochastic nature of the impact pressure. The experiments are carried out in a small-scaled acrylic flume with a dam-break device and a vertical wall. The surges and the impact pressure generated in four different experimental cases are repeatedly recorded by a high-speed camera and pressure sensors near the corner where the vertical wall and the flume bottom meet. An extreme value distribution model, Fréchet distribution, is used to quantify the stochastic relationship between surge front velocity and impact pressure explicitly. On the other hand, the laboratory data agree with the conclusion on the governing factors made in the analytic solution. Moreover, the resulting predictive stochastic formula demonstrates a wide applicable range for actual engineering works.

Numerical verifications on the velocity and pressure fields during a surge impingement event are carried out with a CFD software, Flow-3D. The experimental cases in the laboratory works are reconducted numerically with different computational conditions. With the numerical results, the soundness of the analytic solution is verified. Also, the numerical results are shown to be consistent with the laboratory data.

With the analytic, laboratory experimental studies, and numerical verifications introduced above, the essential characteristics of the surge-induced impact pressure are studied comprehensively, renewing the achievements in the existing literature. The analytic solution proposed in the present study provides people an insightful view on the physics of surge impingement, describing the velocity and pressure field during the impingement and clearly indicating the governing factor of the impact pressure. On the other hand, the laboratory study suggests a way of predicting the impact pressure in actual engineering works, using a specific stochastic distribution.

INDEX

Chapter 1 1
1.1 Motivation and background 1
1.2 Scope of the thesis 5
1.3 Organization of the thesis 6
Chapter 2 7
2.1 Impact pressure generated by liquid-solid interaction 7
2.2 Surge-induced impact pressure 13
2.2.1 Laboratory studies 13
2.2.2 Analytical works 15
2.2.3 Numerical calculations 20
Chapter 3 23
3.1 Introduction 23
3.2 Experimental setup and devices 25
3.2.1 Flume setup 25
3.2.2 Instruments setup 27
3.2.3 Experimental cases 29
3.3 Experimental results 33
3.3.1 Time history of pressure on the vertical panel 33
3.3.2 Distribution of the impact pressure 35
3.3.3 Distribution of surge front velocity 38
3.3.4 Surge front shape and surge front slope 39
3.4 Stochastic model for the impact pressure and discussions on the effect of surge front slope 44
3.4.1 Stochastic model for impact pressure 44
3.4.2 Relationship between C_p and surge front slope 51
3.5 Findings and motivations of further investigations 54
Chapter 4 56
4.1 Introduction 56
4.2 Initial-boundary value problem 58

4.3 Self-similarity solution of velocity field 65
4.4 Self-similarity solution of pressure field 73
4.5 Comparison between the analytical solution of C_{pw0} and existing studies 77
4.6 A brief discussion on viscosity 81
Chapter 5 84
5.1 Introduction 84
5.2 General descriptions of the numerical tool 86
5.3 Verifications of the analytic solution 88
5.3.1 Velocity field 91
5.3.2 Pressure field 98
5.4 Effects of viscosity and turbulence 100
5.4.1 Velocity field 104
5.4.2 Pressure field 107
Chapter 6 110
Appendix A 112
Appendix B 114
Appendix C 118
Bibliography 119
Acknowledgements 126

List of figures

Figure 1.1 Photograph taken at Ohgawa Elementary School after the 3.11 Tohoku tsunami, Miyagi prefecture, Japan 2

Figure 2.1 Physical model used in Cooker and Peregrine (1995) 17

Figure 2.2 Physical model used in Cumberbatch (1960).....18

Figure 2.3 Fig. 2.3 Relationship between Cp, λw and θ 19

Figure 3.1 Photograph of the experimental flume. 25

Figure 3.2 Sketch of the experimental setup (vertically exaggerated, length in mm). 26

Figure 3.3 Typical fluid motion during the dam-break experiment (H = 12 cm) 0.033 s (top left), 0.133 s (top right), 0.233 s (middle left), 0.333 s (middle right), 0.433 s (bottom left) and 0.467 s (bottom right) after the sluice gate opening. 30

Figure 3.4 Typical surge front during an impingement event (H = 12 cm, overhead view) 0.333 s (top left), 0.367 s (top right), 0.400 s (middle left), 0.433 s (middle right), 0.467 s (bottom left) and 0.500 s (bottom right) after the sluice gate opening. 31

Figure 3.5 Typical surge front shape right before the impact with H = 8 cm (top left), H = 10 cm (top right), H = 12 cm (bottom left) and H = 14 cm (bottom right). 32

Figure 3.6 Time history of pressure applied on P0 with H = 8 cm (top left), H = 10 cm (top right), H = 12 cm (bottom left) and H = 14 cm (bottom right). 33

Figure 3.7 Time history of pressure applied on P1 with H = 8 cm (top left), H = 10 cm (top right), H = 12 cm (bottom left) and H = 14 cm (bottom right). 34

Figure 3.8 Cumulative percentile ranking graphs of the impact pressure in different cases at P0 (top) and P1 (bottom). 36

Figure 3.9 Relationship between the impact pressures at P0 and P1. 38

Figure 3.10 Cumulative percentile ranking graph of the squared dimensionless surge front velocity in different cases 39

Figure 3.11 Time history of water surface elevation 10 cm away from the panel after the arrival of the surge front with H = 8 cm (top left), H = 10 cm (top right), H = 12 cm (bottom left) and H = 14 cm (bottom right).....41

Figure 3.12 Time history of water surface elevation 10 cm away from the panel after the arrival of the surge front with H = 8, 10, 12 and 14 cm (median curves). ..42

Figure 3.13 Cumulative percentile ranking graph of the average surge front slope within 0.02 s after the arrival of the surge front in different cases. 43

Figure 3.14 Cumulative percentile ranking graphs for impact coefficient Cp in different cases at P0 (top) and P1 (bottom). 45

Figure 3.15 Fitting curves based on the Fréchet distribution for P0 with (σ, s) = (3.52, 0.737) (top left, top right) and P1 with (σ, s) = (3.31, 0.674) (bottom left, bottom right).....48

Figure 3.16 Comparison between Equation (3.4.1) with (s, σ) = (3.52, 0.737) and (3.31, 0.674) and published data. 50

Figure 3.17 Relationship between the surge front slope and impact coefficient in different cases at P0 (top) and P1 (bottom), combined with the theory proposed by Cumberbatch (1960). 52

Figure 3.18 Relationship between the squared surge front velocity and surge front slope in different cases.....54

Figure 4.1 Conceptional sketch of water surge impingement onto a vertical wall. 58

Figure 4.2 Conceptional sketch interpreting the moving boundary conditions. 63

Figure 4.3 Solutions of $F(X)$ at different accuracy 69

Figure 4.4 Relative differences between Fq (X) and Fq-1 (X) (q=5,6,7,8). 70

Figure 4.5 Solutions of G (X, Y) 71

Figure 4.6 Solutions of V (X, Y).....71

Figure 4.7 Sketch of the definition of S.....75

Figure 4.8 Comparison among the laboratory data of C_{pw0} at P0, with Equation (4.47), (4.48) and (4.50).....80

Figure 4.9 Comparison among the laboratory data of C_{pw0} at P1, with Equation (4.47), (4.48) and (4.50).....80

Figure 5.1 Fluid motion of inviscid dam-break flow (H = 12 cm) 0.033 s, 0.133 s, 0.233 s, 0.333 s, 0.367 s, 0.433 s and 0.467 s after the water column starts collapsing (from top to bottom). Lengths are in m and velocity in m/s.....89

Figure 5.2 Comparison between numerical data of $F(X)$ and the theoretical results (from top to bottom, H=8 cm, 10 cm, 12 cm and 14 cm).....92

Figure 5.3 Comparison between numerical data of $F'(X)$ and the theoretical results (H=8 cm, 10 cm, 12 cm and 14 cm, t=0.003 s).....95

Figure 5.4 Comparison between the numerical data of G (X, Y) and the theoretical curves provided by Equation (4.34), H=8 cm.....96

Figure 5.5 Comparison between the numerical data of V (X, Y) and the theoretical curves provided by Equation (4.35).....96

Figure 5.6 Distribution of dimensionless vorticity with H=8 cm.....97

Figure 5.7 Comparison between the numerical data of C_p (X) and the theoretical curve provided by Equation (4.44).....99

Figure 5.8 (1) Fluid motion of viscous dam-break flow (H = 12 cm) 0.033 s, 0.133 s, 0.233 s, 0.333 s, 0.433 s and 0.467 s after the water column starts collapsing (from top to bottom). Lengths are in m and velocity in m/s. 101

Figure 5.8 (2) Fluid motion of viscous dam-break flow (H = 12 cm) 0.033 s, 0.133 s, 0.233 s, 0.333 s, 0.433 s and 0.467 s after the water column starts collapsing (from top to bottom). Lengths are in m and energy in m^2/ s^2 103

Figure 5.9 Particle velocity near the bed in inviscid and viscous flows right before the impact, combined with the solution of Ritter (1892).....105

Figure 5.10 Comparison between the numerical data of F (X) in viscous and inviscid flows during the impingement.....106

Figure 5.11 Comparison between the numerical data of C_p (X) in inviscid and viscous flows, with the theoretical curve provided by Equation (4.44) 108

Figure 5.12 Comparison between the numerical data of impact pressure in inviscid and viscous flows, with the theoretical curve provided by Equation (4.44). ...108

Figure A.1 Comparison of the cumulative percentile distribution of impact pressure between the original data of Lobovský et al. (2014) and the re-sampled data using a sampling rate of 500 Hz 111

Figure B.1 Relationship between C_p and $R^2_{C_p}$ at P0 (H=8, 10, 12 and 14 cm).....114

Figure B.2 Relationship between C_p and $R^2_{C_p}$ at P1 (H=8, 10, 12 and 14 cm).....114

Figure B.3 Relationship between tanθ and $R^2_{\tan\theta}$ at P0 (H=8, 10, 12 and 14 cm).....115

Figure B.4 Relationship between tanθ and $R^2_{\tan\theta}$ at P1 (H=8, 10, 12 and 14 cm).....116

Figure C.1 Comparison between the velocity fields using mesh sizes of 0.5 ×0.5 mm and 1.0×1.0 mm with H=8 cm.....117

List of tables

Table 2.1 Summary of different categories of the impact pressure generated in liquid impingement 12

Table 3.1 Parameters of the proposed probability distributions (fitting curves) 49

Table 4.1 Solutions of the coefficients in Equation (4.22) and the value L for $F^q(X)$ .. 68

Table 4.2 Calculated impact coefficient at different accuracy 75

Table 4.3 Differences between the present theory and Cumberbatch (1960) 78

Table 4.4 Assumptions used in the derivations 81

Table 5.1 Representative parameters of water used in numerical calculations 86

Table A.1 Comparison of percentiles of impact pressure between the original data of Lobovský et al. (2014) and the re-sampled data using a sampling rate of 500 Hz 112

Chapter 1
General introduction

1.1 Motivation and background

Devastating pressure can be generated by the impingement of liquid onto a solid surface, and the prediction of this pressure is a long-standing issue in various engineering fields. One well-known problem is water surge impingement onto structures. The terminology 'surge' is frequently encountered in hydraulic and coastal engineering, such as dam-break flows and tsunami run-up on a coast. In this context, a surge is a transient, supercritical flow mainly formed by the breaking of long waves or the sudden collapse of a water column under the effect of gravity. Usually, it generates destructive pressure accompanied by a high splash of water onto structures standing on its travel route. Figure 1.1 is the photograph that the author took at Ohgawa Elementary School in Miyagi prefecture, Japan, after the 3.11 Tohoku Tsunami. The figure shows that the lower parts of the columns were severely damaged by the surge impact, resulting in the instability and destruction of the entire structure. The school was standing near the Kitagawa River (less than 150 m away from the riverside), and it was attacked by the ruinous run-up tsunami surge from the river. Many similar cases have been reported by the survey teams after the tsunami event (refer to the 2011 Tohoku Earthquake Tsunami Joint Survey (TTJS) Group, 2012). Thus, it is of critical importance to appropriately account for the pressure generated by water surges in structural designs.

Fig. 1.1 Photograph taken at Ohgawa Elementary School after the 3.11 Tohoku tsunami, Miyagi prefecture, Japan

However, evaluating the impact pressure induced by fluid is by no means an easy task. There are mainly three approaches to study the surge impact problem: laboratory experiment, theoretical analysis, and numerical calculation. Direct on-site survey is not available for this issue as surge impact is a very transient and destructive phenomenon. Therefore, it is simply not possible for people to measure the magnitude of the impact pressure timely. On the other hand, although the above-mentioned three approaches have been taken by a number of authors, various difficulties were encountered in their works.

Many organizations in different countries have proposed guidelines with empirical formulas for engineers to predict the pressure induced by water surges (e.g., ASCE 2017 and FEMA 2019). These formulas are based on the past laboratory experiments conducted by a number of researchers under different experimental conditions. However, these

authors and guidelines have suggested different formulas or even used different physical parameters to describe the surge-induced impact pressure. The main reason is that the laboratory works fail to be consistent with each other. There are mainly two aspects of this issue. Firstly, many empirical formulas involved the parameters for specific experimental set-up, e.g., initial water lever in a dam-break device, wave height in solitary wave breaking. However, as a classic mechanical phenomenon, the impact pressure should be determined only by the physical parameters right before the impact, not by those of surge generation. Therefore, in this sense, the governing factors of the impact pressure should be measured right before the impact. Secondly, the magnitude of surge-induced impact pressure is known to be stochastic. Even in carefully controlled laboratory works, the pressure peaks are distributed in a wide range under the same experimental condition. Therefore, different laboratory works quantified the impact pressure with different values, which has brought significant biases when proposing empirical formulas based on these laboratory data. In other words, only by taking stochasticity into account can people correctly evaluate the magnitude of impact pressure. These two issues have not been addressed soundly as of now. Neither the governing and trivial factors of the surge-induced impact pressure are clearly indicated, nor has any stochastic model been proposed.

Theoretical research on the impact stage is known to be a recalcitrant topic in hydrodynamics. The main difficulties for theoretical analysis are the absence of a characteristic length in the problem and the highly transient (singular, by case) nature of the physical phenomenon. There are basically two ways to deal with this situation: the self-similarity method and the pressure impulse method. The self-similarity method is a

potent tool for handling the physical phenomena where no explicit characteristic length could be defined. At the same time, it provides a possibility to avoid having singularities during the mathematical derivations. However, this method needs very careful definitions of the physical conditions, e.g., the governing equation, the initial condition, and the boundary conditions, since it closely looks into the details of the velocity and pressure fields. Unfortunately, many theoretical works did not provide verifications on their physical assumptions, partially because of the difficulties in collecting laboratory data (previously introduced), and another reason is the misunderstandings on the impact physics. In recent years, with the development of computational technology, chances are coming for people to verify the theoretical assumptions and results in detail with highly advanced numerical models. The pressure impulse method focuses on the integral of pressure over time. The advantage of this method is that the physics models considered are quite simple, and usually, it provides people with a classic boundary value problem of an elliptic differential equation. However, this method could not be used to calculate the detailed pressure distribution inside the integrating span. Therefore, there is a significant difficulty when predicting the exact impact pressure peak solely from the pressure impulse, although some laboratory studies have revisited the results of the pressure impulse itself. Generally, theoretical analysis is not an effective approach to describe the stochasticity of the impact pressure as the physical models are solved in deterministic manners. However, it elucidates the underlying physics of surge impact, advancing people's knowledge on how the impact pressure peak is generated.

As previously mentioned, the numerical method could be used to verify the soundness of theoretical and laboratory results. Until recent years, the computation of highly

transient flows, such as surge impact, was considered a tough problem in CFD (Computational Fluid Dynamics), especially with the existence of a free surface. The main reason was that the physical parameters abruptly change during a transient process, and there is a difficulty in capturing this change numerically. When an unsuitable algorithm or mesh construction is applied, significant losses in momentum and energy are inevitable, which is unacceptable for pressure peak evaluation. Recently, a number of advanced CFD tools have been developed, and they are designed capable of correctly computing the transient flows, though most of them are still time-consuming and only applicable for small-scale problems. By taking advantage of these numerical tools, people have become able to justify their physical assumptions in the analytic works and reproduce the laboratory data.

1.2 Scope of the thesis

The main purpose of the present thesis is to advance people's knowledge of the physics of how the impact pressure is generated by surges and how its magnitude is distributed stochastically. To achieve this purpose, the author has to

1. present a pioneer work on quantifying the stochastic nature of the surge-induced impact pressure and propose a specific extreme value distribution for it based on an observed governing factor of the surge impact.
2. analytically and explicitly reveal the governing and trivial physical parameters of surge-induced impact pressure; propose an analytic solution for the impact pressure; and provide a sound theoretical basis for laboratory and numerical studies.

1.3 Organization of the thesis

This thesis is divided into six chapters. Chapter 2 presents a literature review on the historical studies related to the surge impact problem. In this chapter, we will see that researchers have elaborated and succeeded in overcoming many difficulties in this topic, remaining the unsolved issues mentioned in Section 1.1. Chapter 3 demonstrates a carefully controlled laboratory work measuring the surge-induced impact pressure on a vertical wall with measurements of the physical parameters right before the impact. This chapter also proposes a stochastic model for the impact pressure, showing satisfactory consistency with various literature. In Chapter 4, an analytic solution of the velocity and pressure fields during a surge impact event is proposed based on a well-posed physical model. The self-similarity method is applied there, and the resulting solutions could exactly satisfy the governing equation, the initial condition, and the boundary conditions near the bed. Chapter 5 provides numerical verifications on the results obtained from Chapter 3 and Chapter 4. With a reliable CFD tool, the soundness of the physical assumptions used in Chapter 4 is justified, and the consistency between laboratory and numerical data is demonstrated. Chapter 6 concludes this thesis and indicates some potential future works.

Chapter 2
Literature Review

2.1 Impact pressure generated by liquid-solid interaction

The violent impact between a liquid and solid is a notorious problem in hydrodynamics and many engineering fields. To the author's best knowledge, the pioneer study on this issue was conducted by Von Kármán (1929), where the impact force on landing seaplanes was considered. After that, the study on the liquid-solid impact pressure was split into two branches: liquid impingement onto a solid surface and entry of a solid body into liquid. The present study comprehensively falls into the former branch, and therefore, the author will trace the historical locus of the studies in this branch. A more general literature review on the violet pressure generated by liquid-solid (-liquid) could be found in Dias and Ghidaglia (2018).

The foundational work on the liquid impingement problem was proposed by Bagnold (1939). In this work, the author not only studied the physical process of breaking wave impact onto a solid wall, but also pointed out the uncertainty in the magnitude of the impact pressure. This author concluded that the so-called "air pocket" under the water surface yielded this uncertainty. This work inspired researchers to classify the impact pressure generated by liquid impingement into three different categories (refer to, e.g., Lafeber et al., 2012): shock-induced, hydrodynamic, and (entrapped) gas-induced impact pressure.

The shock-induced impact pressure is closely related to the compressibility of liquid. As a liquid flow suddenly impinges onto a rigid solid surface, the liquid will be slightly compressed, generating the so-called “shock wave”. The evaluation of this kind of impact pressure is notoriously difficult. As far as the author knows, few fundamental theoretical studies could be found in Rankine (1870) and Hugoniot (1887, 1889). The so-called Rankine-Hugoniot solution (RHS) for the one-dimensional shock-induced impact pressure reads:

$$p_i = p_0 + \rho_0 c U \left(1 + O\left(\mathrm{Ma}_0\right)\right) \tag{2.1}$$

where p_i is the impact pressure, p_0 is the pressure before the compression, ρ_0 is the density of the fluid before the compression, c is the speed of sound of the fluid, and U is the incident speed of the fluid here. Ma_0 is the initial Mach number of the fluid, and its value should be small in Equation (2.1). Laboratory measurement of this type of impact pressure is also tricky as the pressure wave travels at the speed of sound of the fluid which is usually a tremendous value. However, as it could be easily derived from Equation (2.1), the compressibility of water is negligible for flows at a speed significantly lower than the speed of sound of the liquid (where the squared Mach number is, say, smaller than 0.1). Therefore, in reality, especially in civil engineering, the compressibility of the liquid is neglected in almost all transient dynamic processes.

The hydrodynamic impact pressure is the most important type of impact pressure in terms of civil engineering works. This type of impact pressure is generated by the sudden change of the velocity field in the incident incompressible fluid flow. Therefore, it is possible to evaluate the impact pressure by investigating the governing equations of

hydrodynamics (e.g., the Euler's equation and the Navier-Stokes equation) analytically or numerically. Foundational analytic works of hydrodynamic impact pressure were conducted by Cumberbatch (1960) and Cooker and Peregrine (1995). These works will be introduced in detail in a later section. As a meaningful reference, the impact pressure generated by the normal water entry of a solid wedge has a definitive solution proposed by Wagner (1932):

$$p_i = C_p \rho U^2 \tag{2.2}$$

$$C_p = \frac{\pi^2}{8 \tan^2 \theta} \tag{2.3}$$

where p_i is the impact pressure, ρ is the density of the fluid, and U here is the entry speed of the solid wedge. C_p is called the "impact coefficient", where θ denotes the angle between the wedge and the liquid surface right before the entry. As presented, there are two governing factors in Wagner's solution (WS), U and θ. It is shown that the impact pressure is proportional to the squared entry speed, U^2. This result has been repeatedly verified in successive works, e.g., Scolan & Korobkin (2003). However, on the other hand, there is an apparent paradox that the impact pressure turns to infinity when θ approaches zero (and Equation (2.3) also becomes suspicious even when θ goes to 90°). As it will be shown in a later section, similar governing factors are used to evaluate the hydrodynamic impact pressure generated by liquid impingement (e.g., Cumberbatch (1960)). Therefore, it becomes necessary to reconsider whether the physical conditions have been soundly considered in these classic theories. Laboratory measurement of this type of impact pressure is also possible using pressure sensors at low costs. Due to these conveniences, hydrodynamic impact pressure is the most frequently studied one among the three categories. In coastal and ocean engineering, many studies on this type of impact pressure

were conducted for water surface wave impingement onto structures (Blackmore & Hewson 1984, Kirkgoz 1982, 1990, Oumeraci et al., 1993, Hattori et al., 1994, Bullock et al., 2001, Shu 2004, Cuomo et al., 2011). Surge-induced impact pressure also falls into this category, and many fruitful works are introduced later, though with some unsolved issues.

Impact pressure could also be generated by the entrapped gas under the liquid surface. In that case, the gas pockets are squeezed by the surrounding liquid. This phenomenon results in oscillatory pressure on the solid surface, and the magnitude of the impact pressure is indefinite and might be influenced by the size of the gas pockets (Bagnold 1938, Bredmose et al., 2009, Bredmose et al., 2015). The so-called Bagnold's solution (BS) for the impact pressure reads:

$$\left(\frac{p_0}{p_i}\right)^{\frac{1}{\gamma}} + \frac{1}{\gamma-1}\left(\frac{p_i}{p_0}\right)^{\frac{\gamma-1}{\gamma}} = S + \frac{\gamma}{\gamma-1} \tag{2.4}$$

$$S = \frac{m_l U^2}{2 p_0 \Omega_0} \tag{2.5}$$

where p_0 is the initial pressure of the gas (air, in the case of Bagnold (1939)) and γ is the adiabatic exponent. S is the so-called "the impact number", where m_l is the mass of the liquid (water here), U is the incident velocity of the fluid flow, and Ω_0 is the initial volume of the entrapped gas pocket. It could be understood that the value of Ω_0 is very hard to define in actual applications; even other parameters could be relatively well controlled. A typical example of this type of impact pressure could be found in plugging wave breakings (Bagnold 1939, Kirkgöz and Mamak 2004, Bogaert et al., 2010, Kimmoun et al., 2010). Following this well-known example, gas-induced impact pressure

is sometimes called the “flip-through” pressure. To empirically solve the above-mentioned uncertainty in the magnitude of impact pressure generated by water waves, Klammer et al. (1997) and Allsop et al. (1997) used stochastic distributions to describe this parameter for engineering works. These stochastic models actually inspired the author of this thesis to conduct a similar analysis on the surge-induced impact pressure. However, as demonstrated by laboratory works, it has to be remarked here that aeration does not play an important role in the surge-induced problem (Lobovský et al., 2014, Xie and Shimozono 2022), and the source of stochasticity of it has not been revealed yet.

The following table presents a summary of the above-mentioned categories of the impact pressure generated by liquid impingement onto a solid surface. The parts colored in red are set to be the research targets of the present study. A detailed review of these specific topics will be presented in a later section.

Table 2.1 Summary of different categories of the impact pressure generated in liquid impingement

Categories	Shock-induced	Hydrodynamic	Gas-induced
Analytical solution	RHS	Water impingement: Cumberbatch (1960), Cooker & Peregrine (1995) Water entry (reference): WS	BS
Laboratory observation	Difficult	Possible	Possible
Aeration	None	Small	Large
Compressibility	liquid	None	Gas
Stochasticity	Unknown	Yes, not yet formulated	Yes, formulated

2.2 Surge-induced impact pressure

The surge-induced impact pressure on a solid surface falls into the category of "hydrodynamic" in Table 2.1. Therefore, many fruitful studies have been conducted on this topic. As introduced in Chapter 1, there are mainly three approaches for studying the surge-induced impact pressure. In this section, the author will present a number of representative works in each approach, showing what difficulties have been overcome and what are still unsolved.

2.2.1 Laboratory studies

This sub-section is based on the published work of Xie and Shimozono (2022).

Many organizations in different countries have proposed guidelines with empirical formulas for engineers to predict the pressure induced by water surges (e.g., ASCE 2017 and FEMA 2019). These formulas are based on the past laboratory experiments conducted by a number of researchers under different experimental conditions (e.g., Ramsden 1993, 1996 and Asakura et al., 2002). A simple but comprehensive summary of these can be found in the study by Yeh et al. (2014). However, these authors and guidelines have suggested different formulas or even made different qualitative descriptions of surge pressure. For example, Ramsden (1993) claimed that there is no obvious impact pressure peak for the surges that travel on a dry bed. However, many recent laboratory studies have rebutted this statement with plenty of experimental data (these recent works are

introduced later), showing that the hydrodynamic impact pressure peak exists assuredly. As another example, Asakura (2002) proposed a predictive formula for evaluating the surge-induced impact pressure on a vertical wall, which reads:

$$p_i = \alpha \rho g \eta_{\max} \tag{2.6}$$

where $\eta_{\max}$ is the highest water level without the presence of the wall, and α is a variable coefficient whose value is no larger than 3. As Equation (2.6) presented, this formula evaluates the impact pressure using the expression of hydrostatic pressure. However, one of the engineering guidebooks, FEMA 2019, suggested a completely different formula for the impact pressure (a simple derivation of this formula is presented in Chapter 4):

$$p_i = 2.25 \rho U^2 \tag{2.7}$$

where U is the incident surge front velocity. Equation (2.7) follows the conventional assumption that the impact pressure is proportional to U^2. Obviously, Equation (2.6) and (2.7) use different physical parameters to quantify the impact pressure. However, as mentioned in Chapter 1, the impact pressure should be determined by the status of incident flow right before the impingement. Therefore, in this context, Equation (2.7) is in a more acceptable form, although Equation (2.6) is also consistent with specific data sets.

In recent years, several laboratory studies under various experimental conditions have been published (e.g., Robertson et al., 2008, Nouri et al., 2010, Al-Faesly et al., 2012, Robertson et al., 2013, Douglas and Nistor 2014, Lobovský et al., 2014, Kihara et al., 2015, Kihara and Kaida 2016, 2019, Xu et al., 2021, Shen et al., 2020 and Chuang et al., 2020). These works not only investigate the impact pressure applied on structures but also

provide detailed information on incident surge, e.g. the surge front velocity and water surface elevation right before the impingement. In these works, highly sensitive pressure sensors and high-speed video cameras were the main devices to accurately collect the data. Also, as an associated issue, surge-induced forces on different types of structures have also been investigated by several authors (e.g., Arnason 2009, Nouri et al., 2010, Robertson et al., 2013 and Wüthrich et al., 2018).

As introduced in the previous section, the uncertainty in the impact pressure generated by wave breaking has been studied quantitatively with stochastic distribution models. On the other hand, the carefully controlled experiments of Lobovský et al. (2014) have revealed that the magnitude of pressure during water surge impingement is also stochastic and cannot be described by deterministic predictive formulas. These authors repeated the experiments under the same experimental conditions 100 times in a small-scale flume. Stochastic distributions of the impact pressure were accurately obtained at different locations on the structure (a vertical wall). However, no predictive formula based on their stochastic analysis has been proposed. Furthermore, the fluid phenomena underlying the stochasticity have not been elucidated. As far as the author of this thesis knows, no stochastic model has been proposed for surge-induced impact pressure.

2.2.2 Analytical works

As introduced in Chapter 1, there are mainly two ways to analytically deal with the surge-impingement problem: the self-similarity method and the pressure impulse method. These two methods provide two different standing points of solving the problem. The

self-similarity method looks into the physical parameters from the view of differential form. In contrast, the pressure impulse method solves the physical parameter in the integrated form.

We first review the pressure impulse method. The concept of pressure impulse in hydrodynamics has been mentioned in some books in early ages (e.g., Lamb 1932 [Chapter I-11], and Batchelor 1973 [Chapter 6-10]). However, the usage of this concept for the liquid impact problem was originated in a later work by Cooker and Peregrine (1995). The pressure impulse is defined as

$$P(x,y)=\int_{t_a}^{t_b} p(x,y,t)\,dt \tag{2.8}$$

where x and y are the cartesian coordinates, t_a and t_b are the times immediately before and after impact, respectively. p (x, y, t) is the pressure distribution in the fluid region. The value of t_b - t_a is assumed to be small enough so that an evaluation of the pressure impulse P (x, y) is sufficient for actual applications (also refer to Ghadirian and Bredmose 2019). In the work of Cooker and Peregrine (1995), the following physical model has been studied under the assumption that the advection terms in the velocity field are negligible compared with the time derivatives.

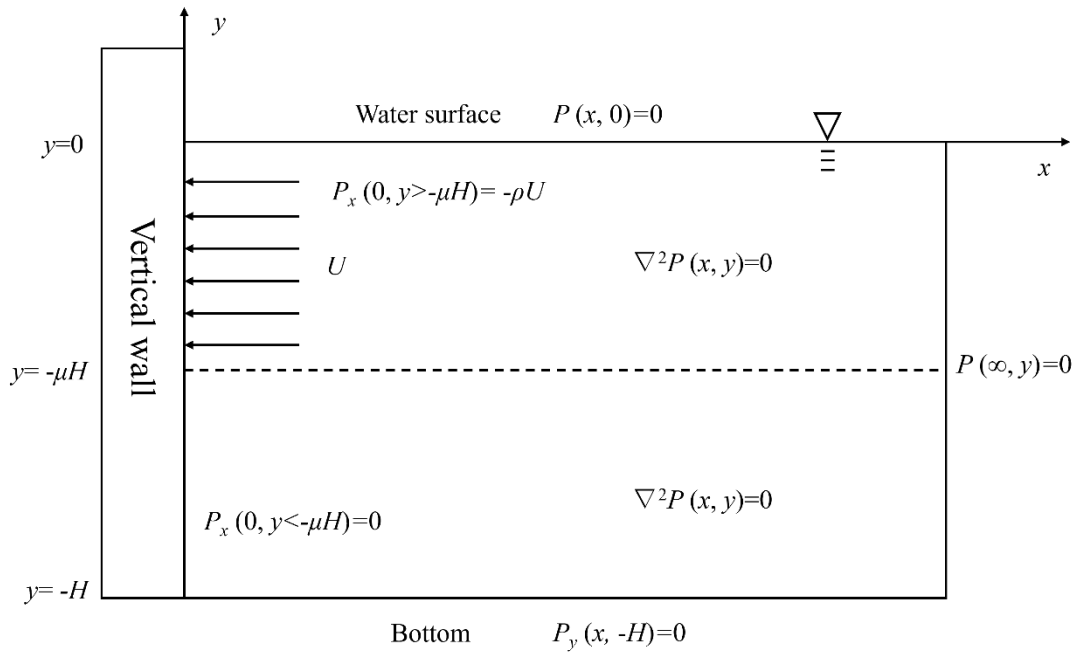

Fig. 2.1 Physical model used in Cooker and Peregrine (1995)

It could be understood from Figure 2.1 that although the authors divided the fluid region into two parts, the pressure impulse in each part could be obtained from an elliptic equation with clearly defined boundary values. As the governing equation is linear, many powerful mathematical tools (e.g., Fourier analysis) could be applied. Owing to the simple structure of the physical model, the work of Cooker and Peregrine (1995) was expanded into many three-dimensional applications with more complicated boundary values (e.g., Wood and Peregrine 1998, Chatjigeorgiou et al., 2016, Ghadirian and Bredmose 2019). The effects of turbulence involved in the incident flow were also studied by several authors (e.g., Thao et al., 2007). However, it has been proved by several laboratory works (Bagnold 1939, Kirkgöz and Mamak 2004, Lobovský et al., 2014, Chuang et al., 2020) that the impact duration, t_b - t_a, is a highly stochastic parameter. Therefore, although its value is usually very small, it could significantly affect the value of pressure peak enveloped in the integrated form, Equation (2.8). It could be said that

the pressure impulse method is an outer approximation to the impact pressure in this context.

As a parallel method to the pressure impulse, the self-similarity method has a longer history, and it was first used by Cumberbatch (1960). In this foundational work, the motion of water particles during the impact was assumed to be irrotational, and therefore the velocity potential theory was applied. The author proposed the following self-similarity variables in the derivations.

$$\lambda = \frac{x}{Ut} \quad , \quad \mu = \frac{y}{Ut} \tag{2.9}$$

$$\Phi(x,y,t) = tU^2\phi(\lambda,\mu) \quad , \quad \psi = \phi(\lambda,\mu) - \frac{1}{2}\left(\lambda^2+\mu^2\right) \tag{2.10}$$

$$\eta(x,t) = tU\xi(\lambda) \tag{2.11}$$

where Φ is the velocity potential, and η is the location of the free water surface. The physical model of this study is shown in Figure 2.2, where a water wedge with angle θ normally impinges onto a horizontal plate.

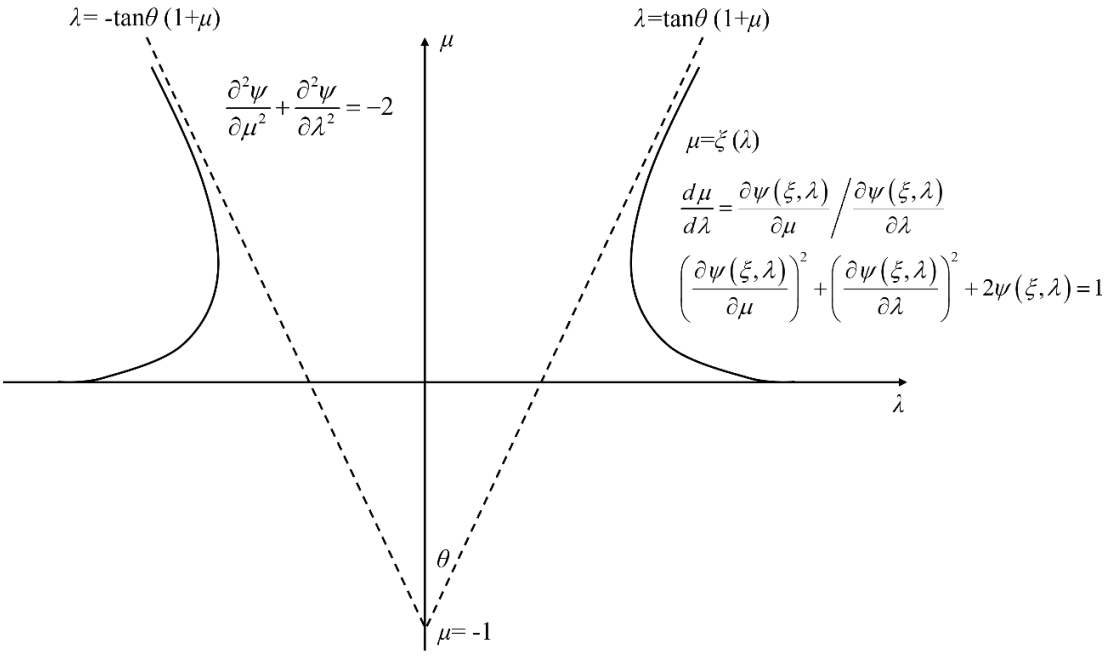

Fig. 2.2 Physical model used in Cumberbatch (1960)

From Figure 2.2, we can see that the governing equation of the velocity potential is also an elliptic equation. However, the boundary conditions have become nonlinear and in very complicated forms. Therefore, it is far more difficult to derive an analytic solution for the velocity field under this physical model than the pressure impulse method. After some simplifications and approximations, a predictive formula for the impact pressure was proposed:

$$p_i(\lambda) = \rho U^2 C_p(\theta)\left[1-\left(\frac{\lambda}{\lambda_w(\theta)}\right)^2\right] \tag{2.12}$$

where the impact coefficient C_p is a function of the incident wedge angle, and its value could be determined numerically. λ_w is the location of the water surface on the plate. Note that the applicable range of this analytic solution is $0 < \theta < \pi/4$. Figure 2.3 shows the value of C_p and λ_w.

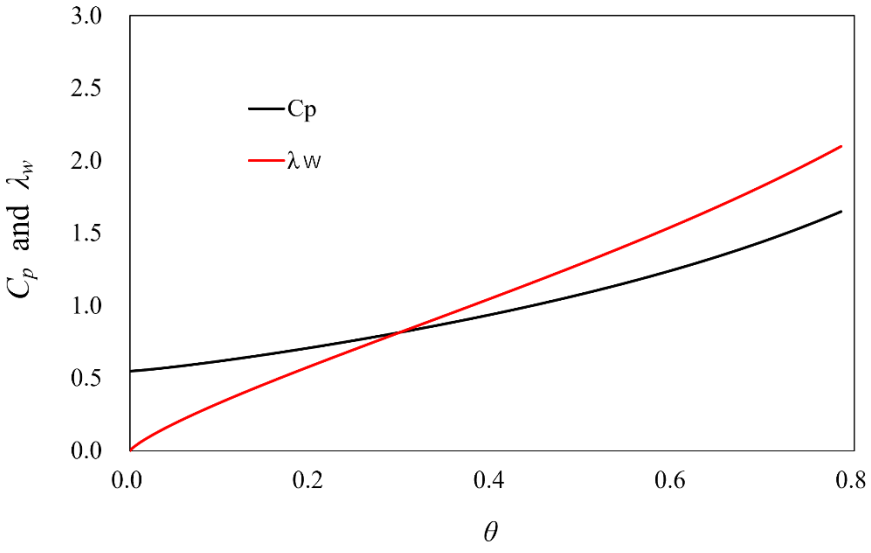

Fig. 2.3 Relationship between C_p, λ_w and θ

As mentioned in Chapter 1, an apparent advantage of the self-similarity solution is that the singularity in the velocity field when t approaches zero is explicitly involved in the formulations. For the impact pressure, similar to Wagner's solution, Equation (2.12) also suggests that the governing factors of the impact pressure are U^2 and θ. However, from Figure 2.3, we could still point out the peculiar behavior of C_p when θ approaches zero, where the value of C_p turns to 0.5, the well-known value of the pressure in steady flows. This issue has motivated the author of this thesis to reconsider: whether the literature have correctly described the physics of surge impact.

Following the work of Cumberbatch (1960), a series of self-similarity solutions for describing the impact pressure were proposed. Cross (1967), Kihara et al. (2015) and Kihara and Kaida (2016) took the gravitational term into account, which was neglected in Cumberbatch (1960). Many researchers derived the self-similarity solution for liquid impact with more complicated geometries (e.g., Wu 2007, Duan et al., 2009, Semenov and Wu, 2013). Nevertheless, the framework of those studies was originated in Equation (2.9) – (2.11).

2.2.3 Numerical calculations

With the rapid development of CFD, it has become possible for people to conduct numerical calculations to evaluate the hydrodynamic impact pressure. This section presents some basic descriptions of the CFD tools that have been applied to simulate the liquid impingement process. As the author of this thesis only takes advantage of a

commercial CFD software to verify the results from laboratory works and theoretical analysis, details such as the algorithm and scheme construction are not presented here.

For the hydrodynamic impact pressure, the incompressible Navier-Stokes equation is usually selected as the governing equation in numerical models (refer to Dias and Ghidagria 2018). A number of sophisticated solvers and software have been released for users to calculate the velocity and pressure fields during the surge impingement swiftly and accurately. For example, ANSYS Fluent and OpenFOAM are popular CFD tools to simulate various liquid-solid impact phenomena (refer to Wei et al., 2016, Henry et al., 2014, Sarjamee et al., 2017). Most of the available numerical models have some common characteristics:

1. The classic finite-difference or finite-volume method is used to discretize the governing equation.
2. The VOF (Volume of Fluid) method is applied to track the motion of the free water surface (Heyns et al., 2013)
3. The two-equation model, usually the *k-e* model, is used to generate turbulence (originated in the work of Kolmogorov, 1942).

A brief review of these characteristics could be found in Sarjamee et al. (2017). When simulating the highly transient flows along an abruptly curving surface numerically, it has been reported that significant losses of momentum and kinetic energy could occur (Mampaey and Xu 1995). This difficulty has been recently overcome by a CFD solver, Flow-3D, where a unique model FAVOR^{TM} has been specifically applied to ensure that no momentum is lost along a sharply changed surface. Although the above-mentioned numerical tools can provide people with accurate numerical results of impact pressure, it

is also notable that the calculations are sometimes extremely time-consuming (the CPU time is usually no less than the order of 10^4 s). The reason is that, in order to capture the highly transient and localized impact pressure, the mesh size and the time step have to be tiny enough. There is currently no solution to this awkward situation, and therefore, the numerical calculations of impact pressure are usually conducted for small-scale problems. Also, to the best knowledge of the author of this thesis, as of now, there is no numerical model capable of evaluating the instabilities in the free water surface. Nevertheless, it will be seen in Chapter 3 that those kinds of instabilities are potentially responsible for the uncertainty in the magnitude of surge-induced impact pressure.

Chapter 3

Laboratory experiments on surge impingement process and stochastic analysis on the impact pressure

This chapter is based on the published work of Xie and Shimozono (2022).

3.1 Introduction

This chapter presents a laboratory experimental work and a stochastic analysis on the surge impingement process.

As introduced, many authors have conducted laboratory works to reveal the characteristics of the surge impact process. Based on these works, people have proposed various deterministic formulas to evaluate the magnitude of surge impact pressure onto structures, using various physical parameters that appeared in the laboratory works. Most of these formulas could quantitatively predict the experimental data collected on the structures in the corresponding laboratory works but disagree with the data from other literature. Nevertheless, most of the formulas suggested similar qualitative characteristics of the surge impact pressure, showing that they have partially captured the nature of it indeed.

The main reason for the situation mentioned above is that the authors did not include stochasticity in their formulas. In that case, although the basic qualitative correlations

among the physical parameters could be figured out with limited laboratory data, significant biases on the quantitative evaluations were inevitable. On the other hand, although the stochasticity of surge impact pressure has been repeatedly confirmed recently, there is still no formula that could describe it as of now. Therefore, in this chapter, I attempt to obtain an explicit stochastic model to fill up this gap, showing that the data of various literature might be consistent with each other under this model. For this purpose, carefully controlled laboratory experiments are carried out to provide sufficient experimental data.

Section 3.2 describes the experimental setup and the devices employed in the laboratory work. It is shown that the dam-break experiments are carefully controlled, and the devices are capable of collecting reliable data. In Section 3.3, the experimental results of surge front velocity, surge front shape and the impact pressure applied on a vertical panel are presented. The stochasticity is found not only in the impact pressure but also in the incident surge flows, despite that the experiments are repeated with almost exactly the same initial conditions. In Section 3.4, I attempt to propose a stochastic model for the data using the so-called Fréchet distribution based on the experimental results. The resulting empirical formulas could give satisfactory correlations for the data in the present study and the experimental data randomly collected from various literature. In this section, the relationship between the impact pressure and the surge front slope is also discussed with the analytic theory proposed by Cumberbatch (1960). Section 3.5 summarizes some main findings of this chapter and leads the discussions into the later chapters.

3.2 Experimental setup and devices

3.2.1 Flume setup

The laboratory experiments are conducted at the University of Tokyo. As presented in Figure 3.1, the main experimental device is an acrylic flume equipped with a sluice gate on one side and a vertical acrylic panel on the other side. Water is filled in on the left-hand side of the gate when the gate is at the lowest position (closed). After the gate opening, the water is released and impinges onto the vertical panel. Figure 3.2 shows a sketch of the experimental setup with (x, y) coordinates.

Fig. 3.1 Photograph of the experimental flume.

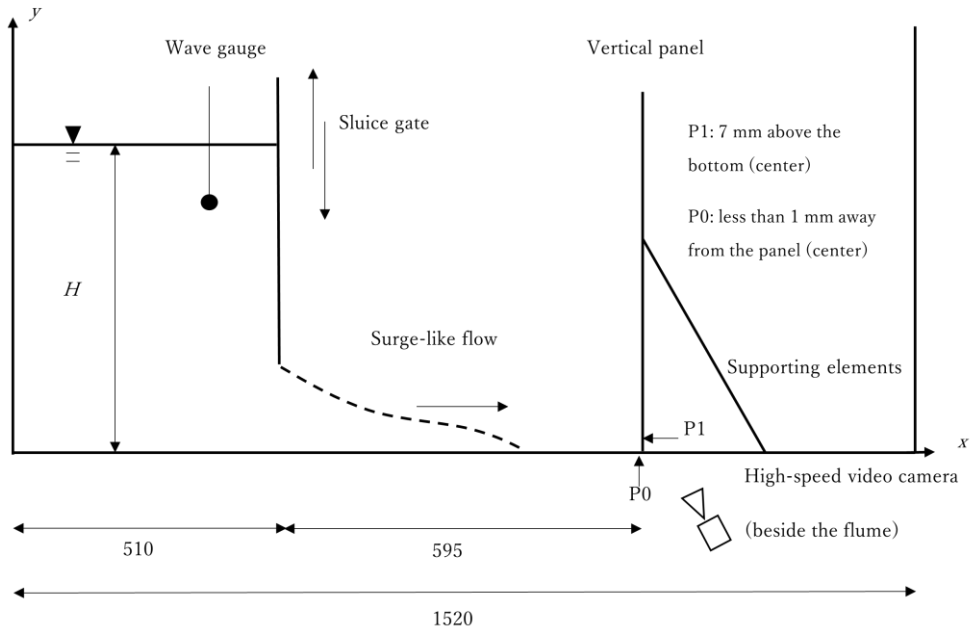

Fig. 3.2 Sketch of the experimental setup (vertically exaggerated, length in mm).

A cuboid acrylic flume of 1,520 × 420 × 450 mm is built specifically for the present study with a precision of 1 mm. Similar small-scale flumes have been utilized for dam-break experiments in the literature (e.g., Lobovský et al., 2014). The flume sides, composed of 10-mm-thick acrylic plates, are perfectly perpendicular to each other at the joints. Two sliding rails for the sluice gate are ditched on the sides of the flume with a 10.5 mm width. There are two circular openings with a 10 mm diameter on the central axis of the flume bottom. The opening positioned at (905, 0) in Figure 3.2 is used for drainage (sealed during experiments), and the one at (1105, 0) is used for equipping a pressure sensor.

The sluice gate used is a 10-mm-thick acrylic plate of 495 × 409 ×10 mm. It is positioned at x=510 mm, as presented in Figure 3.2. This sluice gate fits and slides well along the rails due to the silicone lubricant sprayed onto its side edges. A waterproof seal

is applied on the bottom of the sluice gate, ensuring no water leakage before the gate opens. The gate could be vertically opened by releasing a weight from a height of around 15 cm. Therefore, the maximum opening height of the gate is 15 cm, and the initial water level behind the gate, H, should be set not to exceed this height. The average moving speed of the gate is around 1.2 m/s to ensure that the rising time of the gate is shorter than the upper limit to generate dam-break flows,

$$t_c = 1.25\sqrt{\frac{H}{g}} \tag{3.1}$$

according to Vischer and Hager (1998), where g is the gravitational acceleration. A number of authors have reported that the gate speed could potentially affect the characteristics of dam-break flows (Lobovský et al., 2014, Takagi and Furukawa 2021). However, this issue is not considered in the present study since I measure the incident surge parameters in each run of the experiment.

A vertical acrylic panel (495 × 395 × 10 mm), on which the pressure is measured, is positioned at x=1105 ± 1 mm. The front face of the panel is right above the opening located at (1105, 0). Two acrylic supporting elements are employed behind the panel, ensuring that it does not move from its initial position during the water surge impingement.

3.2.2 Instruments setup

There are four pressure sensors (P310V-01, produced by SSK Co., Ltd) located at y=7, 37, 67 and 97 mm along the central axis of the vertical panel. They are perfectly inserted into the four circular openings, providing a flat front face for the panel. Another pressure

sensor is installed in the opening at (1105, 0), right beneath the panel. The diameter of each pressure sensor is 10 mm; their designed hysteresis (non-linearity) is 0.5% RO, and the repeatability is 0.2% RO, according to the manufacturer. The maximum capacity of the pressure sensors is 10 kPa, and the sampling rate is set to 500 Hz (refer to Appendix A for further information on this sampling rate). In the present study, I only focus on the pressure sensors located at (1105, 0) and (1105, 7) (denoted by P0 and P1 hereby), as presented in Figure 3.2. The reason is that the maximum surge-induced pressure is most likely occurs at the corner (refer to Kihara and Kaida 2019, Lobovský et al., 2014)

A high-speed video camera (k8-USB, produced by KATO KOKEN) is used to record the impingement process from beside the flume. The number of pixels in one frame is set to 800 × 600, the shutter speed is 1/5,000 s, and the frame rate is 500 fps. This video camera is able to capture the water motions during the impingement, as will be shown in a later section.

In addition, a wave gauge (with a sampling rate of 500 Hz) is employed inside the sluice gate (see Figure 3.1) to record the changes in the water level. The measured data are mainly used to detect the moment the sluice gate opens.

The pressure sensors and the wave gauge are connected to a data acquisitor (A/D Atsume-Taro, KENEK), and therefore they are precisely synchronized with each other. As the sluice gate opens, the water surface inside the gate is immediately disturbed, and the wave gauge accurately captures this moment. On the other hand, the high-speed camera also visually captures the moment of the gate opening. Therefore, the pressure

sensors and the high-speed camera are synchronized using the wave gauge as an intermediary with a precision of 0.002 s.

3.2.3 Experimental cases

I investigate the impingement process in four different cases by changing the initial water level behind the sluice gate, H. Considering the maximum opening height of the gate, which is around 15 cm, I set H = 8, 10, 12 and 14 cm. Each case is repeated 24 times (runs) so that the stochastic properties of the surge impingement could be studied.

Figure 3.3 presents a typical side view of the surge generation, propagation and impingement, starting from the gate opening until the impact stage. Figure 3.4 presents a typical overhead view of the same process. The photographs in Figure 3.3 and 3.4 are recorded using a compact video camera (Victor GZ-HD40, 30 fps and shutter speed of 1/2,000 s) in order to present an overall view of the experiment. As can be seen from Figure 3.4, it is notable that the surge front is parallel to the panel but produced some finger-like patterns in the transverse direction. This phenomenon, usually referred to as fingering, occurs at the contact line when a flow with a high Reynolds number is traveling on a dry bed (Jánosi et al., 2004). A finger can merge with an adjacent finger or split into two fingers actively during the propagation, and these processes are highly stochastic (Thoroddson and Sakakibara 1998). The fingering patterns become more obvious after the surge impingement on the panel (also refer to Kondic 2003). Figure 3.5 presents a zoomed-in view of the surge front shape right before the impingement for each case (recorded by the high-speed video camera, with a precision of 0.002 s).

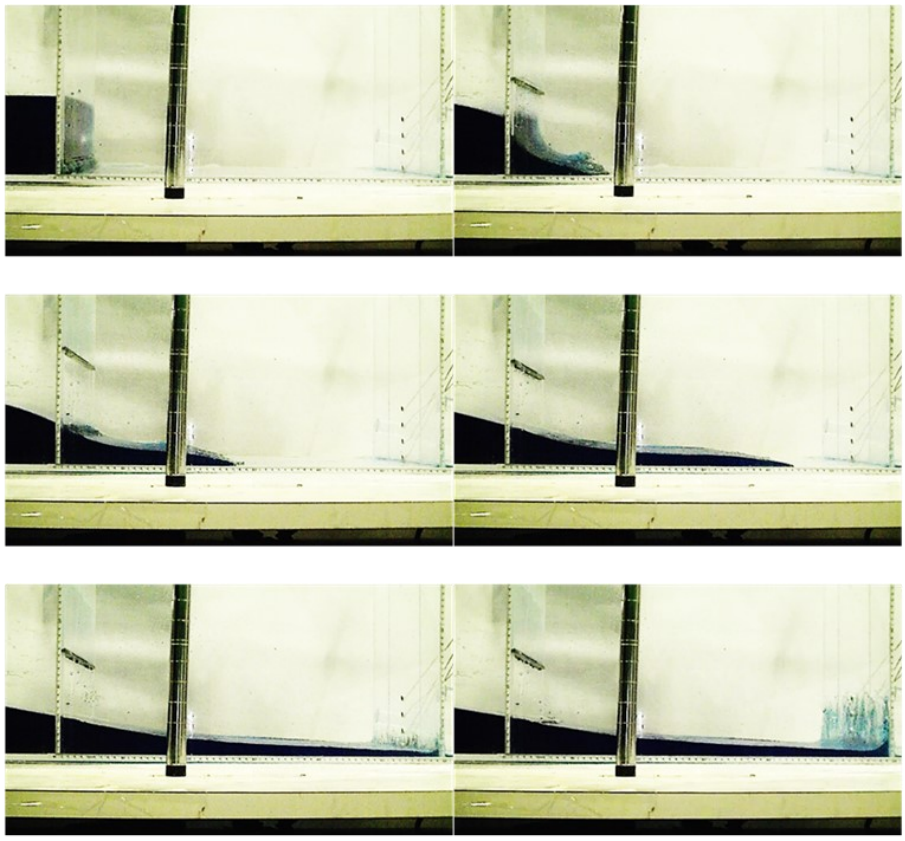

Fig. 3.3 Typical fluid motion during the dam-break experiment (H = 12 cm) 0.033 s (top left), 0.133 s (top right), 0.233 s (middle left), 0.333 s (middle right), 0.433 s (bottom left) and 0.467 s (bottom right) after the sluice gate opening.

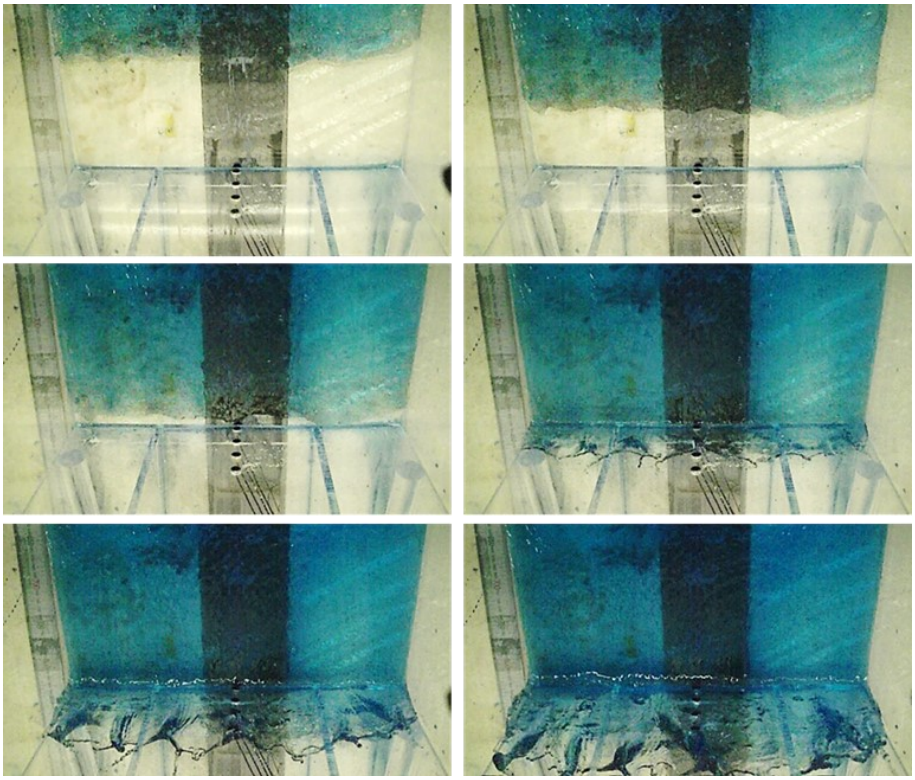

Fig. 3.4 Typical surge front during an impingement event (H = 12 cm, overhead view) 0.333 s (top left), 0.367 s (top right), 0.400 s (middle left), 0.433 s (middle right), 0.467 s (bottom left) and 0.500 s (bottom right) after the sluice gate opening.

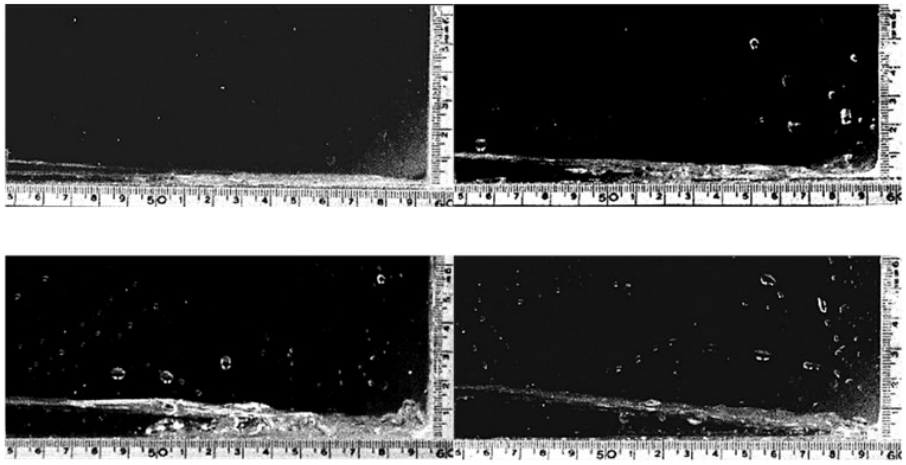

Fig. 3.5 Typical surge front shape right before the impact with H = 8 cm (top left), H = 10 cm (top right), H = 12 cm (bottom left) and H = 14 cm (bottom right).

By using the pressure sensors and high-speed video camera, I record the time history of the pressure applied on the panel, the surge front velocity, and the surge shape right before the impact for each run in each case.

3.3 Experimental results

3.3.1 Time history of pressure on the vertical panel

In the present study, I focus on the time history of the pressure at P0 and P1 to study the stochastic properties of the surge impingement in the initial stage. The effect of gravity is considered negligible during the first impact at these locations (refer to Lamb 1932, Chapter I-11). In a later section, I will investigate the difference between the pressure at P0 and P1. Figure 3.6 and 3.7 present the time history of the pressure at P0 and P1 in each case.

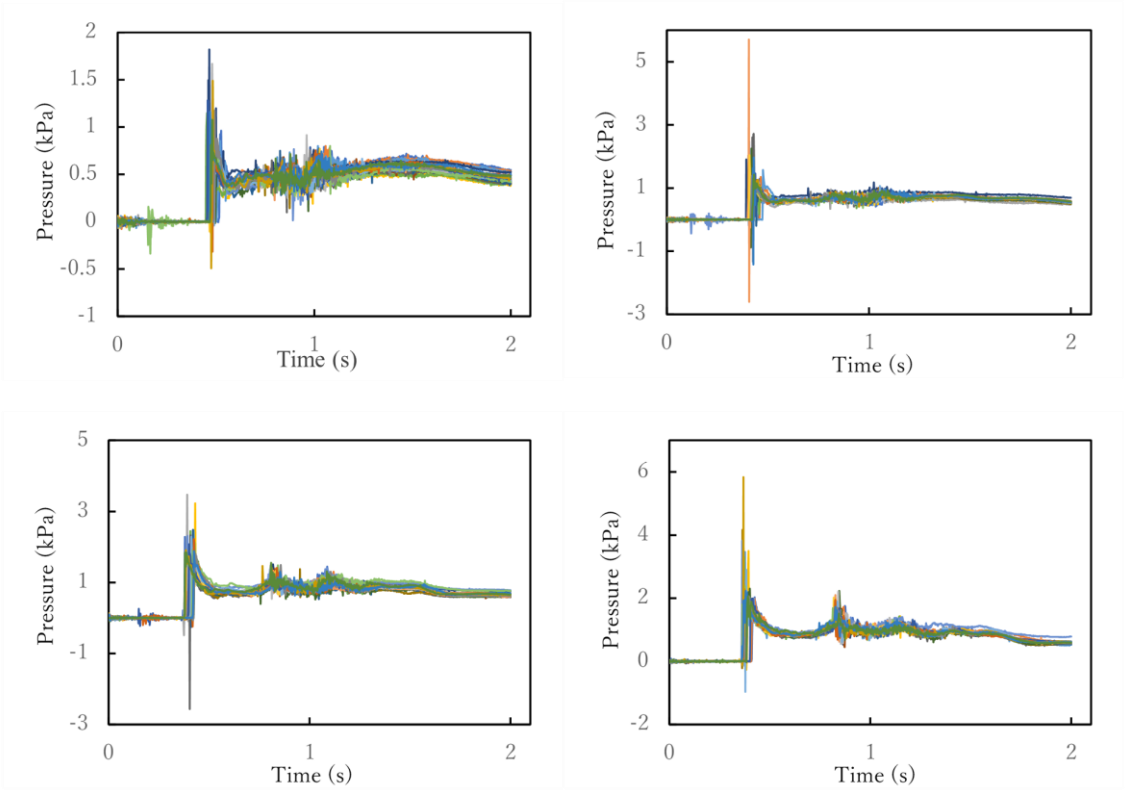

Fig. 3.6 Time history of pressure applied on P0 with H = 8 cm (top left), H = 10 cm (top right), H = 12 cm (bottom left) and H = 14 cm (bottom right).

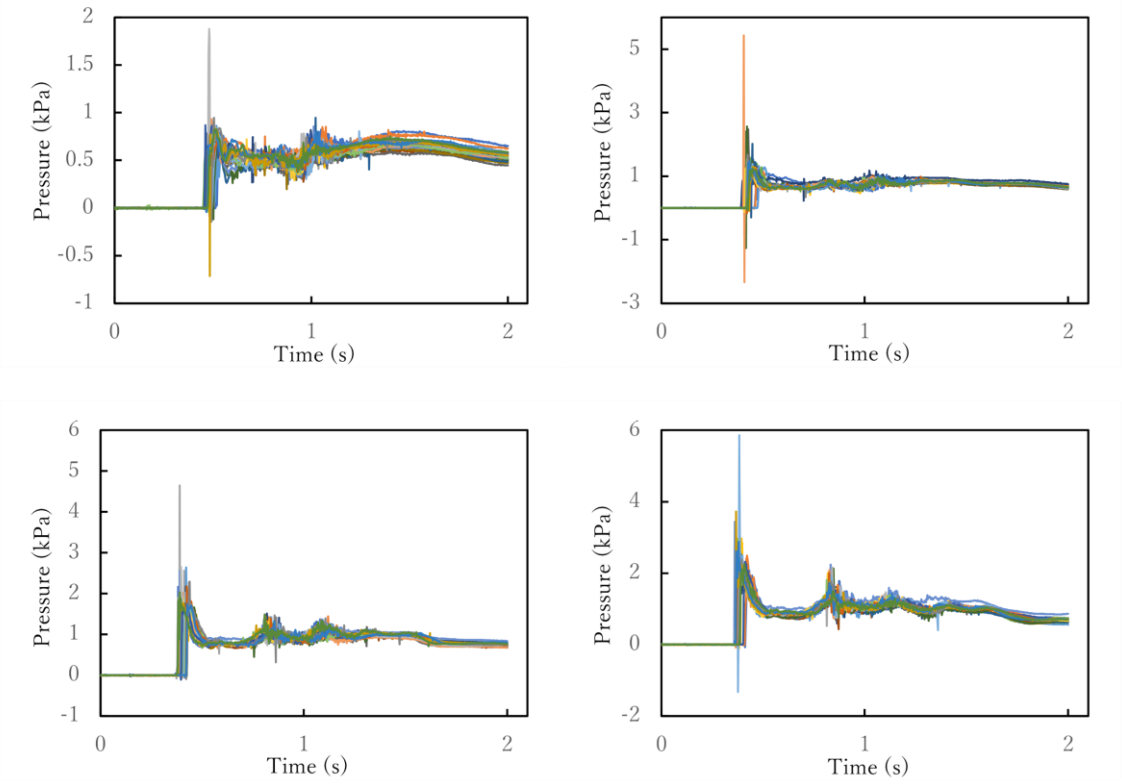

Fig. 3.7 Time history of pressure applied on P1 with H = 8 cm (top left), H = 10 cm (top right), H = 12 cm (bottom left) and H = 14 cm (bottom right).

In these figures, the time origin (t = 0 s) is defined as the moment the sluice gate opens. All the time series end at t = 2 s before the re-reflected wave from the left side reaches the panel. The arrival time of the surge fronts on the panel demonstrates high repeatability in each case. The pressure time series of different runs generally agree on their shapes (the correlations among these curves will be demonstrated and investigated in Appendix B), but the peak values are distributed over relatively wide ranges. There is a pressure peak right after the arrival of the surge front in each run (the impact stage), hereinafter

referred to as the impact pressure. In almost all runs, the impact pressure is the maximum pressure in the entire time span. The second pressure peak appears when the run-up water starts to be yanked back by gravity (the run-up stage). Although this second pressure peak is smaller than the impact pressure, a number of previous studies have reported that the force applied on the vertical structure (the run-up force) reaches the maximum at this stage (Al-Faesly et al., 2013 and Nouri et al., 2010). In the present study, I mainly discuss the properties of the impact pressure. The magnitude of the impact pressure peak agrees with past experiments, and a comparison will be shown in a later section.

3.3.2 Distribution of the impact pressure

As mentioned in the previous section, although the time history curves of the pressure generally share the same shape, the values of the impact pressure widely ranged. To show the characteristics of the pressure distribution over the different runs, I plot the cumulative percentile ranking graphs of the impact pressure for each case in Figure 3.8.

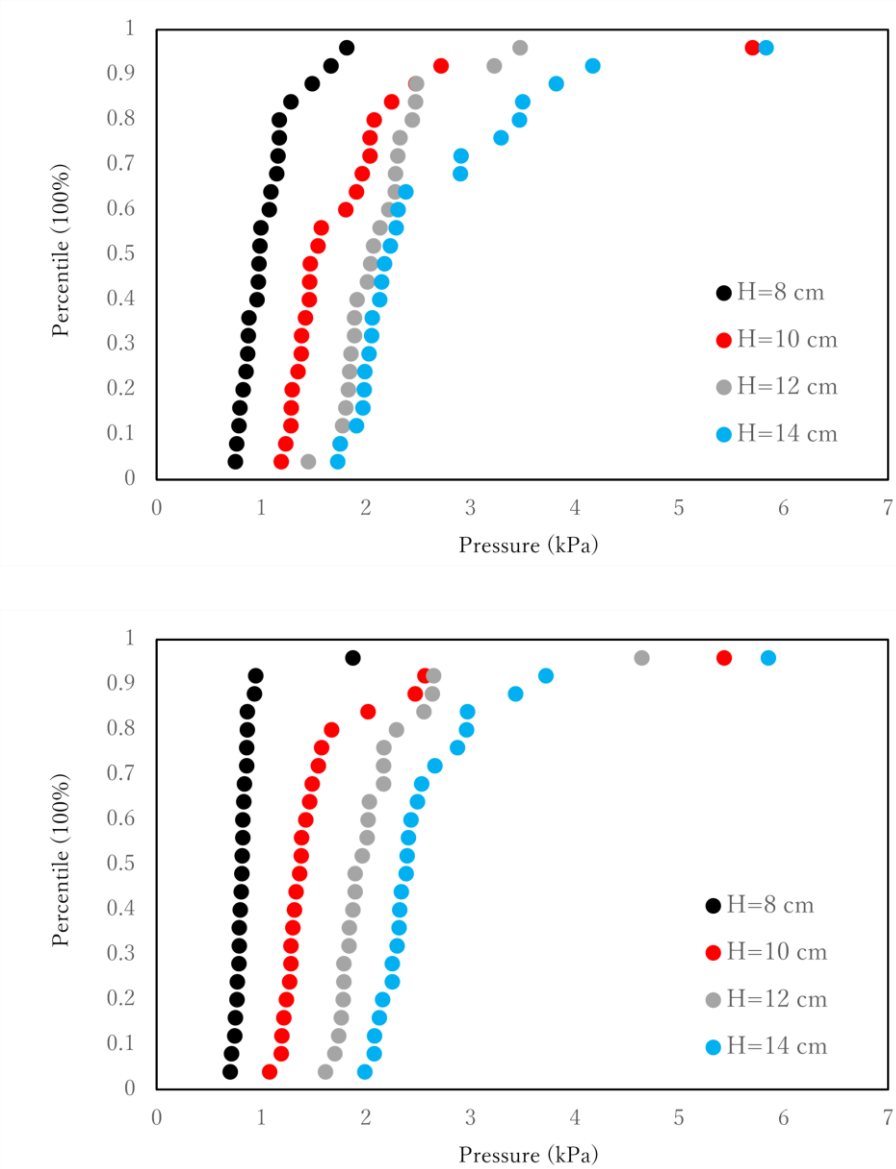

Fig. 3.8 Cumulative percentile ranking graphs of the impact pressure in different cases at P0 (top) and P1 (bottom).

In each case, most plots concentrate around a certain mode value, with some significantly larger than others. However, no extremely small pressure is confirmed from the data. This distribution type is often called ‘fat-tailed’ in statistics, and it usually falls into one of the extreme value distribution models. A similar pressure distribution shape was also obtained

by Lobovský et al. (2014). This fat-tailed distribution is possibly an inherent property of the impact pressure. One of the possible reasons for it may be the fingering phenomenon described in Section 3.2.3. As the fingering patterns at the surge front actively evolve during the surge propagation, fluid particles at the fingers may have gained additional (but short-life) velocity components to the general surge front velocity locally. When a finger impinges on the pressure sensor, the impact pressure could have been significantly magnified. However, in the present study, I do not pursue further details of the fingering patterns but regarded them as a possible source of uncertainty and stochasticity of the impact pressure.

It is not surprising that a higher impact pressure results from a surge generated with a higher water level behind the gate. The median or mode value could be more suitable as a representative value than the mean value owing to the presence of the extreme values. These statistical parameters and a stochastic model for the impact pressure will be discussed in a later section.

Figure 3.9 presents the relationship between the impact pressures at P0 and P1 without distinguishing the cases. It suggests that the measurements of the pressure at P0 and P1 had a high positive correlation. In addition, it could be understood from the slope of the linear fitting curve that the impact pressure at P0 (which is exactly at the bottom) is generally larger than the impact pressure at P1 (which is above the bottom).

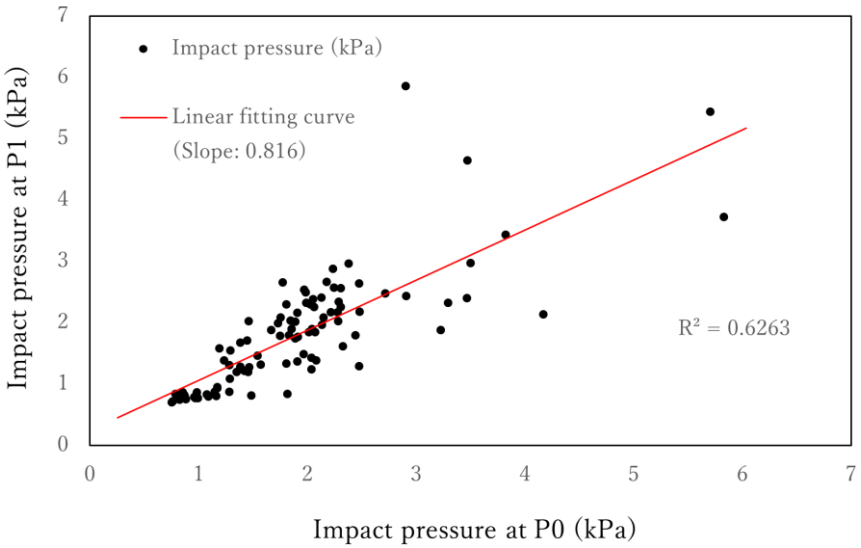

Fig. 3.9 Relationship between the impact pressures at P0 and P1.

3.3.3 Distribution of surge front velocity

The surge front velocity, U, of each run is obtained through a careful analysis of the videos taken by the high-speed video camera beside the flume. I calculate the surge front velocity right before the impact by measuring the time difference between the impact and the moment the surge front passes the location 10 cm away from the panel (with a precision of 0.1 cm and 0.002 s). Although this method includes some uncertainties of the fingering patterns mentioned in Section 3.2.3, it could describe the general moving speed of the surge front. The theoretical velocity of the surge front velocity was given by Ritter (1982) as $U^2 = 4gH$. However, it is commonly known that this formula significantly overestimates the surge front velocity and U^2/gH varies under different experimental conditions (refer to Dressler 1954, Koshizuka and Oka 1996, Hu and Sueyoshi 2010 and Shen et al., 2020). In the present study, U^2/gH is around 1.96 in each case. Figure 3.10

presents the cumulative percentile ranking graph for the squared dimensionless surge front velocity, U^2/gH, in each case. The primary reason for the difference between the experimental data and the theory is the energy dissipation during the propagation. In Chapter 5, I will discuss this issue with numerical method.

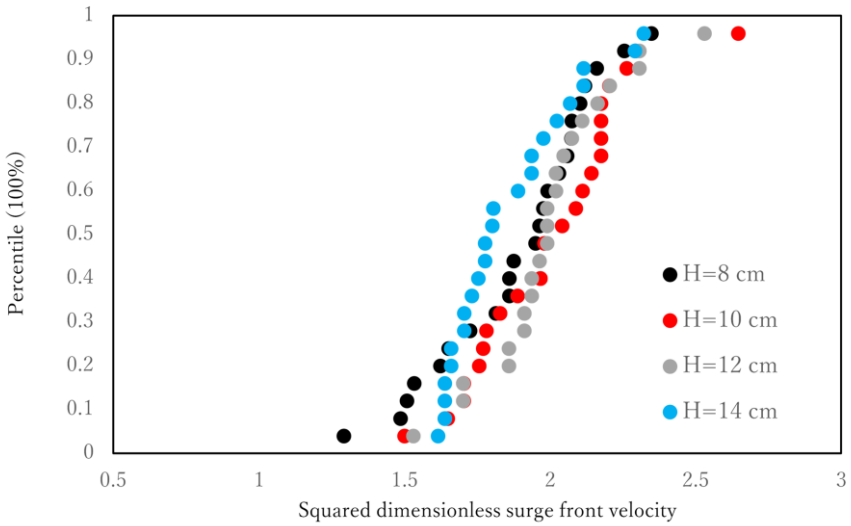

Fig. 3.10 Cumulative percentile ranking graph of the squared dimensionless surge front velocity in different cases.

Almost all points in Figure 3.10 concentrate around a certain mode value without extreme data contrary to the pressure distribution. The deviations from the mode potentially result from measurement uncertainties, the variability of the gate speed (Takagi and Furukawa 2021) and the fingering phenomenon described in Section 3.2.3.

3.3.4 Surge front shape and surge front slope

Several analytical studies on impact pressure (Cumberbatch 1960, Cross, 1967, Shu, 2004) have suggested that the shape of the surge front, especially the surge front slope,

could influence the impact pressure. Therefore, I study the surge front slope and, in a later section, confirm how the surge geometry affects an actual impingement event. However, due to the complexity of the surge tip, I could not exactly define the water surface in the region very close to the contact line between the surge and dry bed. The surge shape demonstrated in this section is confined to the region wherein the water surface could be clearly defined (Figure 3.5 shows this circumstance. Kihara et al., 2015 used a similar method to measure the surge front shape). Figure 3.11 and 3.12 present the time history curves of the water surface elevation above the flume bed 10 cm away from the panel. The curves end after 0.1 s from the arrival of the surge front so that they do not include the affection from the panel.

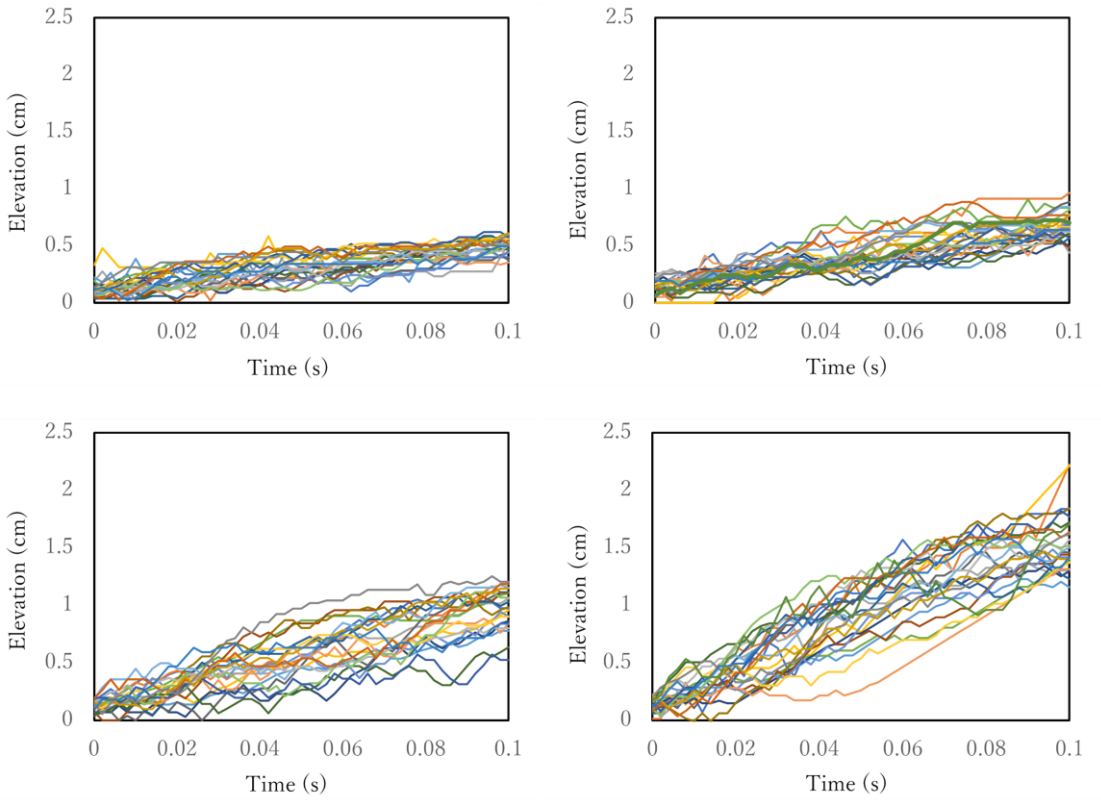

Fig. 3.11 Time history of water surface elevation 10 cm away from the panel after the arrival of the surge front with H = 8 cm (top left), H = 10 cm (top right), H = 12 cm (bottom left) and H = 14 cm (bottom right).

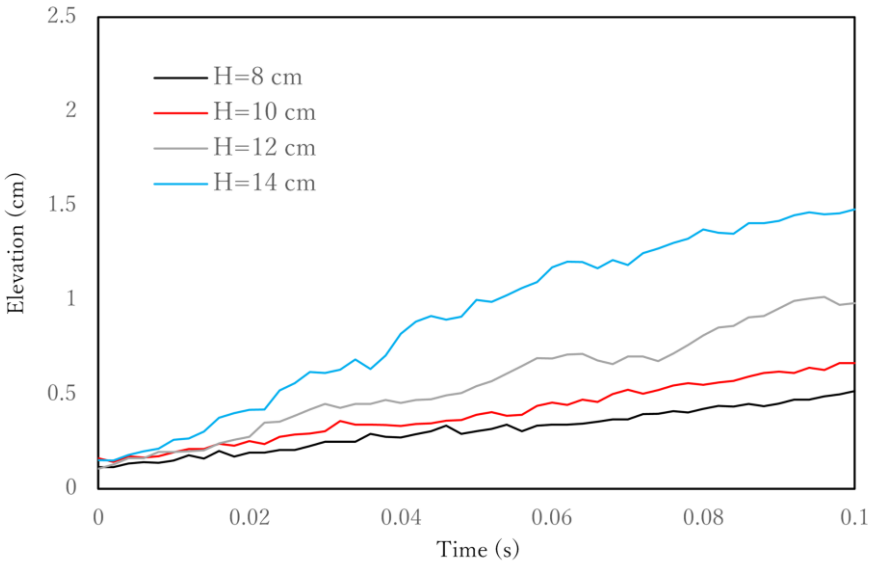

Fig. 3.12 Time history of water surface elevation 10 cm away from the panel after the arrival of the surge front with H = 8, 10, 12 and 14 cm (median curves).

The time origin (t = 0 s) in these figures is set as the moment the water surface becomes definable, which is 0.002 s after the arrival of the surge here. Therefore, they demonstrate the abrupt change in the elevation of the water surface at t = 0 s. This fact suggests that the actual surge flows could not be perfectly described as the moving water wedge used by Cumberbatch (1960). The figures demonstrate that the water surface rises more rapidly in the case with a higher initial water level, primarily due to the increase in the surge front velocity as well as the difference in the surge front shape.

The surge front slope could be calculated using the surge front velocity (presented in Section 3.3.3) and the time history of the water surface elevation (Figure 3.11) for each run as follows:

$$\tan\theta = \frac{h_{0.02}}{0.02U} \tag{3.2}$$

where tanθ is the surge front slope (averaged over 0.02 s), $h_{0.02}$ is the water surface elevation at t=0.02 s in Figure 3.11, and the values of U have been shown in Figure 3.10. Figure 3.13 presents the cumulative percentile ranking graph of the surge front slope of each run over 0.02 s, within which the impact pressure occurs after the arrival of the surge front.

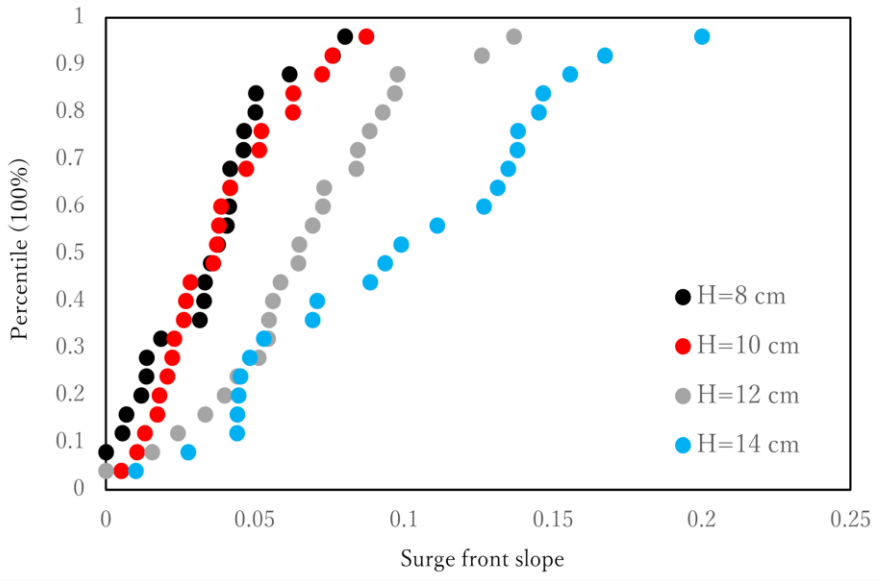

Fig. 3.13 Cumulative percentile ranking graph of the average surge front slope within 0.02 s after the arrival of the surge front in different cases.

Figure 3.13 demonstrates that a steeper surge front slope occurs with a higher initial water level. The plots are widely distributed in each case, implying that the surge front slope is a highly stochastic physical parameter in contrast to the surge front velocity. The reason for the stochasticity could be considered as the complex turbulence at the tip of the surge front. The fingering patterns described in Section 3.2.3 could also have had slight effects on the shape of the tip (see Thoroddson and Sakakibara 1998). The influence of the surge front slope on the impact pressure will be discussed in a later section.

3.4 Stochastic model for the impact pressure and discussions on the effect of surge front slope

3.4.1 Stochastic model for impact pressure

This section proposes a predictive stochastic model for the calculation of the impact pressure given the incident surge velocity. With regard to the relationship between the surge pressure and velocity, the following dimensionless parameter has to be investigated:

$$C_p = \frac{p_i}{\rho U^2} \tag{3.3}$$

where p_i (i = 0,1) is the impact pressure at P0 and P1, U is the surge front velocity in the present study, ρ is the density of water, and C_p is hereafter referred to as the impact coefficient. The value of C_p has been studied using analytical (Cumberbatch 1960) and semi-analytical methods (Kihara et al., 2015, Kihara and Kaida, 2016) and quantified empirically in several guidebooks (e.g., ASCE 2017 and FEMA 2019). However, these previous works treated the value of C_p in a deterministic manner, and its stochastic properties have rarely been studied in the literature to the best of my knowledge. Figure 3.14 presents the cumulative percentile ranking graphs of the value of C_p in each case.

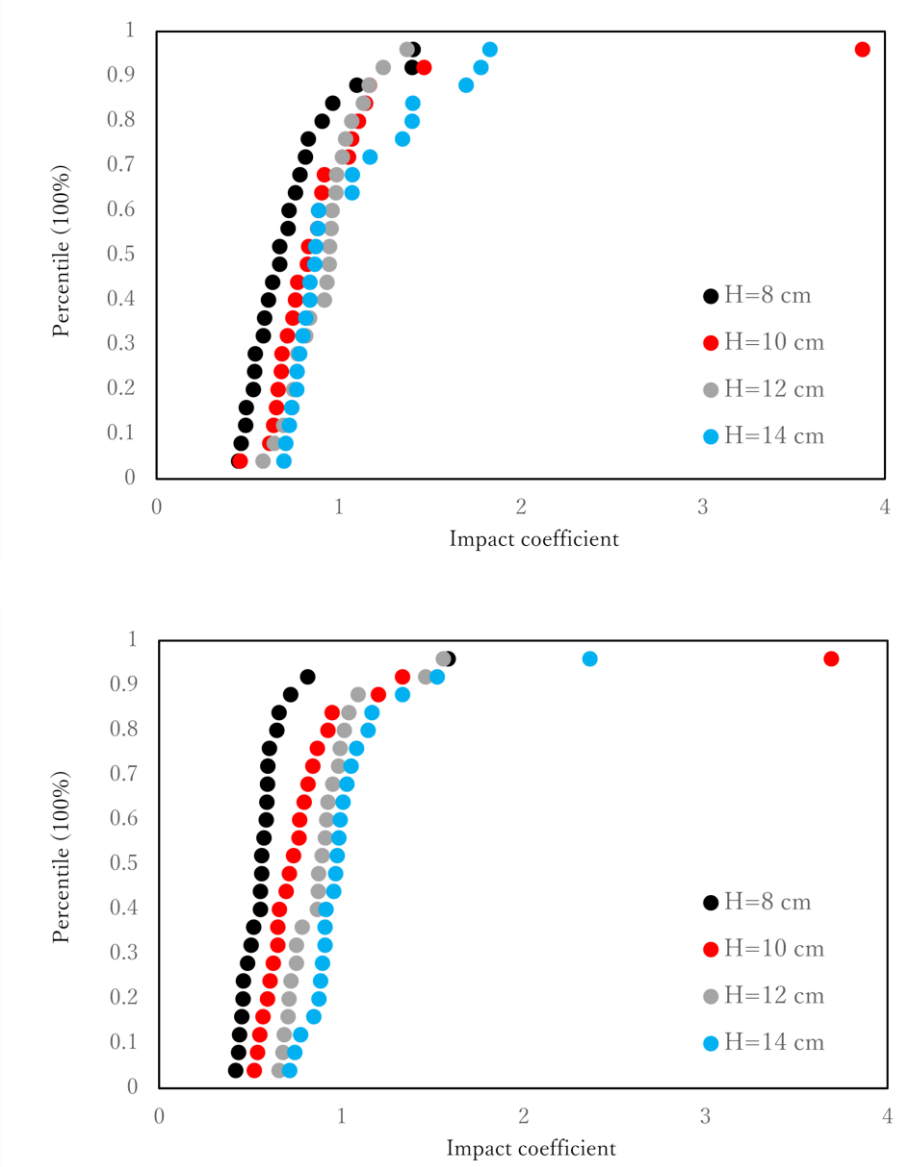

Fig. 3.14 Cumulative percentile ranking graphs for impact coefficient *Cp* in different cases at P0 (top) and P1 (bottom).

Since C_p is a function of the pressure, it also holds a fat tail as shown in Figure 3.14. Notably, the plots from different cases agree with each other slightly better in the graph of P0 than those of P1. There are two possible reasons for this tendency. Firstly, the recorded pressure is the averaged pressure over the area of the pressure sensors.

According to the surge depth shown in Figure 3.12, only the lower part of P1 receives direct impact of the surge when the value of H is small. Meanwhile, the upper part recorded the pressure generated by the run-up water. Therefore, the records of P1 might be lower than the actual impact pressure under this condition. Secondly, the surge front slope might affect the value of impact pressure at P1. This issue will be discussed in a later section. However, in this section, I attempt to propose a single-variable distribution model for C_p. Although the initial water levels of each case are different, the impact pressure has to be determined only by the physical parameters right before the impact.

The next step is to determine a stochastic distribution that could simultaneously provide a good likelihood and avoid conflicting with the physics. Since the value of C_p has to be greater than zero, the Fréchet distribution (also called type II extreme value distribution or the inverse Weibull distribution) is a reasonable choice to fit the 'fat-tailed' data here. It should be noted that several other similar distributions, e.g., the Gumbel distribution, fail to meet the lower limit of C_p. The non-exceedance probability distribution function (which is equivalent to the cumulative distribution function) and probability density function of the Fréchet distribution are

$$P_C\left(0 \le C_p{}' \le C_p\right) = \exp\left[-\left(\frac{C_p}{s}\right)^{-\sigma}\right] \tag{3.4.1}$$

$$P_D\left(0 \le C_p{}' \le C_p\right) = \frac{\sigma}{s}\left(\frac{C_p}{s}\right)^{-1-\sigma} \exp\left[-\left(\frac{C_p}{s}\right)^{-\sigma}\right] \tag{3.4.2}$$

where P_c is the non-exceedance probability distribution function, P_D is the probability density, and s and σ are the scale and shape parameters, respectively, to be determined from the laboratory data. $C_p{}'$ is a non-negative random variable.

Figure 3.15 presents the fitting curves of C_p based on Equation (3.4.1) for P0 and P1. The relationship between $\ln(C_p)$ and $\ln[\ln(P_c^{-1})]$ proves that the fitting curves have good likelihood for both P0 and P1. Table 3.1 presents several important statistical parameters of the fitting curves.

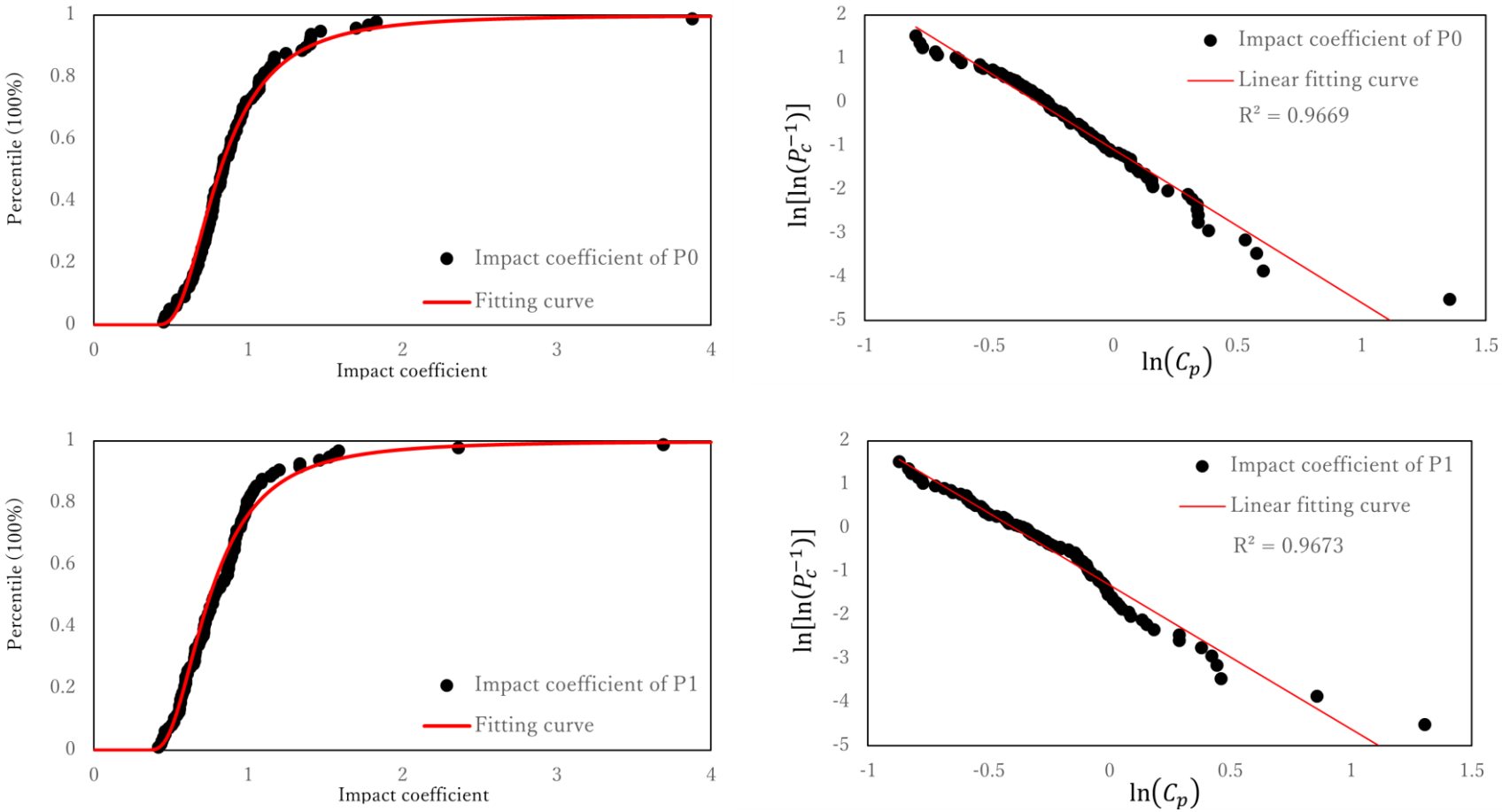

Fig. 3.15 Fitting curves based on the Fréchet distribution for P0 with (σ, s) = (3.52, 0.737) (top left, top right) and P1 with (σ, s) = (3.31, 0.674) (bottom left, bottom right)

Table 3.1 Parameters of the proposed probability distributions (fitting curves)

Parameters	P0	P1
σ	3.52	3.31
s	0.737	0.674
Mode ($s\left[\sigma/(1+\sigma)\right]^{1/\sigma}$)	0.687	0.622
5 % quantile	0.540	0.485
First quartile ($s/(\ln 4)^{1/\sigma}$)	0.672	0.610
Median ($s/(\ln 2)^{1/\sigma}$)	0.818	0.753
Third quartile ($s/\left[\ln(4/3)\right]^{1/\sigma}$)	1.05	0.982
95 % quantile	1.74	1.66

It is found that both the mode and median of P1 are smaller than those of P0 (although the differences are both under 10%). As presented in Figure 3.11 and 3.12, there is a possibility that P1 could not receive a full impact owing to its location in the case of a small H, whereas P0 is more likely to receive the full impact. This may be why the statistical parameters listed in Table 3.1 generally had smaller values at P1, and therefore, (s, σ) of P0 may have been more representative in terms of impingement physics. To justify the applicability of Equation (3.4.1) with (s, σ) listed in Table 3.1, I compare it with the published data obtained by Wemmenhove et al. (2010), Al-Faesly et al. (2012), Douglas and Nistor (2014), Kihara et al. (2015), Mizutani et al. (2017), Kihara and Kaida (2019), Shen et al. (2020), Chuang et al. (2020) and Xu et al. (2021). Both the impact pressure and surge front velocity were provided in these studies. Figure 3.16 presents the result of the comparison.

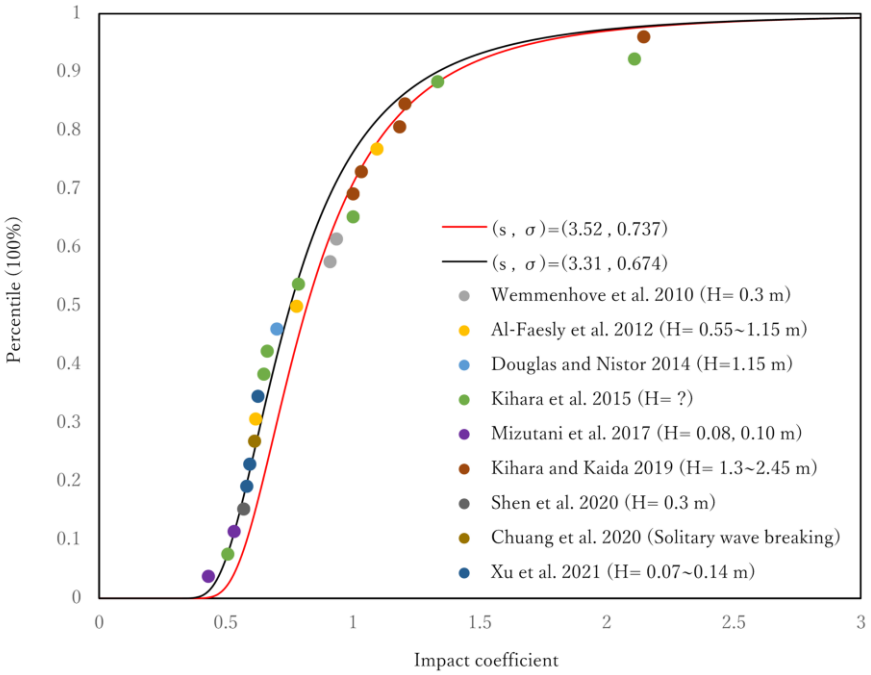

Fig. 3.16 Comparison between Equation (3.4.1) with (s, σ) = (3.52, 0.737) and (3.31, 0.674) and published data.

Equation (3.4.1) demonstrates good performance when predicting the cumulative distribution of the published data randomly collected from various literature works. Except for Chuang et al. (2020), who used the representative C_p from multiple runs, other authors provided the data from single measurement.

Equation (3.4.1) provides a way to predict the stochastic distribution of the impact pressure using only the surge front velocity right before the impact. In other words, the physical parameters specifically related to the dam-break experiments (such as the initial water level and gate speed) are excluded from the model. This is convenient for certain engineering practices (e.g., real tsunami surge impingement). Consequently, based on

Equation (3.4.1), especially with (s, σ) = (3.52, 0.737), engineers could propose engineering formulas for any quantile case by case. For example, the 50 % and 95 % quantiles read:

$$C_{p,50\%} = 0.818 \tag{3.5}$$

$$C_{p,95\%} = 1.74 \tag{3.6}$$

The comparisons between these two formulas and the formulas proposed in literature will be provided in Chapter 4 (Figure 4.8 and 4.9). Similar formulas are widely used in civil engineering (e.g., Kitahara and Ishihara 2020).

3.4.2 Relationship between C_p and surge front slope

Equation (3.4.1) and (3.4.2) suggest that the surge front velocity is the dominant factor for the impact pressure at P0 and P1. However, as introduced, a classic theoretical solution proposed by Cumberbatch (1960) indicated that the surge front slope could influence the value of C_p (also see Faltinsen 2006). Further discussions on this theory are carried out in Chapter 4. In this section, I investigate the effect of the surge front slope on C_p.

Figure 3.17 presents the relationship between C_p and the surge front slope $\tan\theta$ in each case, combined with the theoretical solution proposed by Cumberbatch (1960).

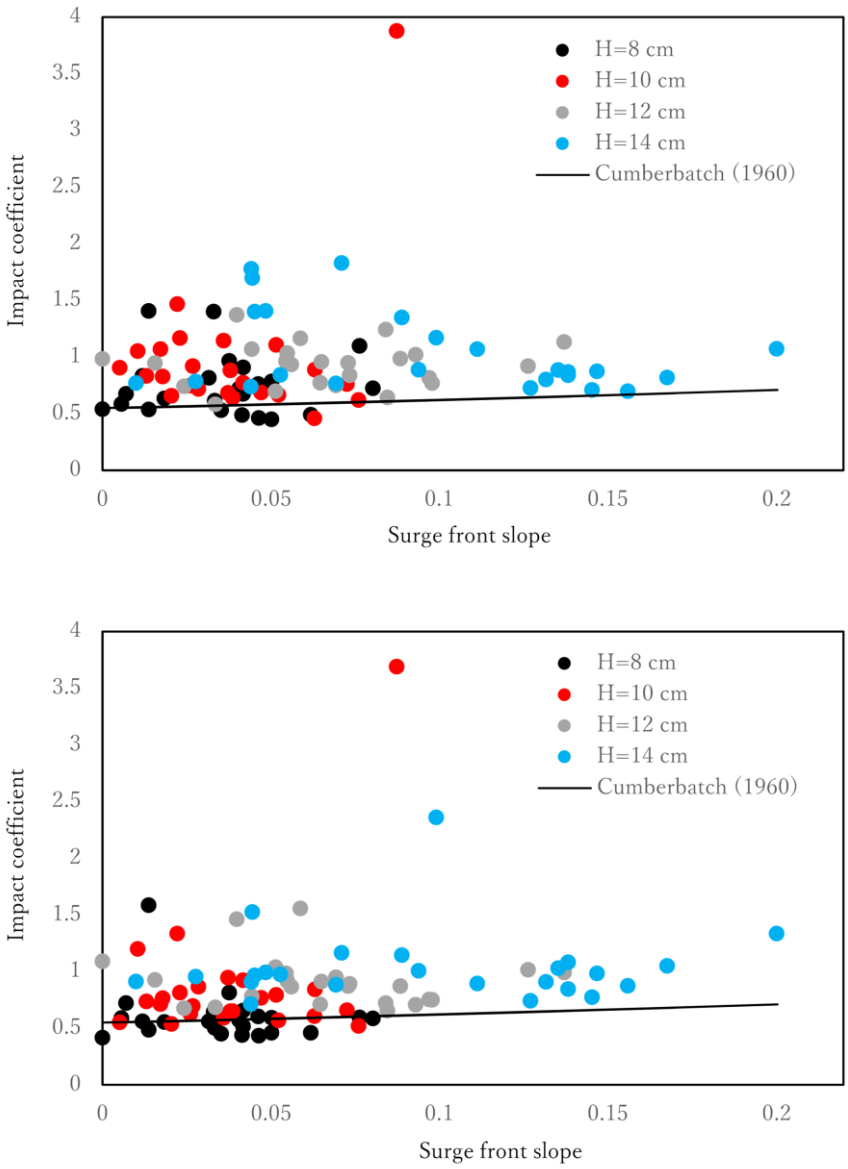

Fig. 3.17 Relationship between the surge front slope and impact coefficient in different cases at P0 (top) and P1 (bottom), combined with the theory proposed by Cumberbatch (1960).

The theory suggests that the value of C_p should slightly increase with tanθ. This tendency could be confirmed in the graph of P1 but not in the graph of P0. Besides, as seen in

Figure 3.13, the values of tanθ increased with H. This may have been one of the reasons why the plots of P0 in Figure 3.14 agreed each other better compared with those of P1 under different values of H. Figure 3.17 implies that the theory proposed by Cumberbatch (1960) could predict the increasing tendency of C_p with tanθ above the bottom but needs to be improved at the bottom. A possible reason is that actual surges were not as simple as the water wedge assumed by Cumberbatch (1960). As explained in Section 3.4 (also refer to Dressler 1952, 1954), the water surface elevation abruptly changed at the tip of the surge front, and therefore, the theory could not exactly predict the impact pressure of such surges at the bottom. However, the water surface elevation at the tip becomes trivial at P1, which is above the bottom. Thus, the theory is valid in predicting the tendency of the pressure there. Quantitatively, the theory generally underestimated the value of C_p within the range of data. This comparison shows that Cumberbatch (1960) might not elucidate the physics of surge impact in a reasonable way. This issue will be discussed in detail in Chapter 4.

Finally, although some theoretical works (e.g., Dressler 1952, Chanson 2009 and Deng et al., 2018) have demonstrated that the water surface shape at the surge front is determined by the surge front velocity, I did not obtain a good correlation between them using the data collected in the present study (see Figure 3.18). This may explain the low correlation between C_p and the surge front slope and further stochastic studies have to be carried out as future works.

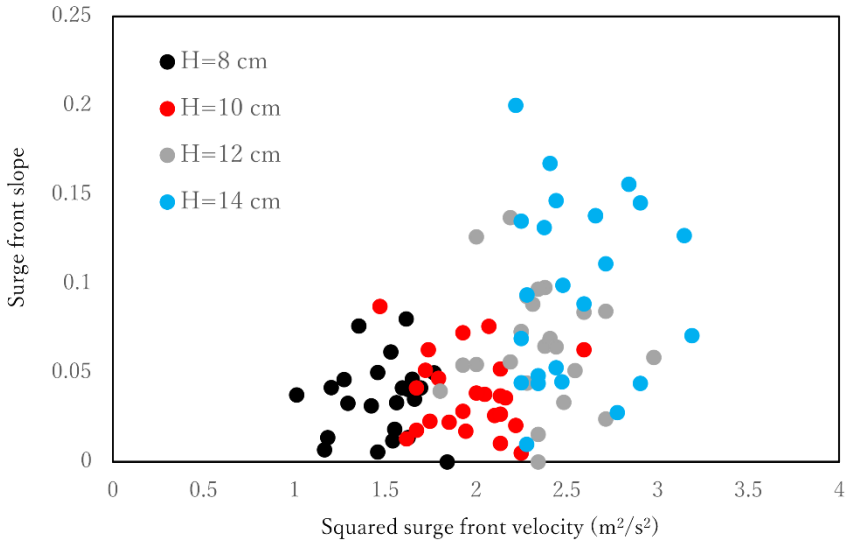

Fig. 3.18 Relationship between the squared surge front velocity and surge front slope in different cases.

3.5 Findings and motivations of further investigations

In this chapter, laboratory experiments and a stochastic analysis were conducted to evaluate the impact pressure generated by water surge impingement onto a vertical wall. Several findings could be derived from the analysis of the experimental data:

1. The time history of the pressure on the vertical wall confirmed that the impact pressure produces the largest pressure peak during the whole impingement process. The impact pressure was distributed over a wide range, and therefore, stochastic estimation is necessary indeed.

2. The impact coefficient $C_p = p/\rho U^2$ could be reasonably modeled by the Fréchet distribution, suggesting that it is more likely to have an extremely large C_p rather than an extremely small one. A predictive formula (Equation [3.4.1]) was proposed for the

stochastic distribution of C_p, which involves only the surge front velocity right before the impact. Examples of engineering formulas were given by Equation (3.5) and (3.6).

3. The surge front slope does not significantly influence the impact pressure at the bed but affects the impact pressure slightly above the bed. The theory proposed by Cumberbatch (1960) failed to predict the tendency of the impact pressure at the bed and generally underestimated the magnitude of the impact pressure (the theoretical value is smaller than the first quartile presented in Table 3.1). Therefore, based on the present study, it could be said that an improved theory should be proposed to describe the impact pressure better.

As mentioned in finding 3, it becomes necessary for me to seek an improved theory over Cumberbatch (1960) to interpret the underlying physics of surge impact. At least, the resulting analytic solution should be able to elucidate the velocity field and the impact pressure near the toe of the vertical wall, as the largest pressure peak occurs there. In Chapter 4, I will attempt to propose such an analytic solution under a well-posed physical model with detailed mathematical derivations. Also, in the laboratory works, the effects of energy dissipation on the surge front (which might be also influential to the impact pressure) was not elucidated in detail. This issue will be addressed by numerical calculations in Chapter 5.

Chapter 4

Analytic solution of the impact pressure

4.1 Introduction

This chapter proposes an analytic solution for the velocity and pressure field during a surge impingement event.

As introduced, many authors have attempted to describe the physics of surge impact by various analytic approaches. In most cases (if not all cases), the direct solutions on the velocity field are derived based on the velocity potential theory, without verifying its existence; the incident surges are also given in simple geometries. Besides, the mathematical formulations in these works are complicated and, at times, not explicit enough for readers to indicate simple relationships between the physical parameters.

The main reason for this awkward situation is that these authors aimed to obtain a comprehensive solution for the velocity field in the entire fluid region. Due to the existence of free water surface and the non-periodic nature of the surge impact, the velocity potential theory became the primary method to simplify the governing equation (the Euler's equation in most cases). In the present study, I convert the way of thinking: focusing on a specific part of the fluid region and simplifying the governing equation by a more reasonable method other than the velocity potential theory. It has been shown in many works of literature and a previous chapter of this thesis that the region near the

corner where the wall and the bed meet is crucial, as the largest impact pressure occurs there. Therefore, in this chapter, the velocity and pressure field in the vicinity of this corner will be mainly discussed without assuming the existence of velocity potential, but with a more natural simplification.

Section 4.2 proposes an initial-boundary value problem for a well-posed physical model of the surge impact. A simplified form of the inviscid vorticity transport equation (or the Euler's equation) is used as the governing equation near the bed, and the boundary conditions of the velocity field are clearly assigned on a moving boundary. The initial condition reasonably demonstrates the discontinuous nature of the impact process. In Section 4.3, this initial-boundary value problem is solved with the self-similarity method. The approximate solutions for horizontal and vertical velocity components are explicitly obtained with very high precision. The solutions could satisfy the initial condition naturally, as well. In Section 4.4, the pressure field is obtained following the solution of the velocity field. The impact pressure near the bed is shown to be finite and proportional to the square of surge front velocity with a constant impact coefficient. In Section 4.5, the solution of impact pressure is compared with the theoretical result of Cumberbatch (1960) and the formulas suggested by FEMA (2019) and ASCE (2017). The comparisons clearly demonstrate their performances when predicting the laboratory data obtained in Chapter 3. Section 4.6 briefly discusses the effect of viscosity during the impact process, intuitively proving that the Euler's equation is a proper governing equation in the present study.

4.2 Initial-boundary value problem

The two-dimensional water surge impingement onto a vertical wall is illustrated in Figure 4.1 with x and y coordinates in the horizontal and vertical directions, respectively, and with the origin at the toe of the wall. The tip of the surge approaches the wall in the negative x-direction with a uniform constant celerity $U<0$. Here, I set the time coordinate so that the surge front reaches the wall at $t=0$, and then runs up for $t>0$. The horizontal and vertical components of the flow velocity during the impingement process are denoted by u (x, y, t) and v (x, y, t), respectively, and the water pressure is represented by p (x, y, t). g is the gravitational acceleration.

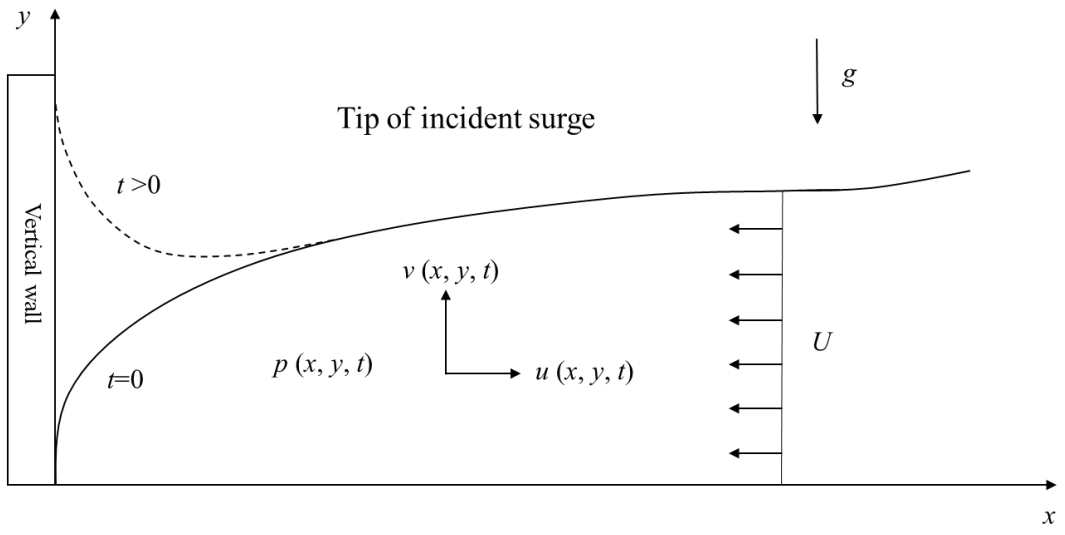

Fig. 4.1 Conceptional sketch of water surge impingement onto a vertical wall.

For simplicity, I assume that, inside the tip of the incident surge, water particles retain the uniform horizontal velocity component equals to the surge front velocity, U, and the vertical velocity component is zero almost everywhere when $t=0$. Therefore, the presence

of turbulent water layers near the bed and water surface are neglected. The initial condition is then represented by

$$u=\begin{cases}0 & x=0\\ U & x>0\end{cases} \quad \text{for } y\geq 0, t=0 \qquad \text{and} \qquad v=0 \ \text{ for } \ x>0,\ y\geq 0,\ t=0. \tag{4.1}$$

Equation (4.1) shows that u (x, y, t) has an abrupt change at the wall when t=0, reflecting the discontinuous nature of the surge impact. A typical initial condition that was used in many analytical works is

$$u=U,\ v=0 \ \text{ for } \ x\geq 0,\ y\geq 0,\ t=0 \tag{4.2}$$

As the discontinuity in the velocity field is not involved explicitly, Equation (4.2) is indeed a simpler initial condition compared with Equation (4.1). However, it brings a remarkable misunderstanding on the flow status, which will be discussed later. Since the surge impingement is a highly transient process over a short time, the viscous force is negligible compared with the inertial force (briefly discussed in Section 4.6). Therefore, the subsequent flow (t > 0) can be described by the two-dimensional Euler's equations:

$$\frac{\partial u}{\partial x}+\frac{\partial v}{\partial y}=0, \tag{4.3}$$

$$\frac{\partial u}{\partial t}+u\frac{\partial u}{\partial x}+v\frac{\partial u}{\partial y}=-\frac{1}{\rho}\frac{\partial p}{\partial x}, \tag{4.4}$$

$$\frac{\partial v}{\partial t}+u\frac{\partial v}{\partial x}+v\frac{\partial v}{\partial y}=-\frac{1}{\rho}\frac{\partial p}{\partial y}-g, \tag{4.5}$$

The solutions for the velocity components and the pressure filed could be uniquely determined under appropriate boundary conditions, but I need to simplify the governing equations in advance for an analytic approach.

First, Equation (4.3) and (4.4) can be combined into the so-called vorticity transport equation, for $t>0$:

$$\frac{\partial \omega}{\partial t} + u\frac{\partial \omega}{\partial x} + v\frac{\partial \omega}{\partial y} = 0 \quad \text{with} \quad \omega = \frac{\partial u}{\partial y} - \frac{\partial v}{\partial x}, \tag{4.6}$$

where ω represents the vorticity. Here, the initial condition of Equation (4.6) has to be analysed carefully. If the incident surge has no vorticity at the first contact, then Equation (4.6) suggests that vorticity will be kept to zero for any $t>0$, which also implies the existence of velocity potential. Therefore, based on Equation (4.2), many previous studies assumed the irrotationality for $t>0$ and introduced the velocity potential to simplify the governing equations.

However, this assumption appears not to be valid considering the nature of the subsequent up-rushing flow under the impact condition described by Equation (4.1). Obviously, the up-rushing flow (above the bed, $y>0$) has a higher vertical velocity near the wall due to the discontinuity at $t = 0$, and thus, $\frac{\partial v}{\partial x}$ has a very large negative value in the vicinity of the wall. On the other hand, the horizontal velocity is forced to be uniform along the wall ($u = 0$) and in the fluid region far from the wall ($u = U$). Thus, $\frac{\partial u}{\partial y}$ is relatively small near the wall. Therefore, I assume that the following relation holds near the wall immediately after the impingement for any small $y>0$:

$$\left|\frac{\partial v}{\partial x}\right| > \left|\frac{\partial u}{\partial y}\right| \qquad \text{and} \qquad |\omega| = \left|\frac{\partial u}{\partial y} - \frac{\partial v}{\partial x}\right| > 0 \tag{4.7}$$

Equation (4.7) suggests that an abrupt transition from the irrotational to rotational flow occurs during the surge impingement by an impulsive external force at $t = 0$. Therefore, for small $y>0$, velocity potential could not be used in the present impact model.

Furthermore, the fluid motion near the bed is now considered. When y is small, the affection of the water surface on the velocity field is considered trivial. Therefore, based on the so-called "squeeze theorem" (u is squeezed by the vertical and the uniform incident flow), it could be said that,

$$\left|\frac{\partial u}{\partial y}\right| \approx 0 \tag{4.8}$$

near the bed. Based on Equation (4.8), I here choose to simplify Equation (4.6) by neglecting $\frac{\partial u}{\partial y}$ from it (neglecting $\frac{\partial v}{\partial x}$ results in a trivial solution), arriving at

$$\frac{\partial^2 v}{\partial x \partial t} + u\frac{\partial^2 v}{\partial x^2} + v\frac{\partial^2 v}{\partial x \partial y} \approx 0 \tag{4.9}$$

Additionally, since the horizontal velocity component has been assumed to be vertically uniform near the bed, it could be denoted as $u = u(x, t)$. Consequently, Equation (4.3) could be integrated from the bed to an arbitrary small y as

$$v(x, y, t) \approx -y\frac{\partial u(x,t)}{\partial x} \tag{4.10}$$

Substituting Equation (4.10) into (4.9), we obtain a partial differential equation in terms of only $u(x, t)$:

$$\frac{\partial^3 u}{\partial t \partial x^2} + u\frac{\partial^3 u}{\partial x^3} - \frac{\partial u}{\partial x}\frac{\partial^2 u}{\partial x^2} \approx 0 \tag{4.11}$$

Here, the trivial solution y=0 has been abandoned as our discussion is confined to the region near the bed, but not precisely on the bed. Hereafter, I assume that Equation (4.11) exactly holds near the bed and derive the velocity field under the initial condition (Equation [4.1]) and appropriate boundary conditions. On the other hand, note that the equation for the pressure is now $p_{xy} = 0$ and it will be mentioned in a later section.

In order to solve this third-order differential equation, at least three boundary conditions are required. As the most straightforward boundary condition,

$$u(0,t)=0 \tag{4.12}$$

has to be satisfied on the wall. In contrast, the boundary conditions apart from the wall become more perplexing. Due to the existence of free water surface, the influence of the wall will not propagate upstream at infinite speed (or, at least, much slower than the speed of sound in water). Therefore, the fluid motion far from the wall should not be disturbed by the impingement event for small t. In other words, there exists a moving boundary $l(t)$ dividing the water into an impact region and an undisturbed region such that

$$u(x,t)=U \quad , \quad x \geq l(t) \tag{4.13}$$

$$v(x,y,t) \propto -\frac{\partial u}{\partial x}(x,t)=0 \quad , \quad x \geq l(t) \tag{4.14}$$

Figure 4.2 illustrates the moving boundary and the two regions. In the undisturbed region ($x > l(t)$), water particles hold the constant horizontal velocity component $u(x, t)=U$ and vertical velocity component $v(x, y, t)=0$. In the impact region ($0 < x < l(t)$), the velocity field varies under the influence of the wall. Therefore, considering the continuity of $u(x, t)$ and $v(x, y, t)$, Equation (4.13) and (4.14) have to be satisfied on the moving boundary $l(t)$. On the other hand, $l(t)$ travels against the incident flow direction, expanding the impact region into upstream. Therefore, in the present study, although the main target is to solve the velocity field in the impact region, the location of the moving boundary $l(t)$ also has to be determined simultaneously as an additional unknown. I have to remark here that Equation (4.14) is only a simplified form for the boundary conditions at $l(t)$.

Rigorously, the higher-order x-derivatives and t-derivatives of u (x, t) also have to be zero on this boundary. In that case, the system will become overdetermined. The consequences of conducting this simplification to the boundary conditions will be mentioned in a later section.

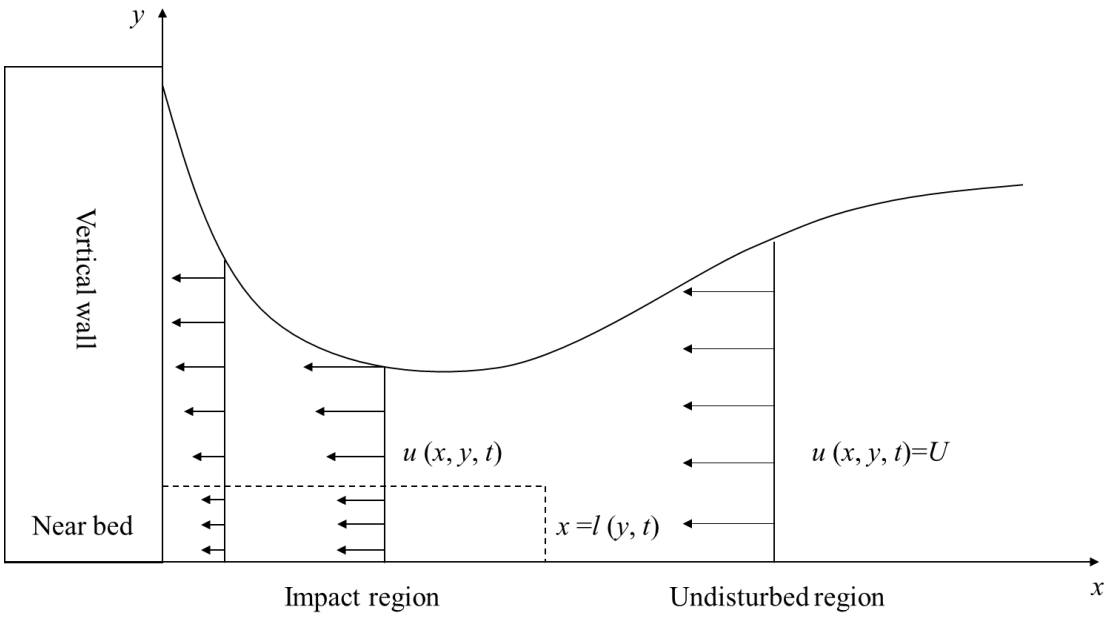

Fig. 4.2 Conceptional sketch interpreting the moving boundary conditions.

Up to here, an initial-boundary value problem for the horizontal velocity component, u (x, t), in the impact region has been constructed. The governing equation is Equation (4.11), and the boundary conditions are Equation (4.12) - (4.14). The initial condition is Equation (4.1). This moving boundary problem is an analogous problem to the notorious Stefan problem (Mei 1994, pp 343 - 407, also see Appendix A) in the field of applied mathematics. However, compared with the classic Stefan problem, Equation (4.11) is strongly nonlinear and there is no small parameter could be used to apply perturbation expansion. This awkward situation is dealt in Section 4.3.

One of the advantages of the present system is that the shape of free water surface is not involved in the problem. In the previous studies with the irrotational flow assumption, the free-surface boundary could not be avoided as the elliptic differential equation of the velocity potential had to be solved for the entire fluid region. Although l (t) is also a moving boundary here, it is a single-variable function of t with its initial value being simply zero. Therefore, compared with the complex free water surface (which could be in a complicated shape from the beginning), the moving boundary proposed here is obviously easier to handle in this sense. In compensation, our discussion is inevitably confined to the region very close the bed as the simplification is based on $\left|\frac{\partial u}{\partial y}\right| \approx 0$. It will be shown in Chapter 5 that, in practise, the solution of the velocity field is also applicable to the water region slightly above the bed.

4.3 Self-similarity solution of velocity field

In this section, I attempt to find an analytic solution of u (x, t) in the initial-boundary value problem proposed in Section 4.2. Since there is no explicit characteristic length in the horizontal direction, I define that

$$F(X) = \frac{u}{U} \qquad X = \frac{x}{Ut} \tag{4.15}$$

as the self-similarity variables to construct a self-similarity solution for u (x, t). These variables were also used in the analytical work of Cumberbatch (1960). As I am interested in the very beginning stage of the impingement, the gravitational effect could be considered negligible (refer to Lamb 1932, Chapter I-11). Using Equation (4.15), I transform Equation (4.11) into

$$-XF''' - 2F'' + FF''' - F'F'' = 0 \tag{4.16}$$

which is a nonlinear ordinary differential equation of $F(X)$ without any scaling factor. Equation (4.12) could be immediately translated into the form of

$$F(0) = 0 \tag{4.17}$$

for $t>0$. By using Equation (4.16) and (4.17), I could also obtain that

$$F''(0) = 0 \quad \text{or} \quad F'(0) = -2 \tag{4.18}$$

Equation (4.18) will be used to verify the soundness of the self-similarity assumption in a later chapter. I only consider the velocity field within the impact region defined in the previous section in the present study. Therefore, the rest of the boundary conditions given at the moving boundary $l(t)$ are written in the self-similarity forms:

$$F\left(L\right)=1 \tag{4.19}$$

$$F'\left(L\right)=0 \tag{4.20}$$

where $L = l(t)/Ut$. Since the gravitational acceleration and the viscosity are neglected in the present discussion, it could be said that

$$l\left(t\right)\propto Ut \tag{4.21}$$

is the only possible form for $l(t)$, from the view of dimension analysis. Therefore, L should be a constant number in the present system. However, as the gravitational acceleration is negligible only for small t, Equation (4.21) is valid only when discussing the impact process.

With Equation (4.17), (4.19) and (4.20), the solution of Equation (4.16) should be uniquely determined. However, unfortunately, I am unable to find out an exact solution of Equation (4.16) by standard mathematical functions, with boundary conditions assigned on an undetermined boundary. Therefore, an approximate solution is built. The solution of Equation (4.16) is expanded into the Taylor series at X=0:

$$F\left(X\right)=\sum_{n=1}^{\infty}a_nX^n=a_1X+a_2X^2+a_3X^3+a_4X^4+\cdots \tag{4.22}$$

Note that Equation (4.17) has already been applied here ($a_0 = 0$). Similar expansions were used in Stoker (1957 [Chapter 12]) and Tao et al., (1988). If Equation (4.22) is cut off at X^q, where q is an integer greater than unity, there would be totally q+1 unknowns (a_1,…,a_q and L). The following algebraic equations could be obtained by plugging Equation (4.22) into Equation (4.16).

$$X^0: \ -4a_2 - 2a_1a_2 = 0 \tag{4.23}$$

$$X^1: \ -4a_2^2 - 18a_3 = 0 \tag{4.24}$$

$$X^2: \ -12a_2a_3 - 48a_4 - 12a_1a_4 = 0 \tag{4.25}$$

$$X^3: \ -12a_3^2 - 8a_2a_4 - 100a_5 + 40a_1a_5 = 0 \tag{4.26}$$

$$X^4: \ -30a_3a_4 + 10a_2a_5 - 180a_6 + 90a_1a_6 = 0 \tag{4.27}$$

$$X^5: \ -24a_4^2 - 24a_3a_4 + 48a_2a_5 - 294a_7 + 168a_1a_7 = 0 \tag{4.28}$$

$$X^6: \ -56a_4a_5 + 112a_2a_7 - 448a_8 + 280a_1a_8 = 0 \tag{4.29}$$

……

Only the first q-1 algebraic equations could be considered when the series in Equation (4.22) is cut off at X^q, as higher-order terms appear from the q-th equation. However, the boundary conditions at $X=L$ provide two more equations for solving the unknowns:

$$\sum_{n=1}^{q} a_n L^n = 1 \tag{4.30}$$

$$\sum_{n=1}^{q} n a_n L^{n-1} = 0 \tag{4.31}$$

As the system of q+1 equations is nonlinear, reluctantly, I have to solve it numerically in most cases, under the restrictions that the solutions must be real and satisfy $L<0$. Since Equation (4.16) is a third-order ordinary differential equation, I have to at least include the terms up to X^3 in Equation (4.22). Reasonable approximations up to X^q, denoted by $F^q(X)$, have been listed in Table 4.1 (q=3, 4, …8). These solutions are obtained using a reliable mathematical software Mathematica 12.3.

Table 4.1 Solutions of the coefficients in Equation (4.22) and the value L for $F^q(X)$

q	a_1	a_2	a_3	a_4	a_5	a_6	a_7	a_8	L
3	Real solution does not exist								
4	-2.000	-1.313	-0.3828	0.08374	-	-	-	-	-1.143
5	-2.000	-1.363	-0.4126	0.09370	0.01702	-	-	-	-1.255
6	-2.000	-1.351	-0.4054	0.09125	0.01643	0.002466	-	-	-1.213
7	-2.000	-1.352	-0.4064	0.09159	0.01651	0.002481	0.0003296	-	-1.220
8	-2.000	-1.352	-0.4062	0.09154	0.01650	0.002479	0.0003292	3.597×10^{-5}	-1.219

Table 4.1 suggests that the coefficients exhibit oscillatory convergence to certain values with increasing q. Also, as an extra restriction to the solutions, Equation (4.18) is exactly satisfied by the value of a_1 at any accuracy in Table 4.1. The reason why real solution does not exist for q=3 is not discussed in this thesis. A possible way to address this problem is to study the structure of the algebraic equations in detail. The proof that real solutions always exist for any q>3 is also not pursuit here. These issues are left for future mathematical works.

Figure 4.3 presents the approximate curves based on the coefficients listed in Table 4.1. The curves of different orders suggest quick convergence of the series, and the higher-order terms have no significant effect on the approximate solution. Figure 4.4 shows the relative differences between $F^q(X)$ and $F^{q-1}(X)$, which is defined as

$$E_1^q(X) = \frac{F^q(X) - F^{q-1}(X)}{F^{q-1}(X)} \times 100\% \tag{4.32}$$

for q= 5, 6, 7 and 8. The results confirm that the solutions have satisfactory convergence. The importance of this property will be mentioned again in a later discussion of the pressure field.

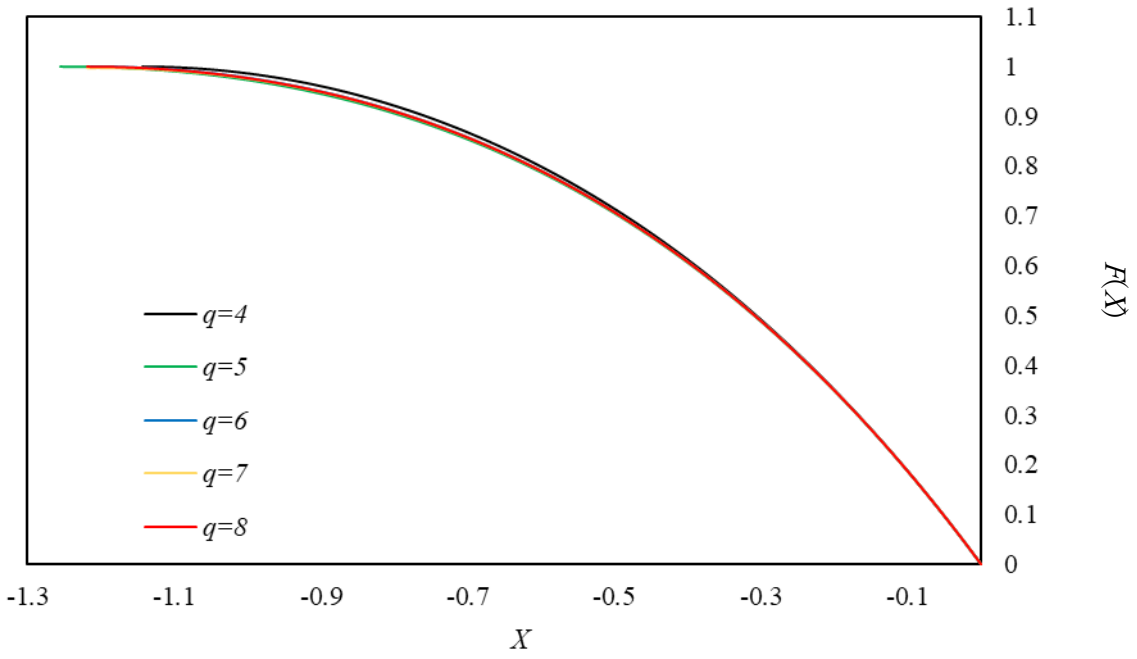

Fig. 4.3 Solutions of $F(X)$ at different accuracy

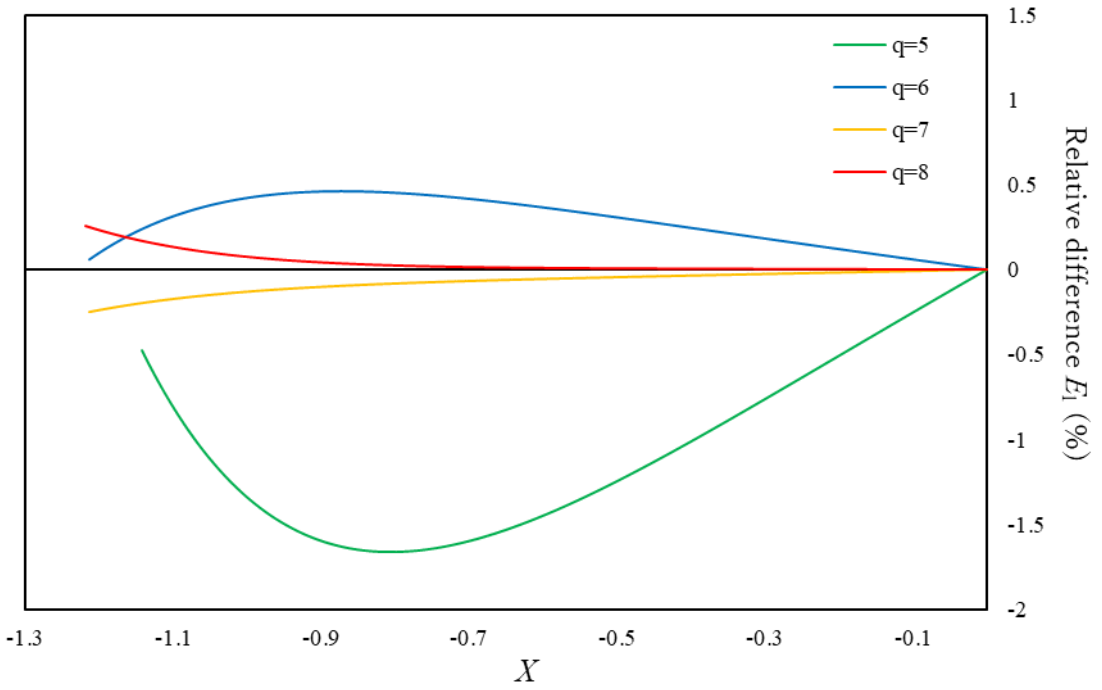

Fig. 4.4 Relative differences between $F^q(X)$ and $F^{q-1}(X)$ (q=5,6,7,8).

The vertical velocity component v (x, y, t) inside the impact region is also calculated in a self-similarity form using Equation (4.10) and the result of $F(X)$ as follows

$$G(X,Y) = -Y\left(a_1 + 2a_2X + 3a_3X^2 + 4a_4X^3 + \cdots\right) \tag{4.33}$$

where

$$G(X,Y) = \frac{v}{U} \quad , \quad Y = \frac{y}{Ut} \tag{4.34}$$

are the self-similarity variables in the vertical direction. Also, the dimensionless total velocity of the water particles could be obtained as

$$V(X,Y) = \sqrt{F^2(X) + G^2(X,Y)} \tag{4.35}$$

The distributions of $G(X, Y)$ and $V(X, Y)$ are shown in the following figures.

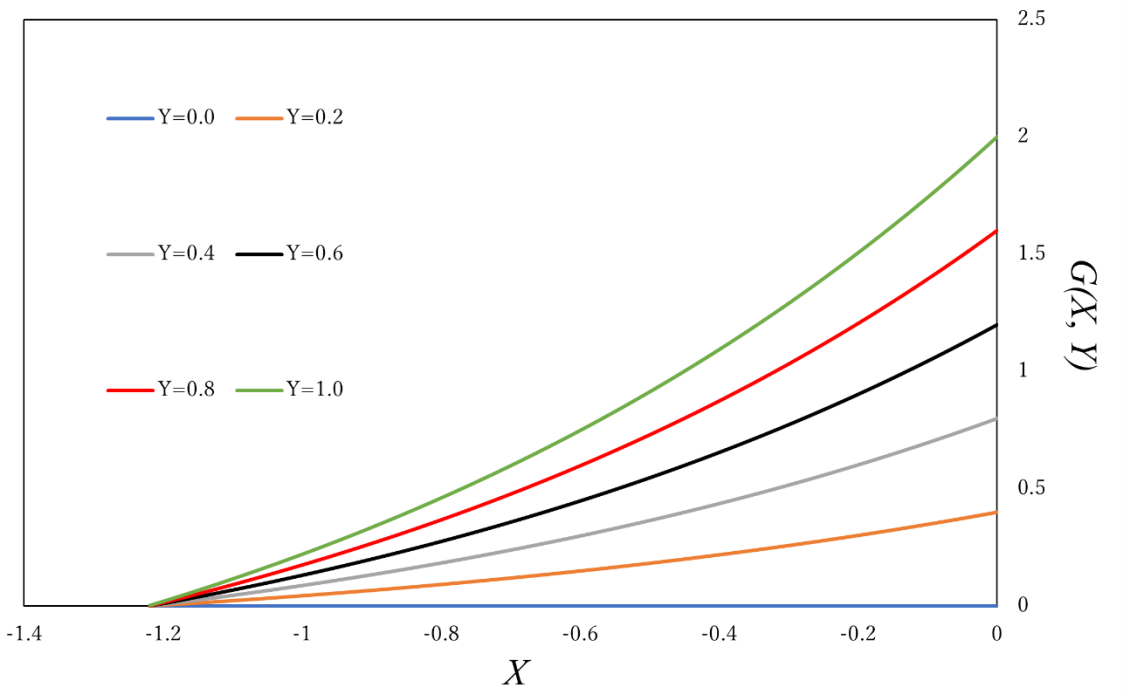

Fig. 4.5 Solutions of $G\ (X,\ Y)$

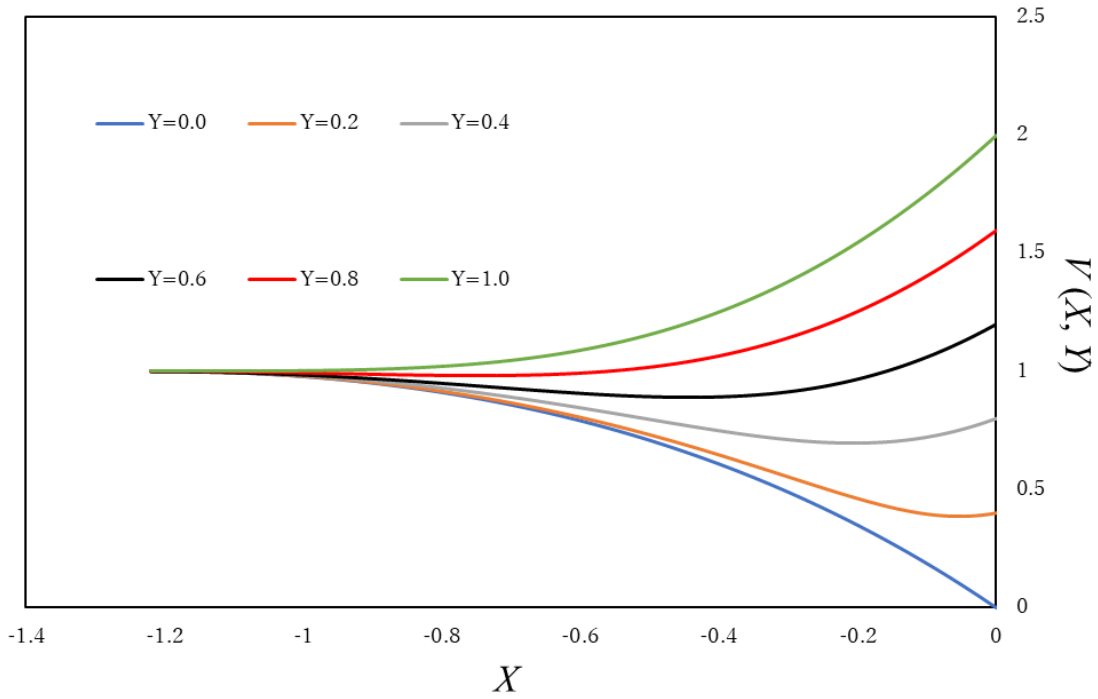

Fig. 4.6 Solutions of $V\ (X,\ Y)$

In Figure 4.5, it could be confirmed that, above the bed, the vertical velocity component of the water particles monotonically increases in the impact region, but does not diverge to infinity in the present self-similarity system of X and Y. However, Figure 4.5 also revealed an obvious weak point of this system. When $X=L$, the X-derivative of G (X, Y) is non-zero (greater than zero) for any $Y>0$. The reason is, as mentioned before, that I only considered the boundary condition for the first derivative of F (X) on L, neglecting the restrictions of higher-order derivatives. This simplification will be shown to bring more conspicuous calculation errors in a later chapter.

It could be found in Figure 4.6 that the total velocity of the water particles shows different behaviors in (L, 0) under different values of Y. For small Y, the velocity of water particles monotonically decreases when X approaches zero. For medium Y, it decreases at first and increases near the wall. For large Y, it monotonically increases with X. The reason is that the horizontal velocity component governs the velocity field very close to the bed, while the vertical velocity component comes into power for large Y instead. I, here again, emphasize that these discussions are only valid near the bed.

4.4 Self-similarity solution of pressure field

In this section, I seek a solution for the pressure field using the Euler's equation. Given the expressions of $F(X)$ and $G(X, Y)$, Equation (4.4) and (4.5) can be rewritten in terms of the self-similarity variables as

$$-\frac{\partial C_p}{\partial X} = -X\frac{dF}{dX} + F\frac{dF}{dX} \tag{4.36}$$

$$-\frac{\partial C_p}{\partial Y} = -X\frac{\partial G}{\partial X} - Y\frac{\partial G}{\partial Y} + F\frac{\partial G}{\partial X} + G\frac{\partial G}{\partial Y} + \frac{gt}{U} \tag{4.37}$$

Here, $C_p(X, Y, t)=p(X, Y, t)/\rho U^2$ is hereafter referred to as the "impact coefficient". For Equation (4.37), I replace $G(X, Y)$ by $F(X)$ using the mass conservation law, arriving at

$$-\frac{\partial C_p}{\partial Y} - \frac{gt}{U} = Y\left(XF'' + F' - FF'' + F'^2\right) = Y\Phi\left(X\right) \tag{4.38}$$

Perceptively, I noticed that

$$\Phi'\left(X\right) = XF''' + 2F'' - FF''' + F'F'' = 0 \tag{4.39}$$

according to Equation (4.16). This result suggests that the value of $\Phi(X)$ is a constant number. Therefore, if the value of $\Phi(X)$ at a specific X is figured out, the value of $\Phi(X)$ at any X could then be determined. By taking advantage of Equation (4.17) and (4.18), I can easily obtain that

$$\Phi\left(X\right) = \Phi\left(0\right) = 2 \tag{4.40}$$

Therefore, Equation (4.37) could be rewritten into

$$-\frac{\partial C_p}{\partial Y} = 2Y + \frac{gt}{U} \tag{4.41}$$

$C_p(X, Y, t)$ can be then obtained from Equation (4.36) and (4.41) as

$$C_p(X,Y,t) = -\frac{1}{2}F^2 + XF - \int_L^X F dX - Y^2 - \frac{gt}{U}Y + T(t) \tag{4.42}$$

where $T(t)$ is an unknown function of time. $T(t)$ can be determined using the dynamic boundary condition that the pressure at L is hydrostatic. For example,

$$C_p(L,0,t) = \frac{gh(t)}{U^2} = \frac{1}{Fr^2(t)} = -\frac{1}{2} + L + T(t) \tag{4.43}$$

where $h(t)$ is water depth at $X = L$ and $F_r(t)$ is the local Froude number. Based on Equation (4.43),

$$C_p(X,Y,t) = -\frac{1}{2}F^2 + XF - \int_L^X F dX - Y^2 + \frac{1}{2} - L + \frac{1}{F_r^2(t)}\left[1 - \frac{YUt}{h(t)}\right] \tag{4.44}$$

is obtained. Since the tip of the surge is highly supercritical, the hydrostatic pressure term is considered negligible in most cases of the present study (it may become significant when discussing a large-scale problem). Particularly, the impact coefficient at the toe of the wall (X=0 and Y=0^+) is given by

$$C_{pw} \equiv C_p(0,0^+,t) = \frac{1}{2} + \left(-L - \int_L^0 F dX\right) + \frac{1}{F_r^2(t)} = \frac{1}{2} + S + \frac{1}{F_r^2(t)} \tag{4.45}$$

where S is equivalent to the area shown in Figure 4.7, bounded by the vertical axis, $F(X)$ and $F(X)$=1. From Equation (4.45), we could clearly figure out three different pressure components. The constant 1/2 is equivalent to the value of C_{pw} under a steady flow condition. S is generated by the unsteady nature of impact, and this area is by no means negligible as long as $F(X)$ holds the distribution shown in Figure 4.3 and 4.7 (this issue will be discussed again in Section 4.5). The term involving the Froude number represents the hydrostatic component.

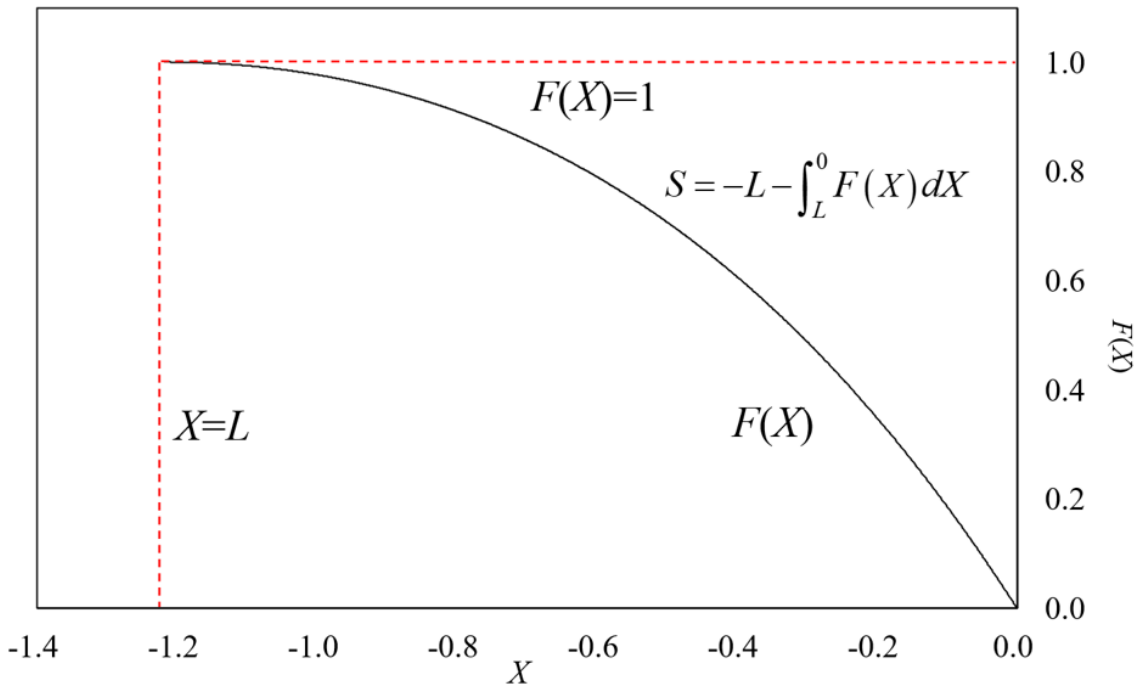

Fig. 4.7 Sketch of the definition of S

The calculation error of $F(X)$ in the range of larger X becomes more influential, considering the shape of curves in Figure 4.3. This fact was mentioned in the previous section, and the approximate solutions of $F(X)$ for q=7 and 8 have been proved to have good convergence as X approaches zero.

It is also possible to directly calculate the integral in Equation (4.45) using Equation (4.22) and the information listed in Table 4.1. Table 4.2 presents the values of C_{pw} at different accuracy, neglecting the hydrostatic pressure. E_2, the relative differences between the values of C_{pw} at two adjoint orders of accuracy, denoted by C_{pw}^{q} and C_{pw}^{q-1}, is defined as following (q=5,6,7,8), which is similar to the definition of E_1.

$$E_2 = \frac{C_{pw}^{\ q} - C_{pw}^{\ q-1}}{C_{pw}^{\ q-1}} \times 100\% \tag{4.46}$$

Table 4.2 Calculated impact coefficient at different accuracy

q	C_{pw}	E_2 (%)
4	0.8587	-
5	0.8686	1.157
6	0.8659	-0.3139
7	0.8671	0.1414
8	0.8667	-0.05040

It could be understood from Table 4.2 that the values of C_{pw} rapidly converge to a constant which is around 0.867. Therefore, in case that the hydrostatic effect is neglected, the theoretical value of $C_{p\mathrm{w}}$ at the first contact, $t=0^+$, could be approximately written as

$$C_{pw0} \equiv C_p\left(0,0^+,0^+\right) = 0.867 \tag{4.47}$$

Compared with the quantiles presented in Table 3.1, Equation (4.47) provides a theoretical value close to the median value. Besides, we could obtain an engineering formula for predicting the 95 % quantile of the impact coefficient as

$$C_{pw0,95\%} = \alpha_1\alpha_2 \qquad \alpha_1 = 2.01\ ,\ \alpha_2 = 0.867 \tag{4.48}$$

From the discussions up to here, I have found a self-similarity solution of the impact coefficient that could satisfy the Euler's equation, when $F(X)$ and $G(X, Y)$ are given. The resulting impact coefficient on the wall, C_{pw0}, converged to a finite constant value under this self-similarity system. It proved that although the velocity components could be truly singular in a surge impingement event, the singularity is removable in terms of the impact pressure.

4.5 Comparison between the analytical solution of C_{pw0} and existing studies

In this section, I directly compare the theoretical value of the impact coefficient at the toe of the wall, C_{pw0}, provided by Equation (4.47), with the existing studies. The data collected from the laboratory works which have been demonstrated in a previous chapter are used again here, with the theory proposed by Cumberbatch (1960) and the formulas suggested by FEMA (2019) and ASCE (2017).

The theory derived by Cumberbatch (1960) assumed that the flow during the impingement is irrotational, and therefore, the velocity potential was used there. The velocity field and the shape of the free water surface were calculated in self-similarity forms, and a solution of C_p on the wall (X=0) was found to be

$$C_p\left(0,Y,\theta\right)=\frac{1}{2}f\left(\theta\right)\left[1-\left(\frac{Y}{\mathrm{I}\left(\theta\right)}\right)^2\right] \tag{4.49}$$

which is called the "approximate solution". Here, θ is the surge front angle that has appeared in a previous chapter. $f(\theta)$ is a specific function of θ and its value has to be determined numerically. I (θ) is the dimensionless water surface elevation on the wall which depends on θ. Comparing Equation (4.49) with Equation (4.44), we understood that both of them suggest a parabolic decreasing tendency of C_p in terms of Y. However, the "approximate solution" involves the surge front angle, while Equation (4.44) is independent of it. The main differences between the present theory and Cumberbatch (1960) are briefly summarized in Table 4.3.

Table 4.3 Differences between the present theory and Cumberbatch (1960)

	Fluid motion	Applicability	Considered factor	Water surface
Present theory	Rotational	Near the bed	U	Not considered
Cumberbatch (1960)	Irrotational	Entire region	U, θ	Wedge

It could be understood that the advantages of the present theory over Cumberbatch (1960) are (i). the fluid motion is no more assumed irrotational, and this is consistent with the physics; (ii). the free water surface is excluded from the formulations, highly simplifying the boundary value problem. Moreover, as demonstrated in a previous chapter, in Equation (4.49), when $Y,\theta \to 0$, the value of C_p turns to 1/2 which is the value of steady flow condition. As mentioned in Section 4.4, this is an awkward conclusion as the surge impact is a highly transient phenomenon where the impact pressure should by no means be equivalent to the steady pressure. On the other hand, Equation (4.44) indicates that the unsteady effect never fades away even for very "flat" incident surges. The reason for this difference is considered to be the usage of the irrotational flow assumption.

The way of calculating the surge impact pressure suggested by FEMA (P-646, 8.6.4, Aug. 2019) is that *"The impulsive force is taken as 1.5 times the hydrodynamic force for the same element, and acts on members at the leading edge of the tsunami bore."* On the other hand, FEMA (2019) also suggests calculating the hydrodynamic force using the formula proposed by ASCE 7-16 (4.10.2.3, 2017):

$$C_p = \frac{p_i}{\rho U^2} = \gamma_1 \frac{1}{\rho U^2} \frac{F_w}{bh_s} \quad , \quad F_w = I_{tsu}\gamma_2 \left(\frac{1}{2}\rho U^2 \right) bh_s C_d \tag{4.50}$$

where

p_i : Impact pressure
F_w : Hydrodynamic force
b : Width of the vertical wall
h_s : height of the surge front
I_{tsu} : Tsunami importance factor, $=1.0$
C_d : Drag coefficient, $=2.0$ for vertical wall
γ_1 : Safety coefficient for impact pressure, =1.5
γ_2 : Safety coefficient for hydrodynamic force, =1.5

Since Equation (4.50) only gives the hydrodynamic force applied on the wall and there is no description of the pressure distribution on the wall could be found in ASCE (2017), I here simply calculate the impact coefficient as

$$C_{pw0} = \gamma_1 \gamma_2 \frac{1}{2} I_{tsu} C_d = 2.25 \tag{4.51}$$

It could be seen that the value of C_{pw0} suggested by FEMA (2019) is obviously larger than the results of Equation (4.47) and (4.49) (at least for "flat" surges). However, as a practical guideline for actual engineering works, FEMA (2019) is able to fairly describe the maximum value of the C_{pw0} of the laboratory data, given that C_{pw0} is a highly stochastic parameter.

Figure 4.8 and 4.9 show the comparisons among the laboratory data of the present study (at P0 and P1), and the results of Equation (4.47), (4.49) and (4.51). It could be confirmed that Equation (4.47) describes the median (non-exceedance probability of 50%, Equation (3.5)) of the laboratory data quite well, while the non-exceedance probability of Equation (4.49) is around 8%. Equation (4.51) succeeds in predicting the maximum value (non-exceedance probability of 95%, Equation (3.6) or Equation (4.48)) of the laboratory data, except for several extremely large plots.

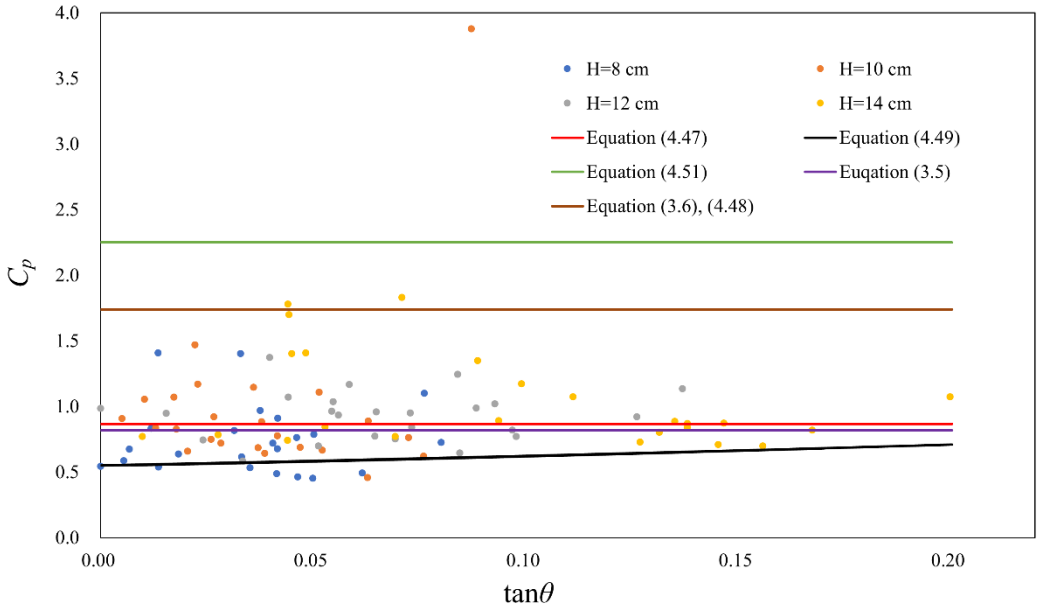

Fig. 4.8 Comparison among the laboratory data of C_{pw0} at P0, with Equation (4.47), (4.49), (4.51), (3.5) and (3.6)

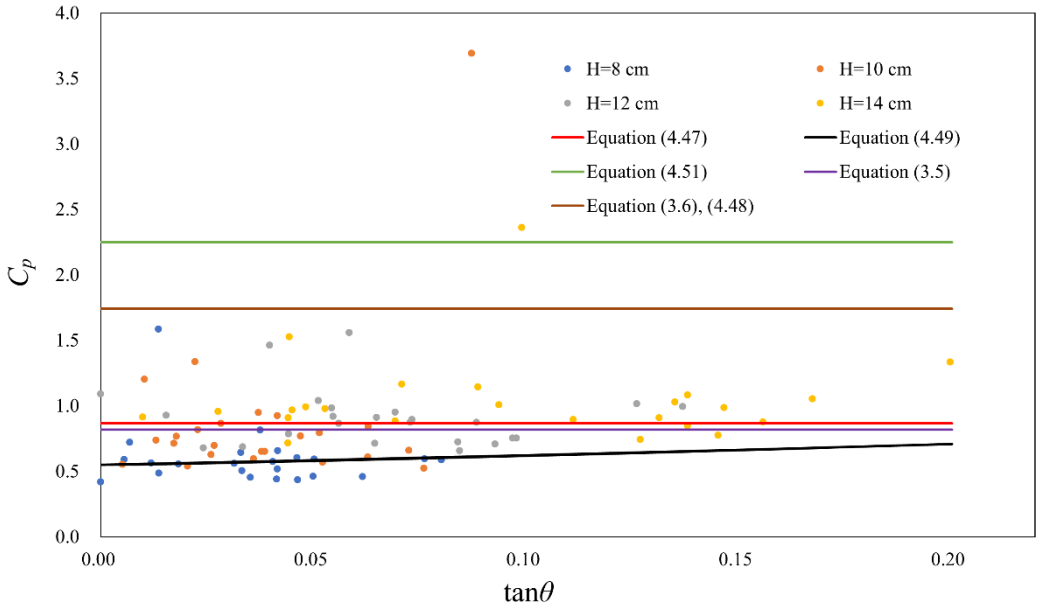

Fig. 4.9 Comparison among the laboratory data of C_{pw0} at P1, with Equation (4.47), (4.49), (4.51), (3.5) and (3.6)

Up to here, I have presented the solutions of the velocity and pressure field for the initial-boundary value problem proposed in Section 4.2. The physical assumptions made in the derivations are summarized in the following table.

Table 4.4 Assumptions used in the derivations

	Assumptions
Water	Inviscid, Incompressible, No aeration, Free from surface tension
Wall	Vertical, Rigid, Impermeable, Fixed
Bed	Horizontal, Hydraulic smooth, Impermeable
Kinematics	Uniform incident flow Water surface not influential to the bed $\partial u/\partial y=0$ Vorticity exists
Dynamics	Finite speed of pressure wave (influences of the wall) Hydrostatic outside the impact region
Mathematics	All derivatives converge (except $t=0$) Self-similarity

4.6 A brief discussion on viscosity

Although I did not involve viscosity in the analytic solution, it is meaningful to confirm the possible effect it may bring to the system. In this section, I directly use the solution of $F(X)$ and $G(X, Y)$ to investigate the viscous effect. Although it is not mathematically rigorous to apply the solutions obtained from the Euler's equation to the

discussion of viscosity, I could still obtain an intuitive qualitative evaluation of the viscous effect.

The flow above the boundary layers near the solid surfaces is considered here. The Navier-Stokes equation on the horizontal direction could be written in the self-similarity form:

$$-X\frac{dF}{dX}+F\frac{dF}{dX}+\frac{\partial C_p}{\partial X}=\frac{1}{\mathrm{Re}_0}\frac{d^2F}{dX^2} \tag{4.52}$$

where

$$\mathrm{Re}_0=\frac{U\left(Ut\right)}{\nu}=\frac{Ul}{L\nu} \tag{4.53}$$

is defined as the Reynold's number in this self-similarity system, and ν is the kinematic viscosity. As it is intentionally expressed in Equation (4.53), $l(t)$ is regarded as the representative length in this self-similarity system. $l(t)$ represents the range that the impingement event could influent, and its scale is proportional to time t. Therefore, from Equation (4.52), it could be understood that the viscosity term leads the pressure gradient to infinity when $l\left(t\right)\to 0$ but it will rapidly fade away when $l(t)$ becomes large. The kinematic viscosity is a small constant number for many fluids, including water (at the order of 10^{-6} m^2/s). Therefore, if the magnitude of U^2t is significantly larger than the order of ν, the viscous effect could be neglected. In many laboratory experiments and engineering works, the magnitude of U is usually larger than 10^0 m/s. It means that if the order of t is larger than 10^{-5} s, the value of Re_0 will become small enough to annihilate the influences from viscosity. Numbers of authors have reported that the impact pressure peak generated by a water surge usually occurs at the order of 10^{-3} s after the first contact.

Accordingly, it could be said that the impact pressure is not governed by viscosity but by the advective terms in the Euler's equation.

Here, I have to emphasize that the above discussion is barely based on the analytic solutions obtained from the simplified Euler's equation, and it is by no means a rigorous quantitative investigation on the viscous effect. However, under the assumption that $|F_{XX}| < \infty$ for any $L \le X \le 0$, it still proved that the viscosity term does not significantly affect the impact pressure.

Chapter 5
Numerical verifications

5.1 Introduction

This chapter provides us with some numerical verifications on the results obtained in Chapter 3 and 4, using a reliable CFD (Computational Fluid Dynamic) software.

In Chapter 3 and 4, I have investigated the stochastic characteristics of surge-induced impact pressure by laboratory experiments and have proposed an analytic solution for the physics of the surge impact phenomenon. However, as the surge impact is a highly transient process, a number of the results obtained from the analytic solution could not be easily verified by laboratory works, especially in the vicinity of the wall. Besides, due to this transient nature of surge impact, I was also unable to investigate the complex turbulent flows combined with the effects of viscosity in laboratory works.

The issues above-mentioned have to be handled with numerical methods. As introduced, with the increasing capability of computers, many powerful CFD tools have been developed to evaluate the fluid-induced impact pressure onto solid surfaces under various physical conditions. In this chapter, I use a reliable commercial CFD tool, Flow-3D 10.3, to investigate the velocity and pressure fields in the vicinity of the wall with a dam-break model. I rebuild the flume used in Chapter 3 with the exact same scale in Flow-3D and involve viscosity and turbulence into the calculations. With the results of the

numerical computations, I could verify the soundness of the discussions written in Chapter 3 and 4.

Section 5.2 introduces some basic information about Flow-3D. As it is a commercial software, some detailed mathematical formulations and computational codes are not open to users. However, there are still many general descriptions of the computation process provided by the producer. Section 5.3 presents the comparisons between the numerical data with the results of the velocity and pressure fields obtained from Chapter 4 in inviscid flows. The soundness of the self-similarity method is carefully verified, showing that this method could yield reasonable results which generally agree with the numerical data. Section 5.4 presents the numerical calculations where viscosity and turbulences are involved. The comparisons between inviscid and viscous flows are demonstrated, and the applicability of the theory proposed in Chapter 4 is revisited there.

5.2 General descriptions of the numerical tool

Flow-3D is known as one of the CFD models for calculating small-scaled fluid motions, and it is used in the present study to simulate dam-break flow and the impact pressure it induces on a vertical wall in a small flume. This CFD model is produced and distributed by Flow Science Inc., and it includes various physical models, e.g., shallow water model, turbulence, cavitation, viscosity, homogeneous and adiabatic bubbles, porous media, sediment scour, and surface tension. In Flow-3D model, water surface is simulated by the VOF (Volume of Fluid) method. Flow equations are solved numerically using finite-difference (or finite-volume) scheme. The computation area in Flow-3D is subdivided into fixed rectangular meshes.

One of the most attractive characteristics of Flow-3D is the so-called FAVOR^{TM} (Fractional Area-Volume Obstacle Representation) model used for constructing meshes near the solid boundary. This particular model became the main reason why I chose to apply this CFD tool to the present study. It has been shown that using Cartesian meshes for the sharply curving solid boundaries can result in a substantial loss of momentum in transient flow (Mampaey and Xu 1995). In the present study, as I consider the surge-induced impact pressure near the toe of a vertical wall where the solid boundary abruptly changes its direction, it is reasonable to ask if Flow-3D suffers from numerical flow losses too. The answer turns to be no. The FAVOR^{TM} model eliminates sharp direction changes by smoothly blocking out fractional portions of grid cell faces and volumes. It also has a collection of special algorithms for computing interfacial areas, evaluating wall stresses, enhancing numerical stability, and for computing advection along solid boundaries.

Therefore, it could be said that Flow-3D is an appropriate tool to investigate the velocity and pressure fields in the vicinity of the wall.

According to the user manual, the general forms of mass conservation law and momentum conservation law in a Cartesian coordinate system (x_1, x_2, x_3) used in Flow-3D are written as

$$\frac{\partial}{\partial x_i}\left(u_i A_i\right) = 0 \tag{5.1}$$

$$\frac{\partial u_i}{\partial t} + \frac{1}{V_F}\left(u_j A_j \frac{\partial u_i}{\partial x_j}\right) = -\frac{1}{\rho}\frac{\partial p}{\partial x_i} + g_i + f_i \tag{5.2}$$

where u_i and u_j are the velocity components in the i and j directions. A_i and A_j are the fractional areas open to flow in the i and j directions. V_F is the volume fraction of fluid in each mesh. g_i is the gravitational force in the i direction. f_i is the diffusion term in the i direction. The equations of fluid motion are closed with the standard two-equation model (k-e model) or the LES (Large Eddy Simulation) model for turbulence closure.

Some representative parameters of the water used in the numerical calculations are listed in Table 5.1. Note that I here assume that all of these parameters are constant during the entire dam-break and impingement processes. Water is regarded as an incompressible fluid here due to the existence of free water surface.

Table 5.1 Representative parameters of water used in numerical calculations

Temperature (K)	Density (kg/m^3)	Dynamic viscosity (mPa・s)	Surface tension (mN/m)
293.2	998.2	1.002	72.75

5.3 Verifications of the analytic solution

In order to directly compare the numerical results with laboratory data and the theory, I rebuild the flume used in Xie and Shimozono (2022) with the same scale in the Flow-3D. Four experimental cases considered in the laboratory works are then simulated numerically. The Euler's equation has been selected as the governing equation as I need to compare the numerical data with the theoretical solutions of the velocity and the pressure fields.

I conduct the calculations in the $x - y$ plane without considering the third dimension (by setting only one mesh in the third dimension). The mesh size on the $x - y$ plane is set to 0.5 × 0.5 mm (the discussion on if this mesh size is small enough is provided in Appendix C). The calculation time step is shorter than 4×10^{-5} s (for the impingement process, it is no more than 2×10^{-5} s), and the output time step is 0.001 s for all cases. The following Figure 5.1 presents the typical dam-break flow generated by the present numerical model (H=12 cm), where the color shade represents the magnitude of the horizontal velocity component.

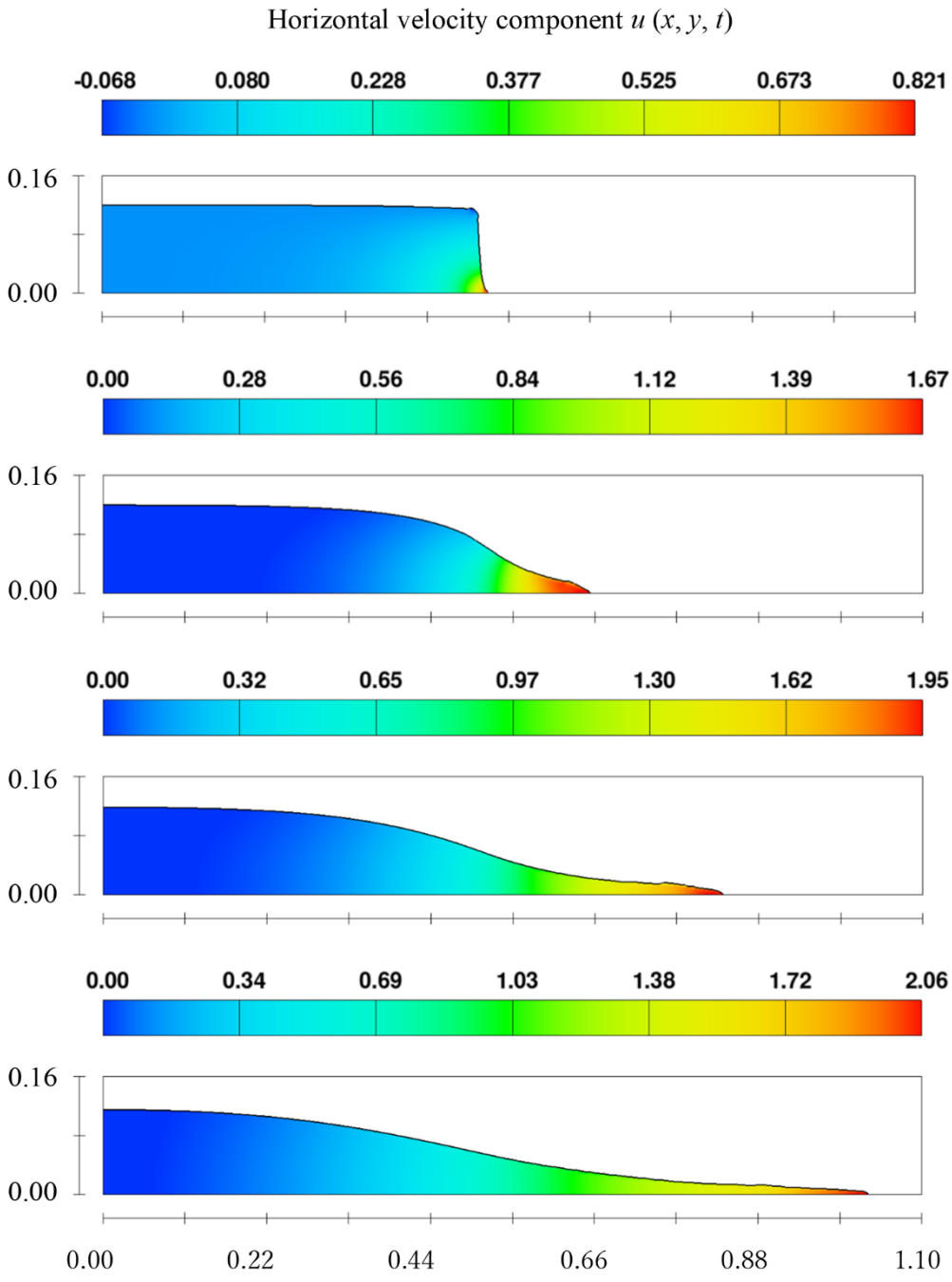
Horizontal velocity component u (x, y, t)
-0.068
0.080
0.228
0.377
0.525
0.673
0.821
0.16
0.00
0.00
0.28
0.56
0.84
1.12
1.39
1.67
0.16
0.00
0.00
0.32
0.65
0.97
1.30
1.62
1.95
0.16
0.00
0.00
0.34
0.69
1.03
1.38
1.72
2.06
0.16
0.00
0.00
0.22
0.44
0.66
0.88
1.10

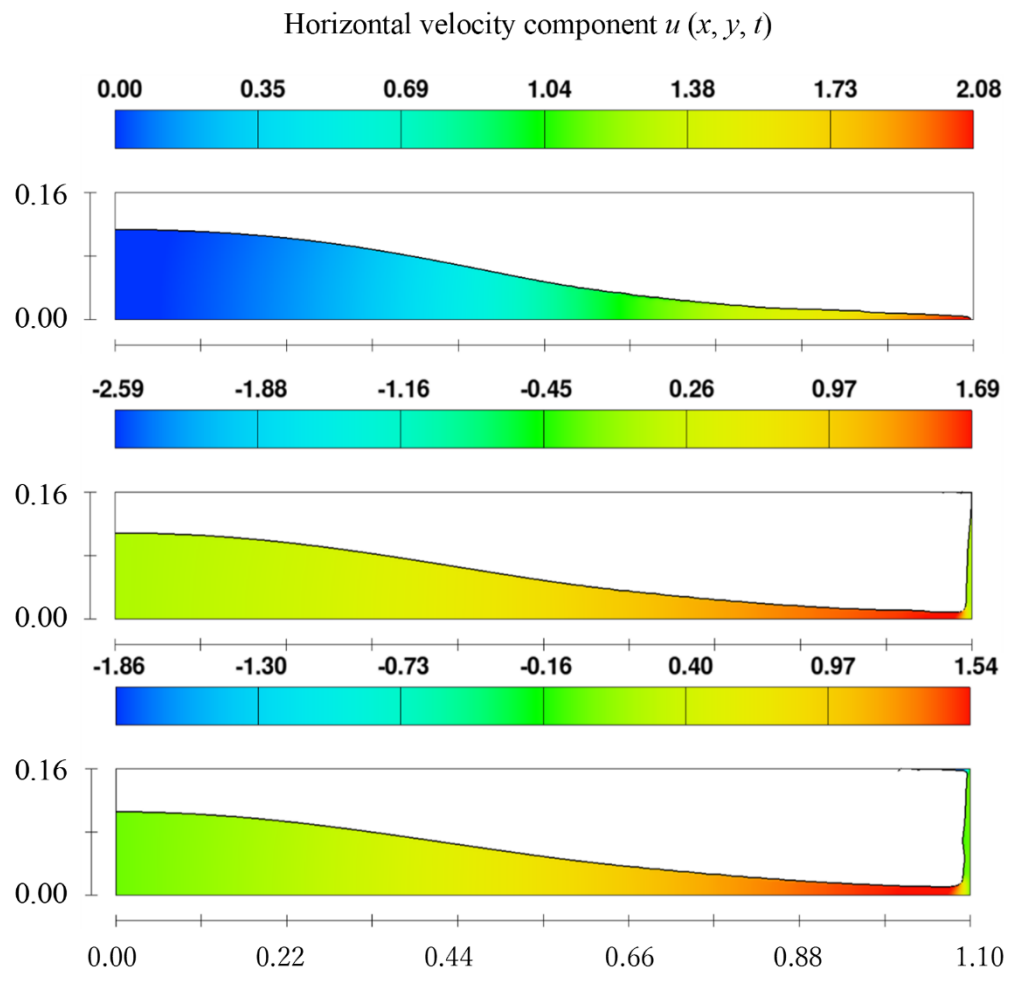

Fig. 5.1 Fluid motion of inviscid dam-break flow (H = 12 cm) 0.033 s, 0.133 s, 0.233 s, 0.333 s, 0.367 s, 0.433 s and 0.467 s after the water column starts collapsing (from top to bottom). Lengths are in m and velocity in m/s.

Compared with Figure 3.3, it could be understood that the surge front presented in Figure 5.1 obviously travels at a higher speed than the actual dam-break flow. This is due to the absence of viscosity and other dissipative factors. This issue will be discussed in a later section. However, we could still use the numerical data obtained from this inviscid dam-break flow to verify the soundness of the analytic solution proposed in Chapter 4, as all

the physical parameters evaluated here will be presented in their dimensionless forms. Having said this, I have to remark here that Figure 5.1 has proved that the inviscid flow is not a reasonable approximation for describing the propagation of dam-break flows, although there is still a possibility that it could be utilized to evaluate the physics during a localized impingement event.

5.3.1 Velocity field

To verify Equation (4.22) and the self-similarity assumption, I obtain the numerical data of the velocity field right after the arrival of surge on the wall (from t=0.003 s) near the bed. The following figures show the comparison between numerical results and the theoretical curves provided by Equation (4.22) in different cases.

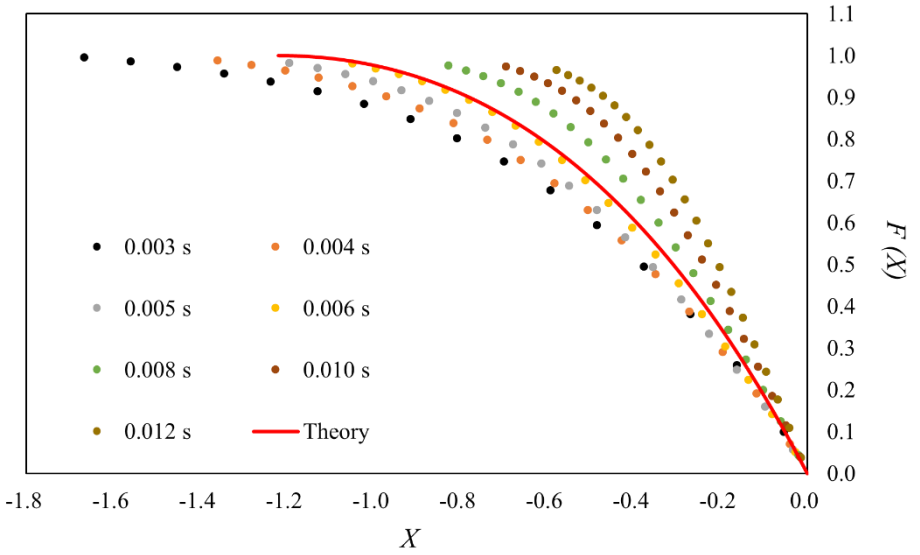
0.003 s
0.004 s
0.005 s
0.006 s
0.008 s
0.010 s
0.012 s
Theory
1.1
1.0
0.9
0.8
0.7
0.6
0.5
0.4
0.3
0.2
0.1
0.0
F (X)
-1.8
-1.6
-1.4
-1.2
-1.0
-0.8
-0.6
-0.4
-0.2
0.0
X

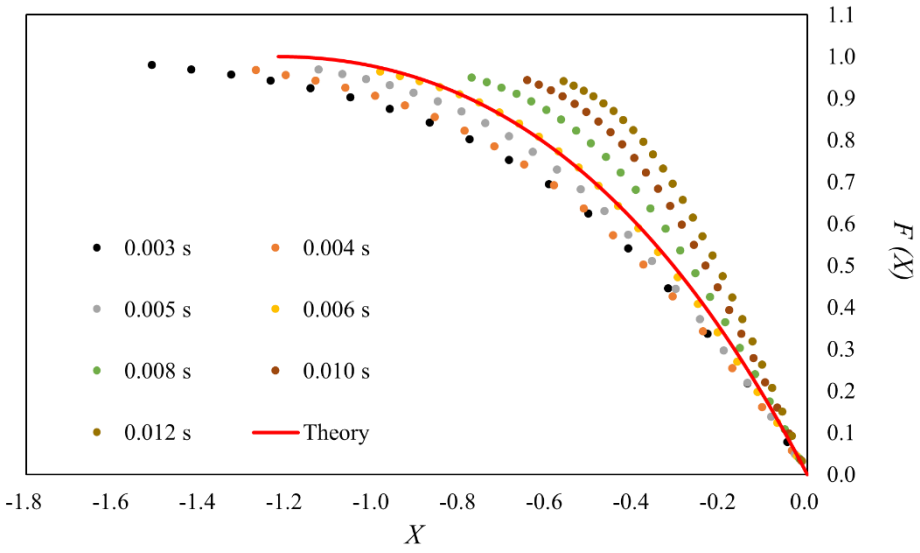
0.003 s
0.004 s
0.005 s
0.006 s
0.008 s
0.010 s
0.012 s
Theory
1.1
1.0
0.9
0.8
0.7
0.6
0.5
0.4
0.3
0.2
0.1
0.0
F (X)
-1.8
-1.6
-1.4
-1.2
-1.0
-0.8
-0.6
-0.4
-0.2
0.0
X

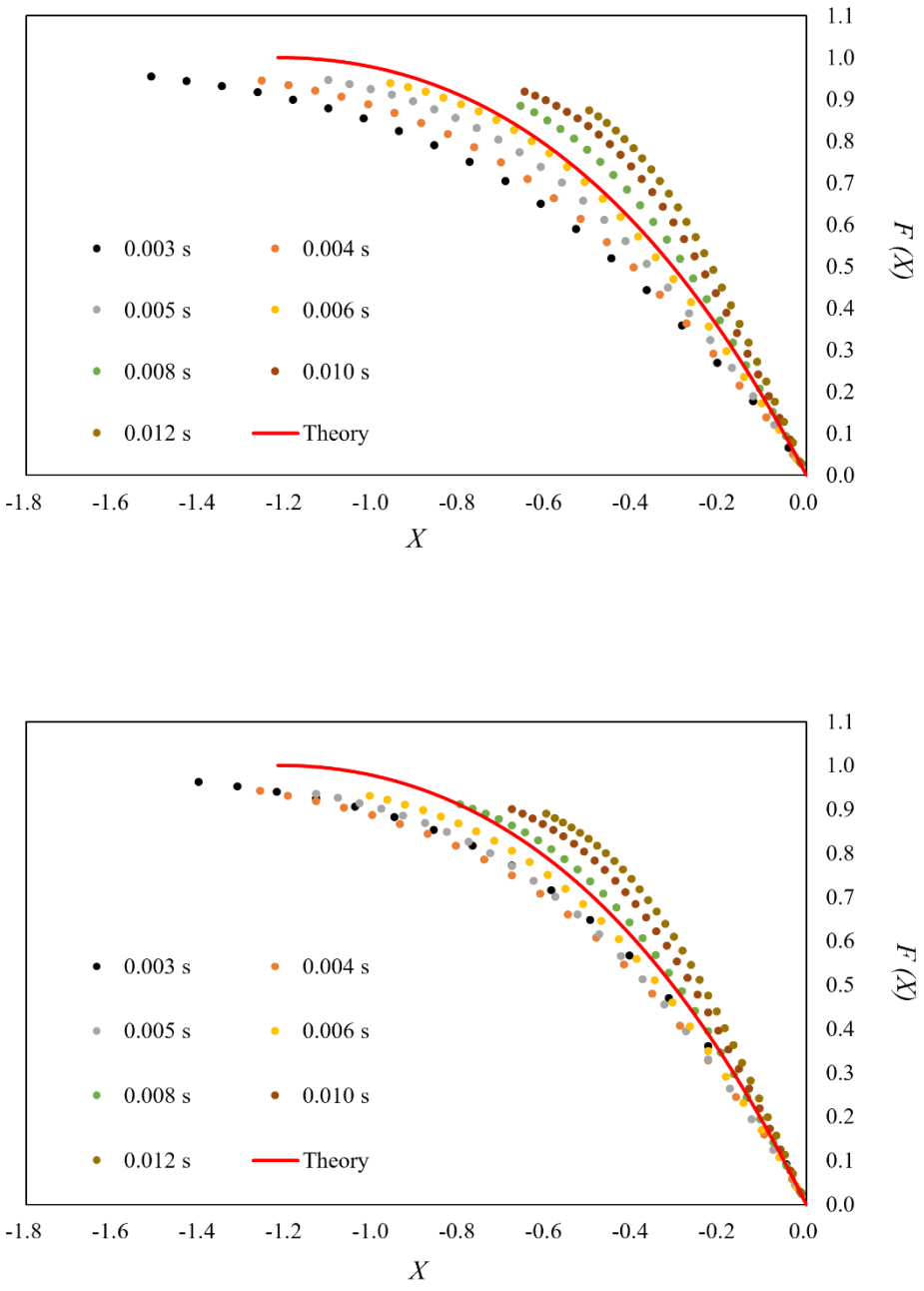

Fig. 5.2 Comparison between numerical data of $F(X)$ and the theoretical results

(from top to bottom, H=8 cm, 10 cm, 12 cm and 14 cm)

In Figure 5.2, the plots end at the locations where the differences of $F(X)$ are less than 1 % between a plot and the one on its left-hand side. I accordingly regard the values of X of these locations as L here. In Figure 5.2, the plots tilt upward when t becomes large. The value of L also shrinks with the increment of t. It is expected that for large t, the area S mentioned in Equation (4.45) will decrease to zero eventually. In other words, the magnitude of $C_{pw}(t)$ would approach 0.5 which is the well-known value for steady flow. The obvious difference between the impact pressure and the steady pressure proved that it is indeed necessary to take the unsteady term into account when considering this transient problem.

On the other hand, the theoretical curves provided by Equation (4.22) succeeded in predicting the basic tendency of the plots, especially near the wall where the plots perfectly satisfy $F'(0) = -2$ in each case (see Figure 5.3 and also refer to Equation [4.18]). This fact implies that the self-similarity assumption is reasonable when solving this impingement problem without considering the effects of viscosity and gravity. However, it could also be seen that there are apparent differences between the theory and the plots near $X=L$. One of the straightforward reasons is that the surge velocity at $X=L$ is not simply a constant number, but gradually changes along the surge. Therefore, a theory using constant incident surge velocity will inevitably generate errors when predicting the velocity field near $X=L$. Moreover, as mentioned in Chapter 4, I only applied the boundary conditions for $F(X)$ and $F'(X)$ on $X=L$. This also significantly affects the accuracy of the theory there.

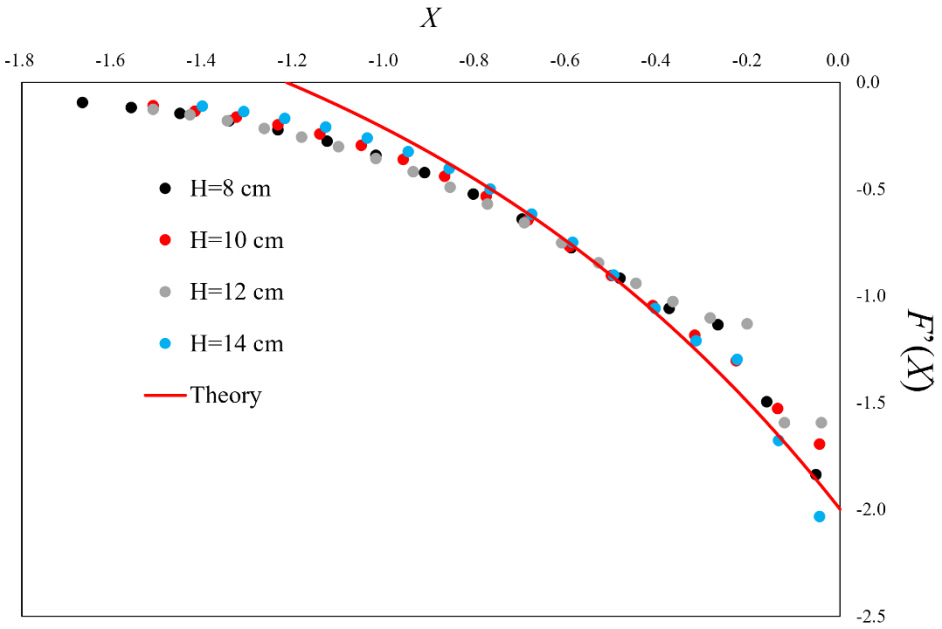

Fig. 5.3 Comparison between numerical data of $F'(X)$ and the theoretical results

(H=8 cm, 10 cm, 12 cm and 14 cm, t=0.003 s)

Figure 5.4 and 5.5 present the numerical calculation results of horizontal velocity component $G(X, Y)$ and total velocity $V(X, Y)$ for the case where H=8 cm when t=0.003 s, combined with the theoretical curves of them provided by Equation (4.34) and (4.35). Figure 5.4 clearly demonstrates that the theoretical curves of $G(X, Y)$ fit the numerical data quite well near the wall but generate some errors near $X=L$ for the same reason explained in the discussion of $F(X)$. In Figure 5.5, we could see that the theoretical curves clearly illustrate the tendency of the numerical data, that is, the magnitude of $V(X, Y)$ decreases at first near $X=L$ but increases near the wall. These two figures proved that the analytic solution proposed in Chapter 4 is not only applicable to the region infinitely close to the bed ($Y \to 0$), but also, to a certain extent, valid for finitely small Y.

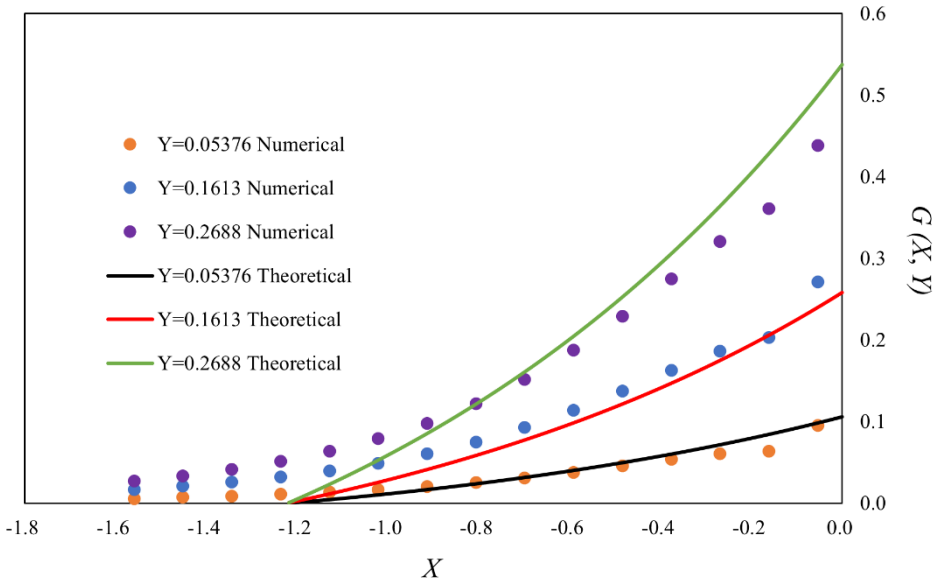

Fig. 5.4 Comparison between the numerical data of G (X, Y) and the theoretical curves provided by Equation (4.34), H=8 cm

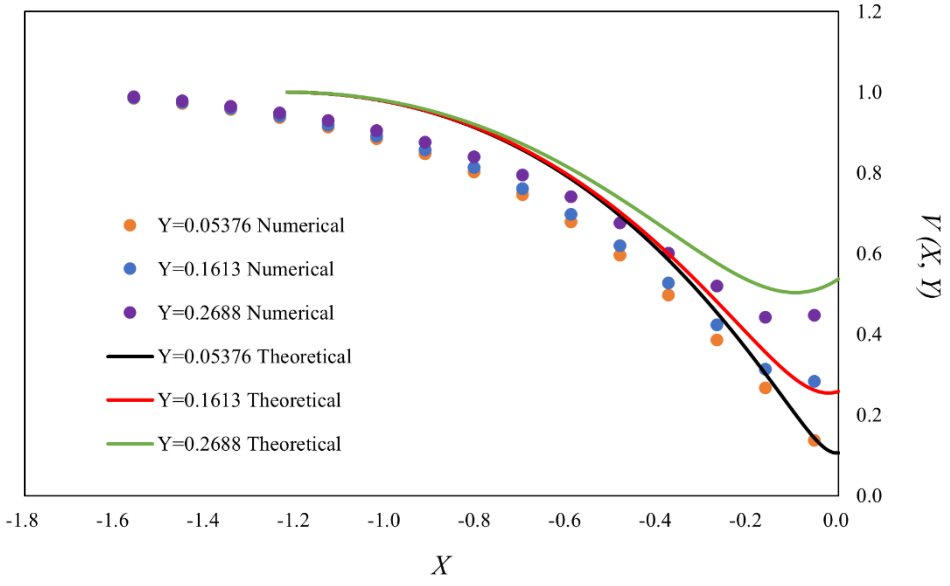

Fig. 5.5 Comparison between the numerical data of V (X, Y) and the theoretical curves provided by Equation (4.35)

Figure 5.6 presents the dimensionless vorticity distribution, which is defined as

$$\Omega = \frac{\partial F}{\partial Y} - \frac{\partial G}{\partial X} = t\omega \tag{5.3}$$

for the case where H=8 cm near the bed. It could be understood that, as predicted in Chapter 4, the vorticity holds very large value near the wall during the impingement. Therefore, we can conclude from this figure that the velocity potential theory is not applicable for surge impingement, even when the viscosity is neglected. The vorticity fades to zero for X=L, showing that the incident dam-break flow is truly irrotational and the vorticity is assuredly generated by the vertical wall.

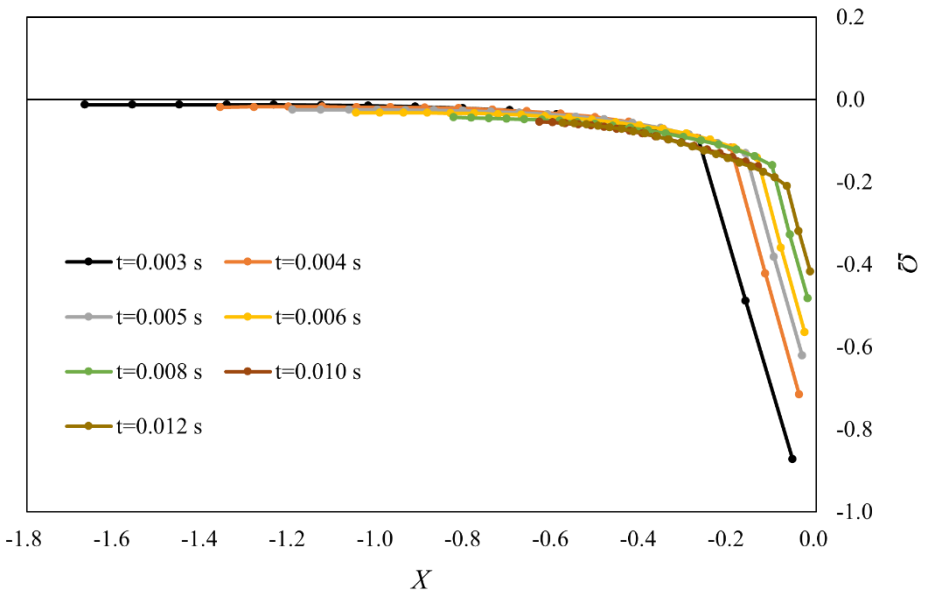

Fig. 5.6 Distribution of dimensionless vorticity with H=8 cm

In this sub-section, I compared the theoretical solution of F (X), G (X, Y) and V (X, Y) with the numerical data provided by Flow-3D using Euler's equation as the governing equation. The assumption of self-similarity has been proven reasonable for inviscid surge impingement. I have also rebutted the usage of velocity potential in the surge

impingement problem by investigating the vorticity distribution near the wall. Generally, the theory agreed with the numerical data quite well near the wall but deviated from the numerical plots near $X=L$. This is mainly due to the boundary conditions used in the analytic solution and the variation of the incident surge front velocity. Nevertheless, the viscosity and turbulence were neglected in this sub-section, and their effects will be studied in a later section.

5.3.2 Pressure field

In this sub-section, I extract the numerical pressure fields when the peak pressures appeared at the wall from Flow-3D. For the four selected cases in the present study, the following Figure 5.7 demonstrates the numerical results of $C_p(X)$ for $X \in [L, 0]$ and the theoretical curve provided by Equation (4.44) (the location of L follows the same definition described in the previous sub-section).

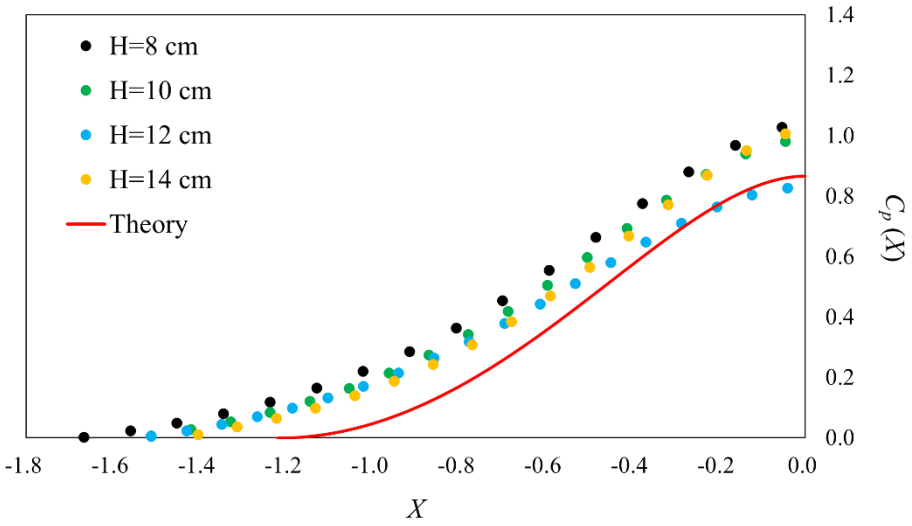

Fig. 5.7 Comparison between the numerical data of C_p (X) and the theoretical curve provided by Equation (4.44)

It could be understood from Figure 5.7 that the theoretical curve predicts the basic tendency of pressure field over [L, 0], although it slightly underestimates the magnitude of the pressure in general. The horizontal gradient of C_p (X) at the wall is found to be zero both in the numerical plots and the theoretical curve. On the other side, X=L, the horizontal gradient of pressure also turns to zero. These are the expected results of Equation (4.44). The underestimation of the theory is a consequence of the previously mentioned mismatches in the velocity field discussion (refer to Figure 5.2). As for the impact coefficient on the wall, although the numerical plots still scattered around 0.8~1.0, Equation (4.44) (or simply Equation [4.47]) agreed with them with errors of around 10%. The numerical results of the C_{pw0} are located between the median and the third quartile in Table 3.1 for P0. The theoretical value is also located in this interval.

5.4 Effects of viscosity and turbulence

Flow-3D allows users to apply various turbulence models to the simulations. In this section, I apply the standard two-equation model (*k-e* model) to induce turbulence into the viscous fluid motions, taking the case of H=8 cm as an example. The parameters listed in Table 5.1 are used here. The mesh size and time steps are the same as used in Section 5.3. The bed and the walls of the flume are assumed to be smooth enough, although the non-slip boundary condition is applied there.

Figure 5.8 (1) and (2) show the typical dam-break flow generated under this viscous model (H=12 cm here for the comparison with the laboratory records) where the color shade represents the magnitude of horizontal velocity component in Figure 5.8 (1), and it represents the turbulence energy distribution in the flow in Figure 5.8 (2). Compared with Figure 5.1, it could be easily understood that (i) there is an evolving turbulent region generated by the viscous shear flow near the solid surfaces (see Figure 5.8), and (ii) the viscous surge front velocity of is obviously slower than the inviscid one. From the view of the arrival time of surge front on the wall, it could be said that the viscous flow is closer to the actual surge-like flow generated in the laboratory works (refer to Figure 3.3). Compared with the kinetic energy of the mainstream (which is proportional to U^2), the turbulent kinetic energy is one order smaller.

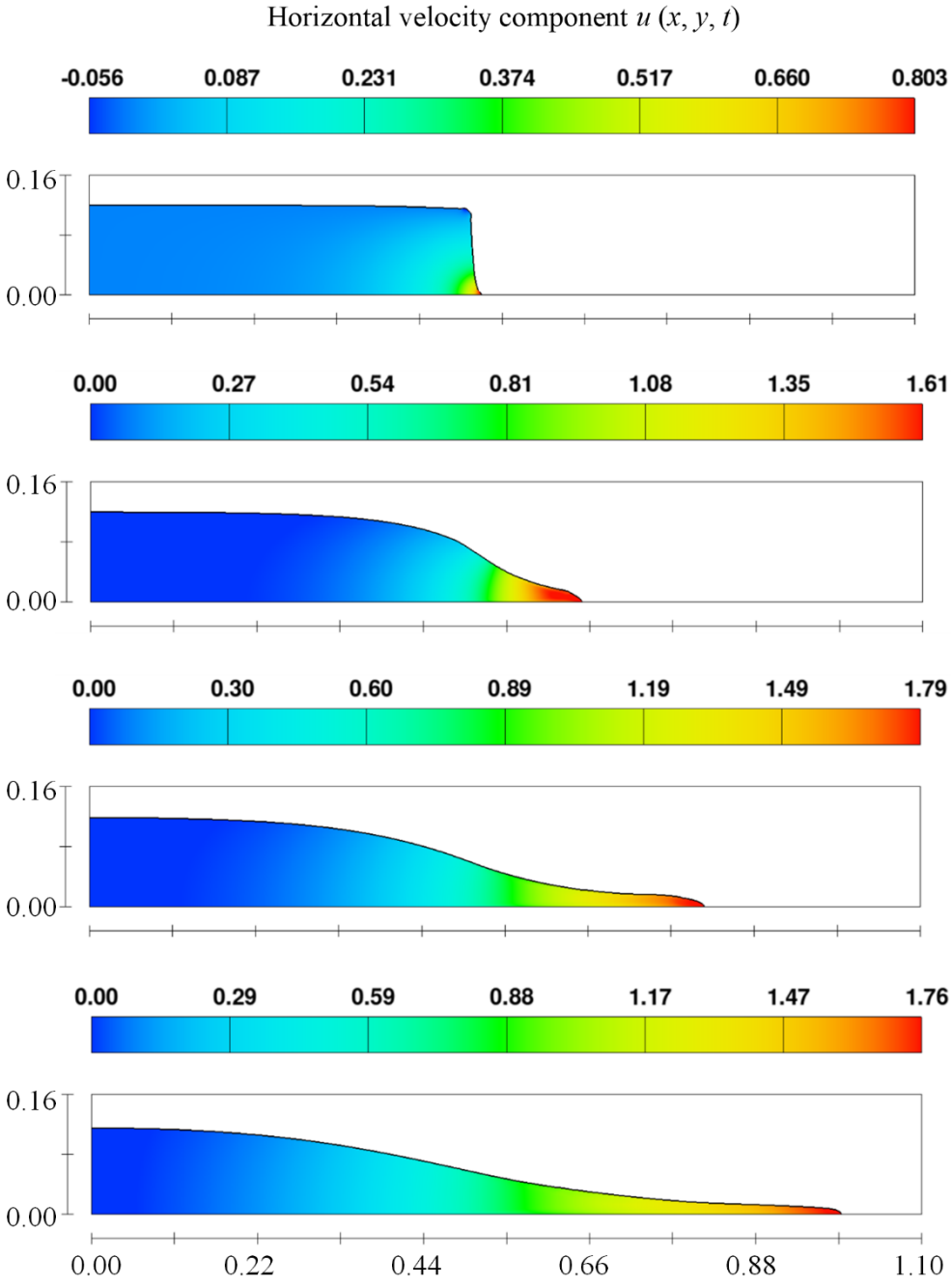
Horizontal velocity component u (x, y, t)
-0.056
0.087
0.231
0.374
0.517
0.660
0.803
0.16
0.00
0.00
0.27
0.54
0.81
1.08
1.35
1.61
0.16
0.00
0.00
0.30
0.60
0.89
1.19
1.49
1.79
0.16
0.00
0.00
0.29
0.59
0.88
1.17
1.47
1.76
0.16
0.00
0.00
0.22
0.44
0.66
0.88
1.10

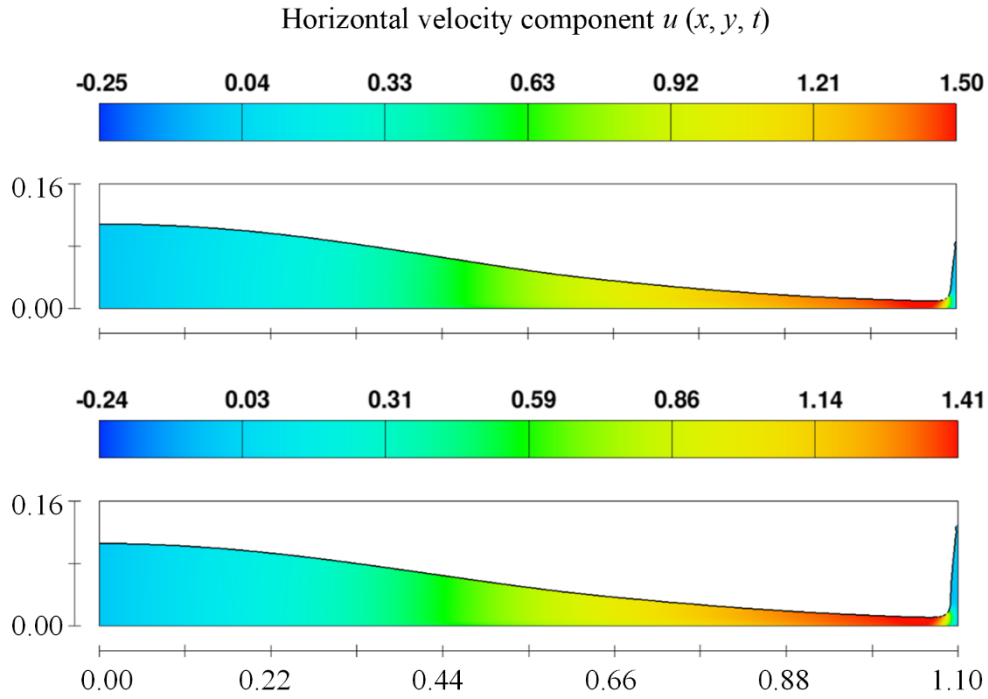

Fig. 5.8 (1) Fluid motion of viscous dam-break flow (H = 12 cm) 0.033 s, 0.133 s, 0.233 s, 0.333 s, 0.433 s and 0.467 s after the water column starts collapsing (from top to bottom). Lengths are in m and velocity in m/s.

Turbulent kinetic energy k (x, y, t)

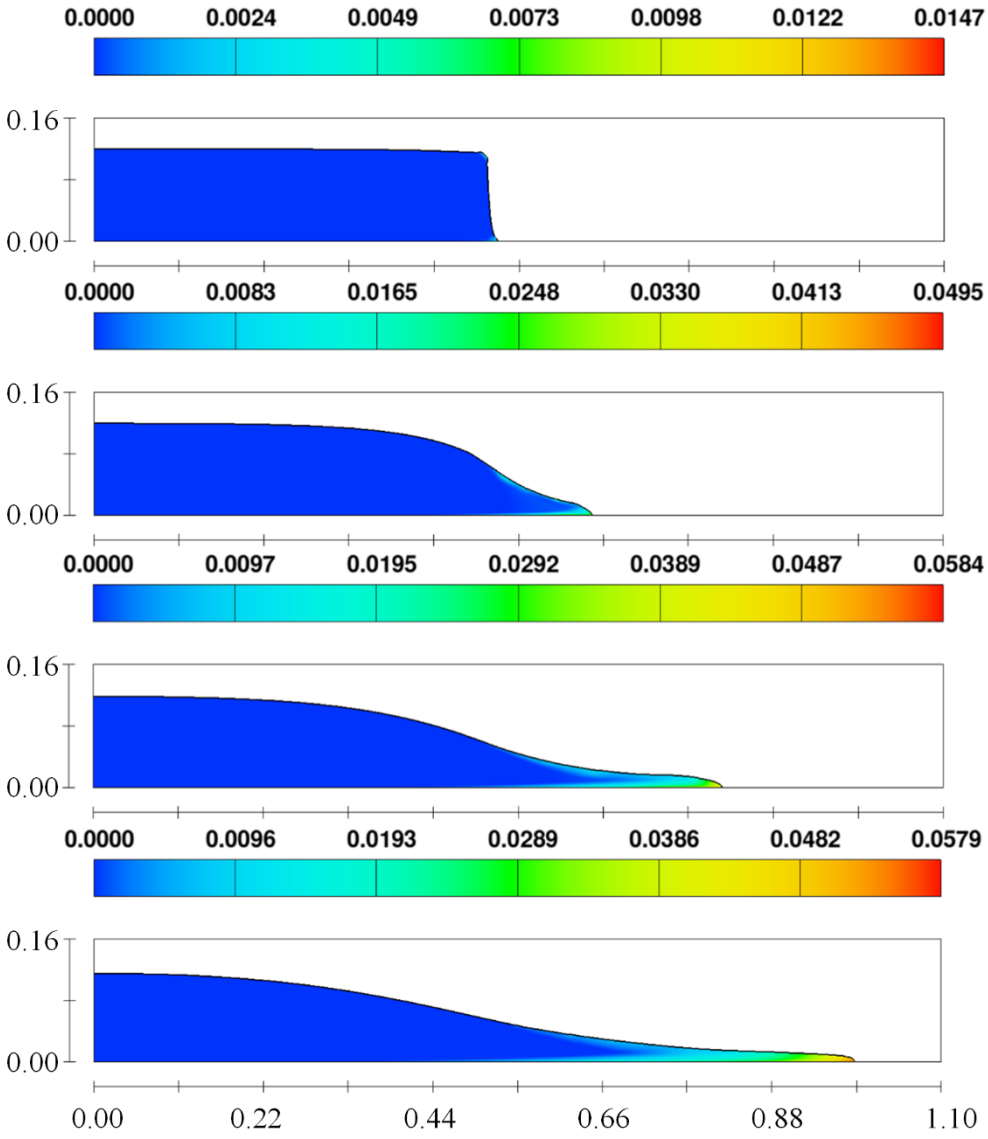

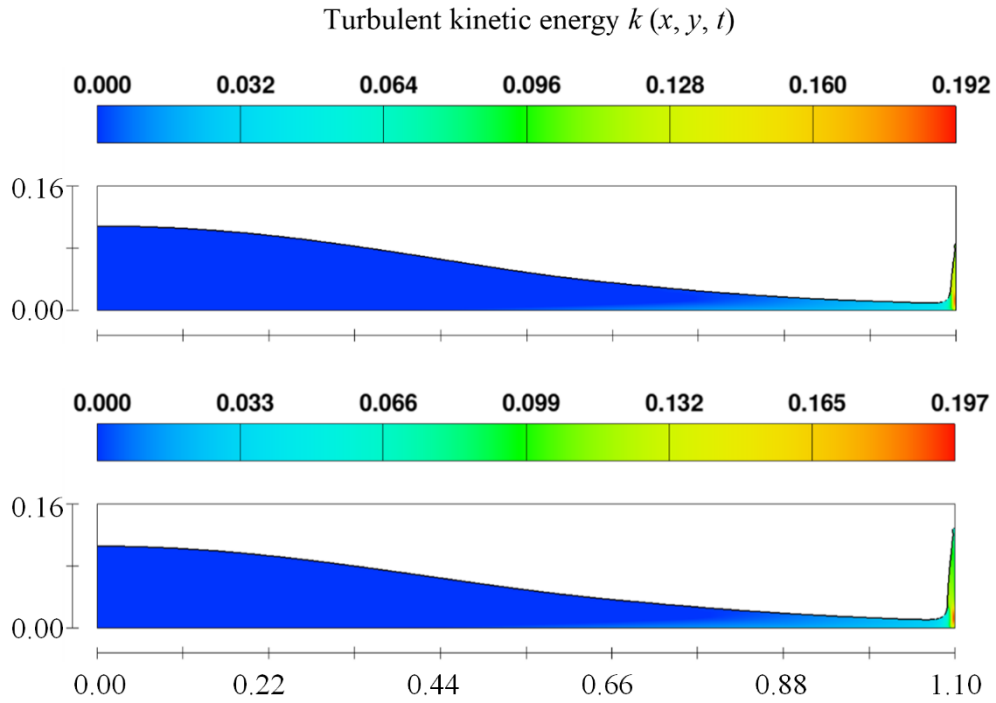

Fig. 5.8 (2) Fluid motion of viscous dam-break flow (H = 12 cm) 0.033 s, 0.133 s, 0.233 s, 0.333 s, 0.433 s and 0.467 s after the water column starts collapsing (from top to bottom). Lengths are in m and turbulent energy in m^2/ s^2.

5.4.1 Velocity field

Figure 5.9 presents a comparison of the distribution of the horizontal velocity component near the bed right before the impact (H=8 cm) in inviscid and viscous flows. The data of the viscous flow is obtained at the location y right above the bottom boundary layer following the so-called "95% rule", that is,

$$y = \left\{ \mathrm{Min}\left(y_i\right) \left| \frac{u\left(x, y_i\right)}{u\left(x, y_{i+1}\right)} \geq 0.95 \ , \ i \geq 1 \right. \right\} \tag{5.4}$$

where y_i is the value of y at i-th cell above the bottom for a specific x. In the present case, we have i=2 or 3 almost everywhere for the viscous flow. It could be understood that the water particle velocity in inviscid flow is quite close to the theoretical value proposed by Ritter (1892), and the difference is due to that we do not have a water column with infinite length at the initial stage (especially on the left-hand side of Figure 5.9). The surge front velocity of the viscous flow is, in contrast, significantly below the theoretical value, but it is close to the experimental results described in Section 3.3.3. Therefore, it is proved again here that the viscous flow in the present study is a more reasonable approximation of the actual dam-break flows in laboratory works, while the theory and the inviscid numerical results overestimate the velocity of water particles in the surge.

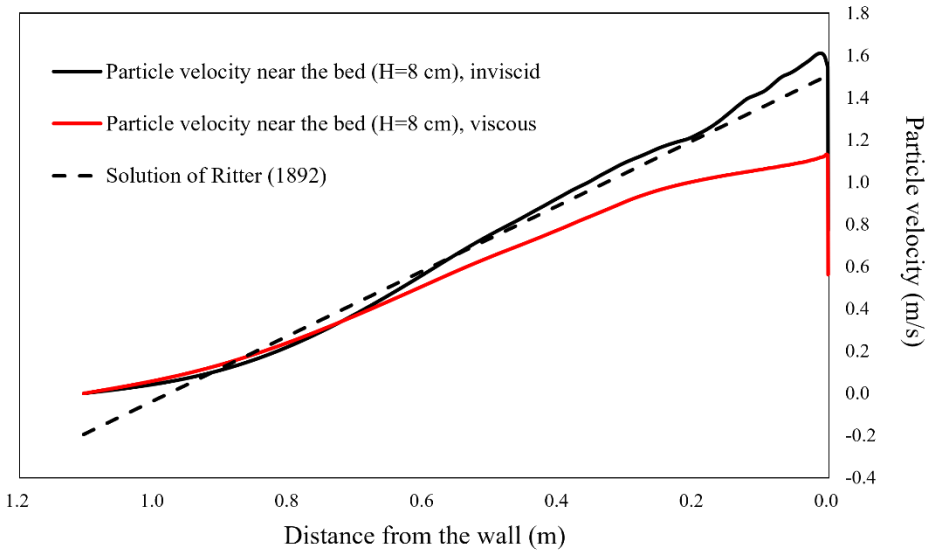

Fig. 5.9 Particle velocity near the bed in inviscid and viscous flows right before the impact, combined with the solution of Ritter (1892)

Figure 5.10 shows the comparison between the velocity fields under inviscid and viscous flow conditions in the case of H=8 cm, right after the impact (from t=0.003 s).

The velocity fields of the viscous flow were obtained outside the bottom boundary layer following the “95% rule”. From Figure 5.10, we can confirm a profound tendency in the numerical data. The *X*-*F* curves of the viscous flow do not tilt up like those curves of inviscid flow. At first (t=0.003 s), the velocity fields of inviscid and viscous flows are quite close to each other, showing that the viscosity and turbulence have not brought significant affections at this stage. However, with t increases, the curves behave in different ways. The curves for viscous flow present a notable long-life self-similarity, even compared to the curves of inviscid flow. This fact implies that it might also be possible to derive a self-similarity solution for the velocity field when viscous terms are considered in the governing equation.

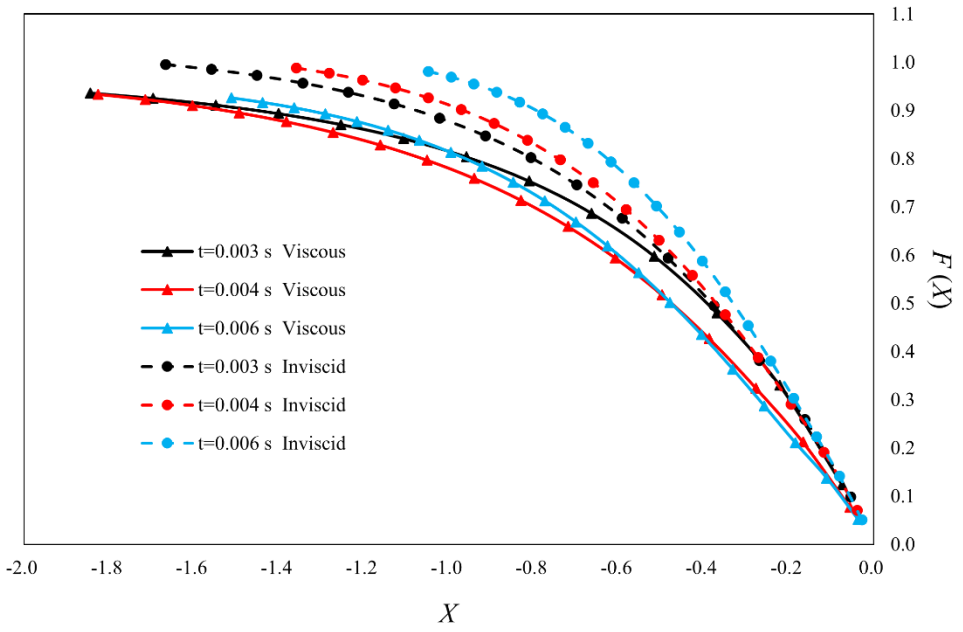

Fig. 5.10 Comparison between the numerical data of F (X) in viscous and inviscid flows during the impingement

In this sub-section, I have compared the velocity fields between viscous and inviscid flows. It has been shown that the viscosity and turbulence significantly affected fluid motion. Therefore, the comparison of the pressure field has also become necessary.

5.4.2 Pressure field

Figure 5.11 presents the comparisons of $C_p\,(X)$ between the viscous and the inviscid flows. The figure clearly demonstrates that although viscosity and turbulence largely suppressed the magnitude of impact pressure in the viscous flow, the values of $C_p\,(X)$ agreed quite well under the two flow conditions. However, in Figure 5.12, compared with the laboratory data, the numerical value of the impact pressure on the wall, $\rho U^2 C_{pw0}$, is obviously larger than the median value (even larger than the 95% percentile suggested by Equation (3.6)) in the inviscid flow. On the other hand, the impact pressure obtained in viscous flow matches the laboratory data more reasonably. As it is proved in Appendix A, the laboratory data obtained in the laboratory works only contain minor errors. Therefore, the pressure evaluations of Flow-3D involving viscosity and turbulence have better consistency with reality.

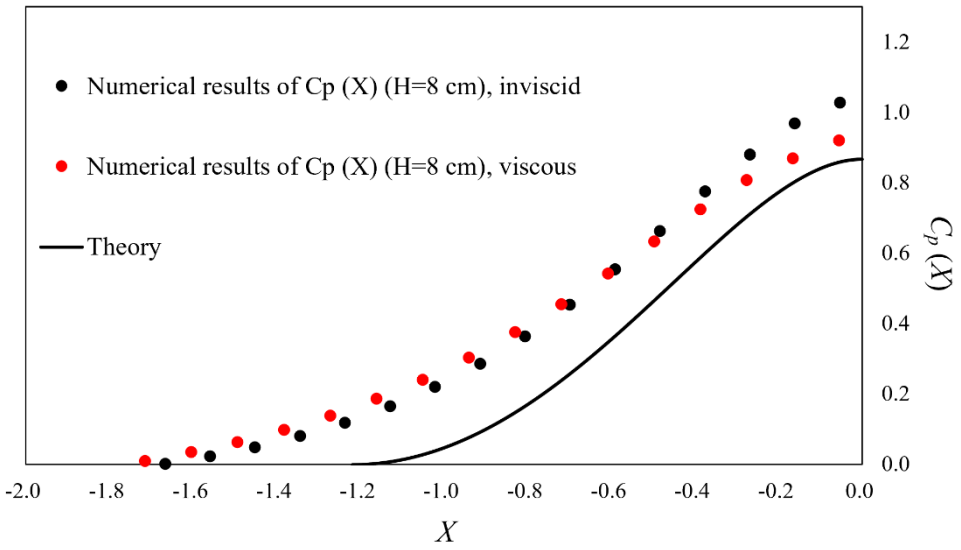

Fig. 5.11 Comparison between the numerical data of C_p (X) in inviscid and viscous flows, with the theoretical curve provided by Equation (4.44)

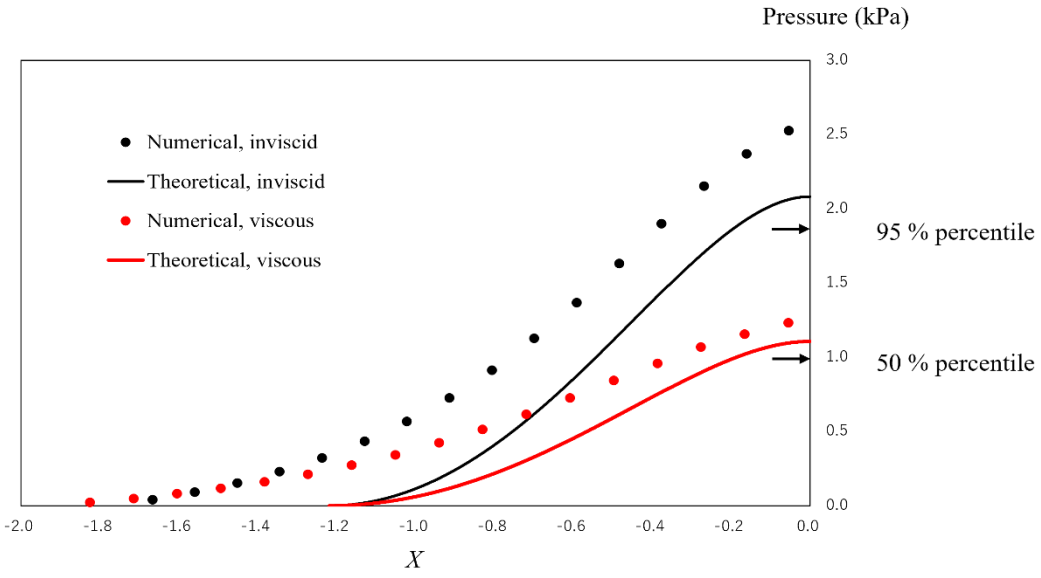

Fig. 5.12 Comparison between the numerical data of impact pressure in inviscid and viscous flows, with the theoretical curve provided by Equation (4.44).

In this Chapter, I verified the results obtained from previous chapters and presented some very rudimentary investigations on the effects of viscosity and turbulence using a CFD tool, Flow-3D.

For the inviscid simulations, although the fluid motions are different from what have been observed in laboratory works, I utilized the dimensionless forms of the numerical data to conduct some verifications. The results of the velocity field supported the self-similarity assumption used in Chapter 4, which consequently resulted in pressure fields being consistent with Equation (4.44). The impact coefficient on the vertical showed the validity of Equation (4.47).

However, the calculations using viscous flow showed that the effects of viscosity and turbulence are possibly not negligible when discussing the actual fluid motions. The simulation results of the viscous dam-break flow were generally consistent with the laboratory records in terms of fluid motions. On the other hand, although the viscous flow demonstrated velocity fields that were significantly different from those of inviscid flows, the distribution of $C_p\,(X)$ under these two flow conditions was very similar.

Chapter 6
Conclusion

To sum up the main results obtained in the present study, the following concluding remarks can be made.

1. The laboratory experiments and a stochastic analysis were conducted to evaluate the impact pressure generated by water surge impingement onto a vertical wall. The impact coefficient on the wall, a highly stochastic parameter, was reasonably modeled by the Fréchet distribution. A predictive formula was proposed for the stochastic distribution of the impact coefficient on the wall, which involved only the surge front velocity right before the impact as the governing factor. The surge front slope was proved not to have significant affection on the impact pressure near the bed.

2. An analytic solution was proposed to elucidate the physics of surge impact. A well-posed physical model was built with reasonable initial and boundary values. Under the assumption of self-similarity, an analytic solution of the velocity field near the bed was derived. The pressure field in the vicinity of the wall was then studied, and the impact coefficient on the wall, which is a finite constant number, was explicitly calculated. It was shown that the surge front velocity is theoretically the governing factor, and the predicted value of the impact pressure is consistent with the laboratory data and an engineering guidebook.

3. Numerical evaluation for the process of surge impact was carried out with a CFD software, Flow-3D. Under the inviscid mode, the numerical results of the velocity and pressure fields agreed with the analytic solution quite well, suggesting that the self-similarity assumption is reasonable for studying surge impact for inviscid flow. Under the viscous mode, the effects of viscosity and turbulence were investigated. The simulation results were consistent with the laboratory records. It was also found that although the velocity field in viscous flow was quite different from the one in inviscid flow, the impact coefficients showed a good agreement.

There are some recommended future works based on this study. (1) In the present study, impact pressure is the main topic. However, in actual engineering works, impact force (the integral of pressure over a certain area) is also a significant physical parameter which has to be evaluated. Furthermore, the impact force could generate tremendous bending moment on the structure. This is another important issue in structure designs. (2) As mentioned in Chapter 5, it is worth attempting to propose a self-similarity solution for the impact pressure considering viscous and turbulent terms. (3) Aeration in the incident flow is frequently observed in the surge flow generated by wave breaking. Therefore, laboratory experiments on the aerated surge impact might be fruitful.

Appendix A

Variability of the measured impact pressure by the sampling rate

In Chapter 3, I used pressure sensors to measure the impact pressure on the vertical panel. The sampling rate of the pressure measurement was set to 500 Hz, which was relatively low compared to previous studies. Here, I investigate how the sampling rate affects the impulsive parameter using available data from a previous study. I used a pressure dataset obtained by Lobovský et al., (2014) with a sampling rate of 20,000 Hz. The dataset consists of repeated pressure time series of 100 runs measured on a vertical panel under a similar experimental setup to mine (H = 0.3 m). I re-sampled the dataset at 500 Hz and compared the stochastic characteristics of the impact pressure between the original and re-sampled datasets. Figure A.1 plots the cumulative percentile distributions of the impact pressure, and Table A.1 summarizes representative statistic parameters.

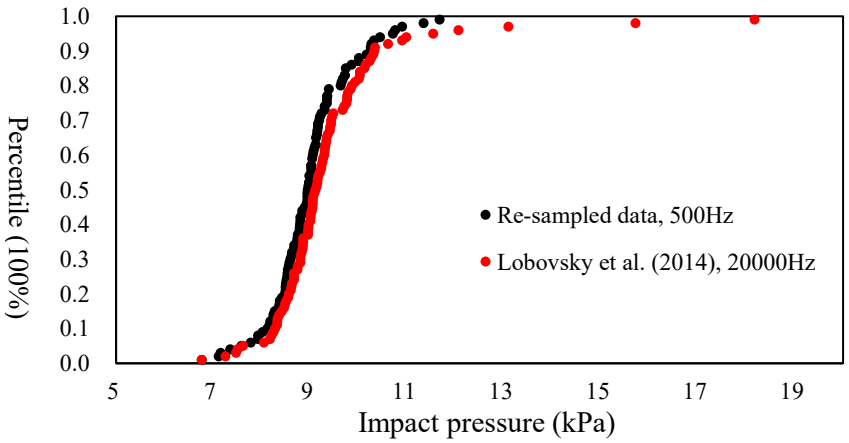

Fig. A.1 Comparison of the cumulative percentile distribution of impact pressure between the original data of Lobovský et al. (2014) and the re-sampled data using a sampling rate of 500 Hz

Table A.1 Comparison of percentiles of impact pressure between the original data of Lobovský et al. (2014) and the re-sampled data using a sampling rate of 500 Hz

Percentiles	Lobovský et al. (2014) (kPa)	Re-sampled data (kPa)
5%	7.617	7.588
25% (first quartile)	8.669	8.531
50% (median)	9.110	8.954
75% (third quartile)	9.753	9.348
95%	11.54	10.71

These results suggest that although some extremely large peaks were not captured with the sampling rate of 500 Hz (less than 5%), the difference between the two distributions was lower than 5% in the lower percentile range. Also, the fat-tailed effect was commonly observed in the two distributions (according to the 5%, 50%, 95% percentiles of the data). From this comparison, we could say that the sampling rate of 500 Hz was able to capture the basic stochastic characteristic of the impact pressure, although the measured data tend to underestimate extremely large peaks.

Additionally, Figure 3.16 showed that the empirical stochastic distribution agreed with the data collected from various literature quite well. Many of the authors used very high sampling rates to record impact pressure peaks. This fact also supports that the validity of the impact pressure distribution obtained in the present study.

Appendix B
Relationships between the impact pressure and the correlation coefficients

In this appendix, the correlations between the time history curves presented in Figure 3.6 and 3.7 will be discussed in detail. As mentioned in Chapter 3, the curves agree each other in terms of the general shape. However, quantitative evaluations have to be carried out to ensure that these curves assuredly have good correlations, in order to ensure the reliability of the data. Two significant physical parameters, C_p and $\tan\theta$, have been mainly discussed in this thesis. Therefore, the relationships between the correlation coefficients among the data curves and these two parameters are investigated here. Through this appendix, we could understand that C_p is more significant than $\tan\theta$ even in terms of the entire time history span.

Figure B.1 and B.2 present the relationship between C_p and the correlation coefficient $R^2_{C_p}$ for P0 and P1. Here, the definition of $R^2_{C_p}$ is that: the correlation coefficient between an arbitrary time history curve and the curve which provides the median value of C_p, within the range of Figure 3.6 and 3.7 (in practices, I use the curve of 52% percentile). From this comparison, we could clearly figure out how influential the C_p to the entire time span.

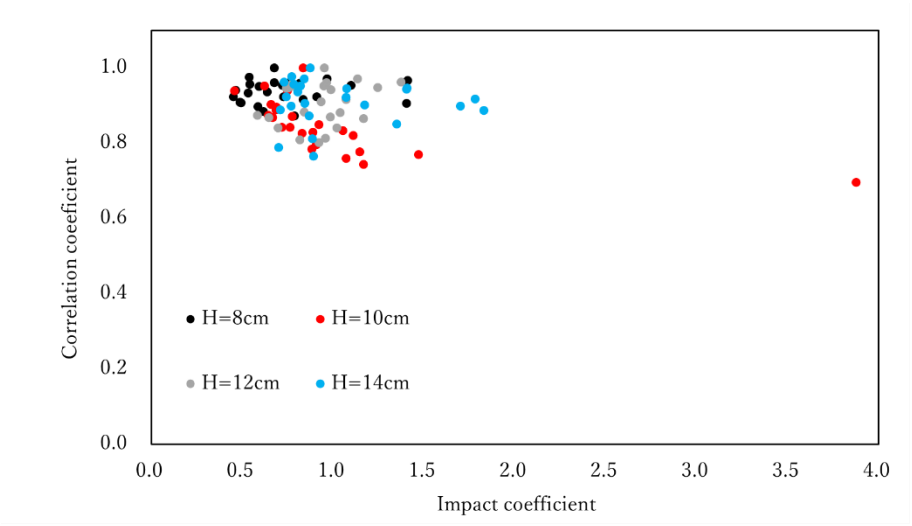

Fig. B.1 Relationship between C_p and $R^2_{C_p}$ at P0 (H=8, 10, 12 and 14 cm)

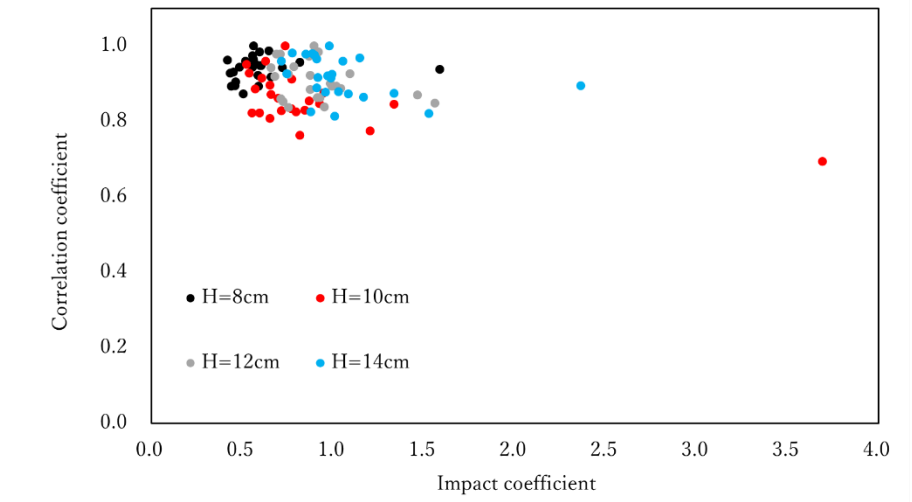

Fig. B.2 Relationship between C_p and $R^2_{C_p}$ at P1 (H=8, 10, 12 and 14 cm)

From these figures, it could be understood that, both at P0 and P1, the values of $R^2_{C_p}$ decrease slightly when C_p increase. This means that a larger impact coefficient could influence the entire time history curve, driving it deviate from the curve which provides the median value of C_p. One of the possible reasons is that a large impact pressure triggers

a high splash in the run-up water. The significant difference in the fluid motion after the impact will influence the pressure evolution after the impact pressure peak, until the run-up water is yanked back by gravity.

Figure B.3 and B.4 present the relationship between tanθ and the correlation coefficient $R^2_{\tan\theta}$ for P0 and P1. Here, the definition of $R^2_{\tan\theta}$ is that: the correlation coefficient between an arbitrary time history curve and the curve which provides the median value of tanθ, within the range of Figure 3.6 and 3.7 (similar to $R^2_{C_p}$, I use the curve of 52% percentile). From this comparison, we could clearly figure out that tanθ has no significant influence from the view of the entire time span.

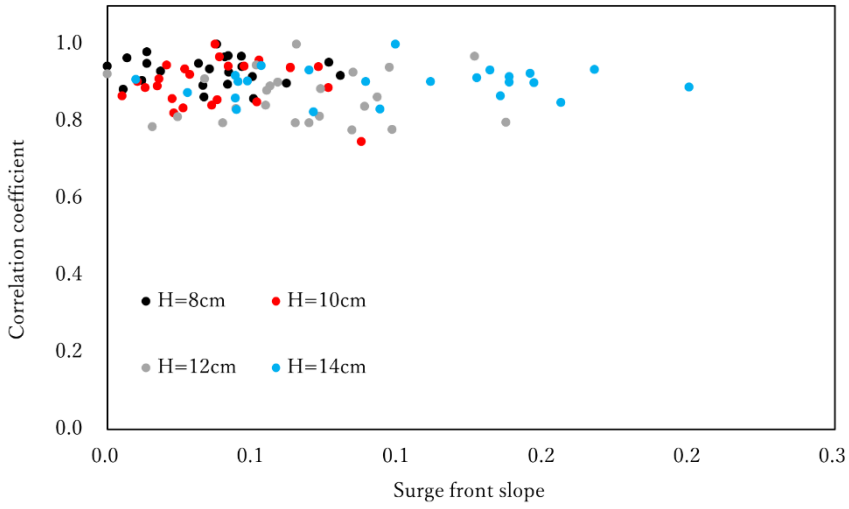

Fig. B.3 Relationship between tanθ and $R^2_{\tan\theta}$ at P0 (H=8, 10, 12 and 14 cm)

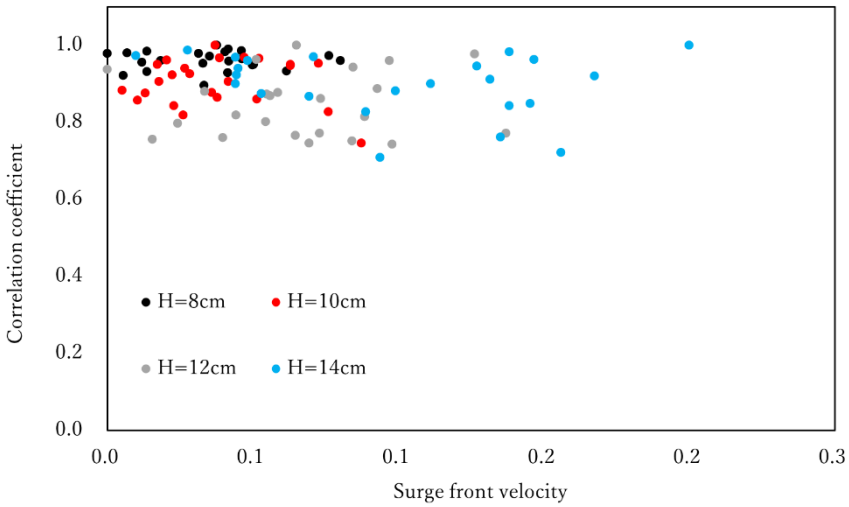

Fig. B.4 Relationship between tanθ and $R^2_{\tan\theta}$ at P1 (H=8, 10, 12 and 14 cm)

From Figure B.3 and B.4, we could not see any conspicuous correlation between tanθ and $R^2_{\tan\theta}$ as the plots are almost horizontally distributed in the figures. The reason is that although the slope of the incident surge front could slightly affect the impact pressure peaks (as discussed in Chapter 3), it could not affect the pressure evolution during the run-up process. The dominant factors of the run-up pressure are the velocity of the subsequent surge flow and the water depth there.

All in all, we could say that the experimental data have agreed each other well and the repeatability is satisfactory, as the values of the correlation coefficients are generally quite high throughout Figure B.1-B.4. This fact suggests that the data collected in the laboratory works are reliable in terms of repeatability.

Appendix C

Verification of the mesh size used in the numerical calculations

Figure 11 demonstrates the numerical results of the velocity field using mesh size of 0.5 ×0.5 mm and 1.0×1.0 mm at t=0.003, 0.006 and 0.010 s with H=8 cm. This comparison shows that the choice of mesh size brought no significant difference here, ensuring that the mesh size of 0.5 × 0.5 mm was a reasonable choice for the calculations, given that the mesh size is needed to be tiny enough to describe an impingement event.

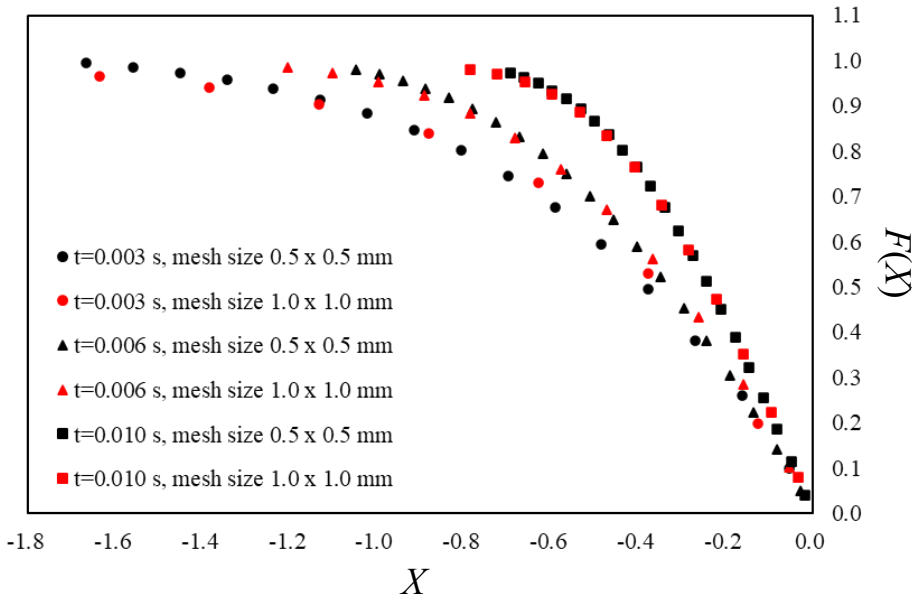

Fig. C.1 Comparison between the velocity fields using mesh sizes of 0.5 ×0.5 mm and 1.0×1.0 mm with H=8 cm

Bibliography

1. Al-Faesly, T., Palermo, D., Nistor, I. and Cornett, A. 2012. “Experimental modeling of extreme hydrodynamic forces on structural models.” International Journal of Protective Structures, 3(4), 477-505.
2. Al-Faesly, T., Nistor, I., Palermo, D. and Cornett, A. 2013. “Experimental study of structures subjected to hydrodynamic and debris impact forces.” 4th Specialty Conference on Coastal, Estuary and Offshore Engineering.
3. Allsop, N. W. H., McKenna, J. E., Vicinanza, D. and Whittaker, T. T. J. 1997. “New design methods for wave impact loadings on vertical breakwaters and seawalls” In Coastal Engineering, 1996, (2508-2521).
4. Arnason, H., Petroff, C. and Yeh, H. 2009. “Tsunami bore impingement onto a vertical column.” Journal of Disaster Research, 4(6), 391-403.
5. Asakura, R., Iwase, K., Ikeya, T., Takao, M., Kaneto, T., Fujii, N. and Ohmori, M. 2002. “The tsunami wave force acting on land structures.” Proceedings of the 28th International Conference on Coastal Engineering, Cardiff, Wales, 1191-1202.M..
6. ASCE/SEI 2017. “Minimum Design Loads and Associated Criteria for Buildings and Other Structures” American Society of Civil Engineers, 7-16.
7. Bagnold, R. A. 1939. “Interim report on wave-pressure research.” Journal of the Institution of Civil Engineers, 12(7), 202-226.
8. Batchelor G. K. 1973. “An Introduction to Fluid Dynamics.” Cambridge University Press.
9. Blackmore PA, Hewson PJ. 1984. “Experiments on full-scale wave impact pressures.” Coast. Eng. 8:331–46.
10. Bogaert H, Léonard S, Brosset L, Kaminski M. 2010. “Sloshing and scaling: results from Sloshel project.” Proc. Int. Offshore Polar Eng. Conf., 20th, 20–25th June, Beijing, China.

11. Bullock GN., Crawford AR., Hewson PJ., Walkden MJA. and Bird PAD. 2001. “The influence of air and scale on wave impact pressures.” Coast. Eng. 42:291–312.
12. Chanson, H. 2009. “Application of the method of characteristics to the dam break wave problem.” Journal of Hydraulic Research, 47(1), 41-49.
13. Chatjigeorgiou, I. K., Cooker, M. J., Korobkin, A. A. 2016. “Three-dimensional water impact at normal incidence to a blunt structure.” Proc. R. Soc. Lond. A 472, 20150849.
14. Chuang, W. L., Chang, K. A., Kaihatu, J., Cienfuegos, R. and Mokrani, C. 2020. “Experimental study of force, pressure, and fluid velocity on a simplified coastal building under tsunami bore impact.” Natural Hazards, 103(1), 1093-1120.
15. Cooker, M. J. and Peregrine, D. H. 1995. “Pressure-impulse theory for liquid impact problems.” Journal of Fluid Mechanics, 297, 193-214.
16. Cross, R. H. 1967. “Tsunami surge forces.” Journal of the Waterways and Harbors Division, 93(4), 201-231.
17. Cumberbatch, E. 1960. “The impact of a water wedge on a wall.” Journal of Fluid Mechanics, 7(3), 353-374.
18. Cuomo, G., Piscopia, R. and Allsop, W. 2011. “Evaluation of wave impact loads on caisson breakwaters based on joint probability of impact maxima and rise times.” Coastal Engineering, 58(1), 9-27.
19. Deng, X., Liu, H. and Lu, S. 2018. “Analytical study of dam-break wave tip region.” Journal of Hydraulic Engineering, 144(5), 04018015.
20. Dias F. and Ghidaglia J. M. 2018. “Slamming: Recent Progress in the Evaluation of Impact Pressures.” Annu. Rev. Fluid Mech. 2018.50:243-273.
21. Douglas, S., & Nistor, I. 2015. “On the effect of bed condition on the development of tsunami-induced loading on structures using OpenFOAM.” Natural Hazards, 76(2), 1335-1356.
22. Dressler, R. F. 1952. “Hydraulic resistance effect upon the dam-break functions.” Journal of Research of the National Bureau of Standards, 49(3), 217-225.
23. Dressler, R. F. 1954. “Comparison of theories and experiments for the hydraulic dam-break wave.” Int. Assoc. Sci. Hydrology, 3(38), 319-328.

24. Duan W. Y., Xu G. D., Wu G. X. 2009. “Similarity solution of oblique impact of wedge-shaped water column on wedged coastal structures.” Coastal Eng. 56, 400-407.
25. Faltinsen, O. M. 2005. “Hydrodynamics of High-Speed Marine Vehicles” Cambridge University Press, 313-317.
26. FEMA P-646 2019. “Guidelines for Design of Structures for Vertical Evacuation from Tsunamis”. 3rd ed Washington, DC: Federal Emergency Management Agency.
27. Ghadirian, A., Bredmose, H. 2019. “Pressure impulse theory for a slamming wave on a vertical circular cylinder.” Journal of Fluid Mechanics, 867: R1.
28. Hattori M, Arami A, Yui T. 1994. “Wave impact pressure on vertical walls under breaking waves of various types.” Coast. Eng. 22:79–114.
29. Henry A, Rafiee A, Schmitt P, Dias F, Whittaker T. 2014. “The characteristics of wave impacts on an Oscillating Wave Surge Converter.” J. Ocean Wind Energy 1:101–110.
30. Heyns JA., Malan AG., Harms TM., Oxtoby OF. 2013. “Development of a compressive surface capturing formulation for modelling free-surface flow by using the volume-of-fluid approach.” Int. J. Numer. Meth. Fluids 71(6):788–804.
31. Kitahra M and Ishihara T. 2020. “Prediction of seismic loadings on wind turbine supportstructures by response spectrum method considering equivalent model damping of support structures and reliability level” Wind Energy Vol. 23(6):1422-1443.
32. Kolmogorov AN. 1942. “Equations of motion of an incompressible turbulent fluid.” Izv Akad Nauk SSSR Ser Phys. 6:56–58.
33. Hu, C. and Sueyoshi, M. 2010. “Numerical simulation and experiment on dam break problem.” Journal of Marine Science and Application, 9(2), 109-114.
34. Hugoniot H. 1887. “Memoire sur la propagation des mouvements dans les corps et specialement dans les gaz parfaits (premiere partie).” J. Ecole Polytech. 57:3–97.

35. Hugoniot H. 1889. “Memoire sur la propagation des mouvements dans les corps et specialement dans les gaz parfaits (deuxieme partie).” J. Ecole Polytech. 58:1–125.
36. Jánosi M., Jan I. M., Szabó, D. K. G., Tél, T. 2004. “Turbulent drag reduction in dam-break flows.” Experiments in Fluids, 37(2), 219-229.
37. Kihara, N., Niida, Y., Takabatake, D., Kaida, H., Shibayama, A. and Miyagawa, Y. 2015. “Large-scale experiments on tsunami-induced pressure on a vertical tide wall.” Coastal Engineering, 99, 46-63.
38. Kihara, N. and Kaida, H. 2016. “On evaluation of tsunami bore pressure on a vertical wall Journal of Japan Society of Civil Engineering.”, B2. Coastal Engineering, 72(2) (in Japanese).
39. Kihara, N. and Kaida, H. 2019. “An application of semi-empirical physical model of tsunami-bore pressure on buildings.” Frontiers in Built Environment, 5, 3.
40. Kimmoun O, Ratouis A, Brosset L. 2010. “Sloshing and scaling: experimental study in a wave canal at two different scales.” Proc. Int. Offshore Polar Eng. Conf., 20th, 20–25th June, Beijing, China.
41. Kirkgöz S. 1982. “Shock pressure of breaking waves on vertical walls.” J. Waterways, Port Ocean Eng. Div. ASCE 108, 81-95.
42. Kirkgöz S. 1990. “An experimental investigation of a vertical wall response to breaking wave impact.” Ocean Eng. 17:379–391.
43. Kirkgoz, M.S. and Mamak, M. 2004. “Impulse modeling of wave impact pressures on vertical wall.” Ocean Eng., 31, pp.343-352.
44. Klammer, P., Kortenhaus, A. and Oumeraci, H. 1997. “Wave impact loading of vertical face structures for dynamic stability analysis-prediction formulae” In Coastal Engineering, 1996, (2534-2547).
45. Kondic, L. 2003. “Instabilities in gravity driven flow of thin fluid films.” SIAM Review, 45(1), 95-115.
46. Koshizuka, S. and Oka, Y. 1996. “Moving-particle semi-implicit method for fragmentation of incompressible fluid.” Nuclear Science and Engineering, 123(3), 421-434.
47. Lamb H. 1932. “Hydrodynamics.” 6th Edition. Cambridge University Press.

48. Lobovský, L., Botia-Vera, E., Castellana, F., Mas-Soler, J. and Souto-Iglesias, A. 2014. “Experimental investigation of dynamic pressure loads during dam break.” Journal of Fluids and Structures, 48, 407-434.
49. Loubere R, Braeunig JP, Ghidaglia JM. 2012. “A totally Eulerian finite volume solver for multi-material fluid flows: Enhanced Natural Interface Positioning (ENIP).” Eur. J. Mech. B 31:1–11.
50. Mampaey, F., Xu Z. 1995. “Simulation and Experimental Validation of Mould Filling.” Proc. Modeling of Casting, Welding and Advanced Solidification Processes VII, London, September 10-12th.
51. Mizutani, N., Umeda, J. and Ikemoto, M. 2017. “Characteristics of impact force on vertical wall caused by splashdown of run-up water column after tsunami collision Journal of Japan Society of Civil Engineering.”, B2. Coastal Engineering, 73(2) (in Japanese).
52. Nouri, Y., Nistor, I., Palermo, D. and Cornett, A. 2010. “Experimental investigation of tsunami impact on free standing structures.” Coastal Engineering Journal, 52(1), 43-70.
53. Oumeraci H, Klammer P, Partenscky HW. 1993. “Classification of breaking wave loads on vertical structures.” J. Waterw. Port Coast. Ocean Eng. 119:381–97
54. Peregrine, D. H. 2003. “Water-wave impact on walls.” Annual Review of Fluid Mechanics, 35(1), 23-43.
55. Ramsden, J. D. 1993. “Tsunamis: Forces on a Vertical Wall Caused by Long Waves, Bores, and Surges on a Dry Bed.” Ph.D Thesis California Institute of Technology.
56. Ramsden, J. D. 1996. “Forces on a vertical wall due to long waves, bores, and dry-bed surges.” Journal of Waterway, Port, Coastal, and Ocean Engineering, 122(3), 134-141.
57. Rankine WJM. 1870. “On the thermodynamics theory of waves of finite longitudinal disturbances.” Philos. Trans. R. Soc. Lond. 160:277–88.
58. Ritter, A. 1892. “Die Fortpflanzung de wasserwellen.”. (“The Propagation of Water Waves.”)” Z. Ver. Dtsch. Ing, 36(33), 947-954.

59. Robertson, I. N., Riggs, H. R. and Mohamed, A. 2008. “Experimental results of tsunami bore forces on structures” In the 27th International Conference on Offshore Mechanics and Arctic Engineering, 509-517.
60. Robertson, I. N., Paczkowski, K., Riggs, H. R. and Mohamed, A. 2013. “Experimental investigation of tsunami bore forces on vertical walls Journal of Offshore Mechanics and Arctic Engineering, 135(2).
61. Sarjamee S., Nistor I., Mohammadian A. 2017. “Numerical investigation of the influence of extreme hydrodynamic forces on the geometry of structures using OpenFOAM.” Nat Hazards 87:213–235.
62. Scolan YM, Korobkin AA. 2003. “Energy distribution from vertical impact of a three-dimensional solid body onto the flat free surface of an ideal fluid.” J. Fluids Struct. 17:275–86.
63. Semenov Y. A., Wu G. X. 2013. “Asymmetric impact between liquid and solid wedges.” Proc. R. Soc. A 469: 20120203.
64. Shen, J., Wei, L., Wu, D., Liu, H. and Huangfu, J. 2020. “Spatiotemporal characteristics of the dam-break induced surge pressure on a vertical wall.” Coastal Engineering Journal, 62(4), 566-581.
65. Shu, J. J. 2004. “Slamming of a breaking wave on a wall.” Physical Review. E, Statistical, Nonlinear, and Soft Matter Physics, 70(6 Pt 2), 066306.
66. Stoker, J. J. 1957. “Water waves, the Mathematical Theory with Applications.” Interscience Publishers, New York.
67. Takagi, H. and Furukawa, F. 2021. “Stochastic uncertainty in a dam-break experiment with varying gate speeds.” Journal of Marine Science and Engineering, 9(1), 67.
68. Tao M., Cen Y. 1988. “The Solution of an Accelerating Plate by Lagrangian Method.” Engineering Mechanics 7th Conf. ASCE, New York.
69. Thao N. D., Takagi H., Shibayama T. 2007. “Violent Wave Impact on Vertical Wall using Pressure-Impulse Theory.” Proceedings of Coastal Engineering, JSCE, 54: 811-815 (in Japanese).
70. The 2011 Tohoku Earthquake Tsunami Joint Survey (TTJS) Group, 2012.

71. Thoroddsen, S. T. and Sakakibara, J. 1998. “Evolution of the fingering pattern of an impacting drop.” Physics of Fluids, 10(6), 1359-1374.
72. Vischer, D. L. and Hager, W. H. 1998. “Dam Hydraulics” Wiley, 287-288.
73. Von Kάrmán T. 1929. “The impact of seaplane floats during landing.” NACA Tech. Note 321, Natl. Advis. Comm. Aeronaut., Washington, DC.
74. Wagner H. 1932. “Uber Stoß- und Gleitvorgange an der Oberflache von Flussigkeiten. Z. Angew.” Math. Mech. 12:193–215.
75. Wei Y, Abadie T, Henry A, Dias F. 2016. “Wave interaction with an Oscillating Wave Surge Converter, part II: slamming.” Ocean Eng. 113: 319–334.
76. Wemmenhove, R., Gladsø, R., Iwanowski, B. and Lefranc, M. 2010 International Offshore and Polar Engineering Conference Beijing. “Comparison of CFD calculations and experiment for the Dambreak experiment with one flexible wall.” Proceedings of the Twentieth China, June 20-25, 2010, 200-205.
77. Wood, D. J., Peregrine, H. 1998. “Two and three-dimensional pressure-impulse models of wave impact on structures.” Coast. Eng. 1–3: 1502–1515.
78. Wu G. X. 2007. “Two dimensional liquid column and liquid droplet impact on a solid wedge.” Q. J. Mech. Appl. Math. 60: 497-511.
79. Wüthrich, D., Pfister, M., Nistor, I. and Schleiss, A. J. 2018. “Experimental study on the hydrodynamic impact of tsunami-like waves against impervious free-standing buildings.” Coastal Engineering Journal, 60(2), 180-199.
80. Xie W., Shimozono T. 2022. “Water surge impingement onto a vertical wall: Laboratory experiments and stochastic analysis on impact pressure.” Ocean Eng. (in press).
81. Xu, Z., Melville, B., Whittaker, C., Nandasena, N. A. K. and Shamseldin, A. 2021. “Mitigation of tsunami bore impact on a vertical wall behind a barrier.” Coastal Engineering, 164.
82. Yeh, H., Barbosa, A. R., Ko, H. and Cawley, J. G. 2014. “Tsunami loadings on structures: Review and analysis.” Coastal Engineering Proceedings, 1(34): currents, 4.

Acknowledgements

I wish to express my sincere gratitude to my supervisor, Prof. Takenori Shimozono. I am by no means an intelligent student among his former students, nor a diligent one. I also confess that I actually failed many times during the analytical derivations and laboratory works. However, he instructed me with a great amount of patience. He always encourages me to do my research rigorously. He frequently uses the Japanese word “Kichinto” to emphasize his standard of the rigor in scientific research. I learned a lot from him; not only the academic knowledge, but also a portrait of researcher. Without his supervision, I would still be a naïve college boy.

I appreciate Prof. Yoshimitsu Tajima and Prof. Yusuke Yamanaka for their helpful advises through these three years. In lab seminars, they have pointed out many shortcomings of my progresses and guided me to improve them. Appreciation is also extended to Prof. Takeshi Ishihara, Prof. Jun Sasaki and Prof. Fuminori Kato. They helped me to improve my thesis and gave many accurate comments from various angles during the pre-defense, individual defense and final defense.

I am also thankful to Prof. Tomoya Shibayama, Prof. Takahito Mikami, Prof. Miguel Esteban, Prof. Mark Bowen, Prof. Masato Sekine and Prof. Takeshi Miyazaki. Their instructions during my bachelor and master degree studies provided me with a solid foundation of coastal engineering, fluid mechanics, hydraulics and applied mathematics. I actually frequently revisited the class notes during the research.

I also wish to express my gratitude to Dr. Masayuki Urabe, Prof. Yasuyuki Seto, Dr. Koichi Yagi, Dr. Yasuhiro Okumura, Dr. Motonari Li and many doctors and nurses from the University of Tokyo Hospital. They saved my life from cancer. Without their surgery and nursing, I would stand no chance to finish my doctoral research and this thesis. They are the true heroes.

Appreciation is extended to Dr. Fangqiu Lu, Dr. Hainan Yue, Dr. Yi Ji, Mr. Tianrun Liu, Mr. Xi Sun, Mr. Yan Wu, Ms. Kexuan Guo, Mr. Hongchen Wang, Dr. Shengwei Zhu and many of my friends. They have warmly supported me during the darkest days of my life. Truly, truly, I enjoyed the time chatting, laughing and hunting with them.

I wish to dedicate this thesis to my parents and family members. From my high school ages, they have been encouraging me to keep on the journey towards natural science, by which I was fascinated. Even I never was a clever student in the class, they always told me that it is not who you are, but what you persist on, truly makes the difference. Following that, now I have become the first doctor candidate in science and engineering in my entire family tree.

I wish to dedicate this work to my dear fiancée. You are my guardian angel and the evening star, keeping watching and shining down upon me through these years. May it be when darkness falls, I will not walk a lonely road.

May your swords stay sharp!

Wenang XIE, Tokyo
2022/02

乱石穿空、驚濤拍岸、巻起千堆雪。